UNIVERSIDADE DE SÃO PAULO
INSTITUTO DE FÍSICA DE SÃO CARLOS

and

TECHNISCHEN UNIVERSITÄT DARMSTADT
INSTITUTE OF ELECTRONIC MATERIALS

GREGÓRIO COUTO FARIA

Structure and dynamics of poly(9,9-dioctylfluoren-2,7-diyl-*co*-benzothiadiazole) (F8BT) and correlations with its electrical properties

São Carlos/Darmstadt
2011

TECHNISCHEN UNIVERSITÄT DARMSTADT
INSTITUTE OF ELECTRONIC MATERIALS

und

UNIVERSIDADE DE SÃO PAULO
INSTITUTO DE FÍSICA DE SÃO CARLOS

Vom Fachbereich Material- und Geowissenschaften zur Erlangung des
akademischen Grades Doktor rerum naturalis (Dr. rer. nat.) genehmigte
Dissertation von M. Sc. GREGÓRIO COUTO FARIA, geboren am 05.01.1984 in
São Carlos, Brasilien

Structure and dynamics of poly(9,9-dioctylfluoren-2,7-diyl-*co*-benzothiadiazole) (F8BT) and correlations with its electrical properties

Datum der Prüfung: 16.09.2011

São Carlos/Darmstadt
D 17
2011

GREGÓRIO COUTO FARIA

STRUCTURE AND DYNAMICS OF POLY(9,9-DIOCTYLFLUOREN-2,7-DIYL-*CO*-BENZOTHIADIAZOLE) (F8BT) AND CORRELATIONS WITH ITS ELECTRICAL PROPERTIES

Tese apresentada ao Programa de Pós-Graduação do Instituto de Física de São Carlos da Universidade de São Paulo – Brasil e Technischen Universität Darmstadt - Alemanha para obtenção da Dupla Titulação de Doutor em Ciência

Área de concentração: Física Aplicada

Orientadores/Advisors:
Prof. Dr. Eduardo Ribeiro de Azevêdo
Prof. Dr. Heinz von Seggern

Versão Corrigida/Final Version

São Carlos/Darmstadt
2011

GREGÓRIO COUTO FARIA

STRUCTURE AND DYNAMICS OF POLY(9,9-DIOCTYLFLUOREN-2,7-DIYL-*CO*-BENZOTHIADIAZOLE) (F8BT) AND CORRELATIONS WITH ITS ELECTRICAL PROPERTIES

Thesis submitted to the Graduate Program of the Instituto de Física de São Carlos/Universidade de São Paulo – Brazil and to Fachbereich Material- und Geowissenschaften/Technischen Universität Darmstadt - Germany in order to obtain the Double Degree of Doctor in Science.

Advisors/Orientadores:
Prof. Dr. Heinz von Seggern
Prof. Dr. Eduardo Ribeiro de Azevêdo

Final Version/Versão Corrigida

Darmstadt/São Carlos
2011

AUTORIZO A REPRODUÇÃO E A DIVULGAÇÃO TOTAL OU PARCIAL DESTE TRABALHO, POR QUALQUER MEIO CONVENCIONAL OU ELETRÔNICO, PARA FINS DE ESTUDO E PESQUISA, DESDE QUE CITADA A FONTE.

REPRODUCTION IS AUTHORIZED WITH APPROPRIATE CITATION

Ficha catalográfica elaborada pelo Serviço de Biblioteca e Informação - IFSC/USP

Faria, Gregório Couto.
Structure and dynamics of poly(9,9-dioctylfluoren-2,7-diyl-*co*-benzothiadiazole) (F8BT) and correlations with its electrical properties. orientadores/advisors Eduardo Ribeiro de Azevêdo; Heinz von Seggern. Versão Corrigida. São Carlos/Darmstadt 2011.
184 p.

Tese (Doutorado com Dupla Titulacao em Ciencias) – Instituto de Física de São Carlos/Universidade de São Paulo - Brasil e Fachbereich Material- und Geowissenschaften/Technischen Universität Darmstadt – Germany, 2011.

1. Conjugated polymers. 2. Molecular relaxation. 3. Molecular dynamics. 4. Electrical properties. 5. Charge-carrier mobility. I. Título.

ACKNOWLEDGEMENTS

After three years and four months of Ph.D. into two Universities, leading with several different techniques, living in two different countries, I have learned one thing: I could never have done **any** of these, particularly the research and writing that went into this thesis, without the help, support and encouragement of a lot of people. Therefore, I would like to thank all who directly or indirectly helped me during this period.

First of all, I deeply thank my Brazilian advisor, Prof. Eduardo Ribeiro de Azevêdo, whose friendship, help, advice and supervision was invaluable. I really appreciate his vast knowledge and skill in many areas (e.g., basics physics, fundaments of NMR, quantum mechanics, polymers science and electrical properties). Without his help, this work would not be possible.

A very special thanks goes out to Prof. Heinz von Seggern, my Germany advisor, to be so kind with me during my times in Darmstadt. You have given so much of yourself to help and to teach me a lot of new things. You also have given me the courage to succeed in most of my electrical properties. Many thanks.

I am indebt with Mrs. Bruna Medeiro Hamabata for her patience and dedication helping me revises the English grammar of my text. Thanks for your enthusiasm, even at 10:00 o'clock at night!

I would also like to thank all of my friends from Instituto de Física de São Carlos: Giovani Gozzi, Rafael Henriques Longaresi, Alexandre Maciel, Washington Souza, Marcos Felipe Sampaio, Márcio Cobo, Oigres Bernardinelli, Wesley Bezerra. Not only are you the people I can discuss my research with and goof off with, but also you are confidants who I can discuss my troubles with and who stand by me through thick and thin

I am also grateful to my colleagues from TU Darmstadt: Andrea Gassman, Cristian Melzer, Dan Walker, Eva Feldmeier, Gabriele Kühnermundt, Graham

Appleby, Helga Janning, Jörg Schütrumpf, Katja Stegmaier, Lorenz Kehrer, Martin Schidleja, Oliver Ottinger and Tobias Koenyves. A special thanks goes to Bernd Stoll to be so kind and helpful during the implementation of the Photo-CELIV technique. I want let them know that my times in Darmstadt were one of the best of my life.

Finally, I would like to dedicate this work to my family: my grandfather Francisco Couto, my parents Roberto and Marta Faria, to my syster Julia Faria, and specially, to my grandmother, Ceníria Flávio Simões Couto. Without your unending support and love from childhood to now, I never would have made it through this process or any of the tough times in my life. Thank you. This thesis is also dedicated to my parents in law Gerson Edson and Sônia Toledo Piza for being always in my side. I also must acknowledge my fiancé, partner and best friend, Maria Elisa Toledo Piza, without whose love, encouragement and moral support I would not have finished this thesis.

I also recognize that this research would not have been possible without the financial assistance of Fundação de Amparo à Pesquisa do Estado de São Paulo (FAPESP) - (Proc-number 2008/01935-5) and by the Deutscher Akademischer Austausch Dienst (DAAD) - (Proc-number A/09/72945; ref. 415). I would like thank and express my gratitude to those agencies.

to Maria Elisa

— whose love gave me strength

RESUMO

FARIA, G.F. Estrutura e Dinâmica do poly(9,9-dioctylfluoren-2,7-diyl-*co*-benzothiadiazole) (F8BT) e correlações com suas propriedades elétricas. 2011. 184p. Tese (Doutorado em Ciências) – Instituto de Física de São Carlos, Universidade de São Paulo, São Carlos e Technischen Universität Darmstadt – Alemanha, 2011.

O projeto de doutorado entitulado "Correlação das Propriedades Óticas e Elétricas com a Estrutura Física e Dinâmica Molecular de Filmes e Dispositivos de Polifluorenos e Derivados". O primeiro é especificamente ligado a investigação da dinâmica molecular, conformação estrutural e empacotamento de polímeros derivados do polifluoreno. Para isso, Difração de Raio-X de Alto Ângulo (WAXD)[1], Ressonânica Magnética no Estado Sólido (RMN) e Análise Térmica Dinâmico Mecânica (DMTA) serão utilizadas como técnicas principais. O segundo objetivo é o de correlacionar, os fenômenos observados na primeira parte do projeto, com as propriedades opto-eletrônicas dos filmes poliméricos sendo utilizados como camada ativa em dispositivos eletrônicos do tipo Diodo Polimérico Emissor de Luz (PLED). Na segunda parte, a fabricação dos dispositivos e sua caracterização como função da temperatura serão os principais objetivos. Espectroscopia de Impedância, Corrente-Voltagem, Tempo de Vôo (TOF) e Photo-CELIV serão as principais técnicas de caracterização utilizadas. Dessa forma, o projeto combina estudos fundamentais de aspectos moleculares com o desempenho tecnológico de dispositivos optoeletrônicos.

Palavras chave: Polímeros conjugados. Relaxação molecular. Dinâmica molecular . Propriedades elétricas. Mobilidade de portadores de carga.

ABSTRAKT

FARIA, G.F. **Korrelation zwischen der molekularen Dynamik und physikalischen Struktur eines Polyfluorenderivats mit den optoelektronischen Eigenschaften von daraus hergestellten Bauteilen.** 2011. 180p. Doktorarbeit (Doktor der Naturwissenschaften) - Technischen Universität Darmstadt, Fachbereich Material- und Geowissenschaften, Darmstadt, Germany and Instituto de Física de São Carlos, Universidade de São Paulo, São Carlos, Brazil, 2011.

Der erste Teil der Arbeit befasst sich mit der Untersuchung der molekularen Dynamik und Konformation sowie der molekularen Packung von Polyfluoren-basierten Polymerschichten. Die hauptsächlich verwendeten Analysemethoden waren die Röntgenweitwinkelbeugung (WAXD), die Festkörper-NMR und die dynamisch-mechanische Analyse (DMTA). In dem zweiten Teil der Arbeit wurden polymere Leuchtdioden (PLEDs) mit dem Polyfluorenderivat als Funktionsschicht hergestellt und deren optoelektronische Eigenschaften charakterisiert. Dazu wurden temperaturabhängige Strom-Spannungs-Kennlinien, Impedanzmessungen und Beweglichkeitsmessungen durchgeführt. Das Hauptziel der vorliegenden Arbeit war es, Korrelationen zwischen den molekularen Phänomenen, die im ersten Teil der Arbeit identifiziert wurden, und den Eigenschaften der PLEDs, die im zweiten Teil ermittelt wurden, zu finden.

Keywords: konjugierte Polymere. molekulare Relaxation. molekulare Dynamik. elektrische Eigenschaften. Ladungsträgerbeweglichkeit.

ABSTRACT

FARIA, G.F. **Structure and dynamics of poly(9,9-dioctylfluoren-2,7-diyl-*co*-benzothiadiazole) (F8BT) and correlations with its electrical properties.** 2011. 180p. Thesis (Ph.D in Science) – Instituto de Física de São Carlos, Universidade de São Paulo, São Carlos and Technischen Universität Darmstadt – Germany, 2011.

The PHD project has two main goals. The first one is specifically related to investigations on molecular dynamics, structural conformations and packing of polyfluorene-based polymers. For this purpose, Wide Angle X-Ray Diffraction (WAXD), Solid-State Nuclear Magnetic Resonance (NMR) and Dynamical-Mechanical Thermal Analysis (DMTA) are being used as the main techniques. The second goal is to correlate molecular phenomena, as characterized in the first part, with opto-electronic properties of polyfluorene when used as active layer in an electronic device, such as a Polymer Light-Emitting Diode (PLED). In the second part, fabrication of devices and their electrical characterization as a function of temperature are the main objectives. Impedance Spectroscopy, Current-Voltage characterization of the devices and Time-Of-Flight (TOF) techniques are among the main techniques to be used in the second part of the project. Therefore, the project combines fundamental studies on molecular dynamics with technological performance of organic electronic

Keywords: Conjugated polymers. Molecular relaxation. Molecular dynamics. Electrical properties. Charge-carrier mobility.

LIST OF FIGURES

Figure 1 – Illustration of the use of polymers as insulating material: high-voltage wires and houseware objects............................ 37

Figure 2 – The projected global organic electronic market from 2008 until 2017: It is expected to reach the total of 19 billion dollars of business on 2017[26].. 39

Figure 3 - Images from the first full Sony OLED television to go on sale. Inset: OLED television resolution versus conventional LED television.. 40

Figure 4 - a) Illustration of the main-chain dimerization due to the Peierls Instability: The band gap in polymeric systems appears since the length of single and double bound are different; therefore, the repeat unit has two atoms and the π orbital is divided in two; b) Illustration of the sp^2 hybridization: π orbital of two consecutives carbons overlaps, giving rise to a delocalized orbital, providing a "highway" for charge mobility along the polymer chain.. 42

Figure 5 – Electromagnetic Spectrum: The energy between 1 and 4 eV covers all the visible range. Most of the conjugated polymer emits light in this range of frequency, being then applied with success in optoelectronics devices..................................43

Figure 6 – Molecular structure of different polyacetylene isomers: a) the cis-polyacetylene and b) the trans-polyacetylene...44

Figure 7 - Model for transport in low and high-MW films. a) Charge carriers are trapped on nanorods (highlighted in grey) in the low MW case. b) Long chains in high-MW films bridge the ordered regions and soften the boundaries. Figure adapted from reference 20. 46

Figure 8 – X-ray analysis of a) out of plane and b) in plane diffraction of P3HT samples with different molecular weight. Note that low molecular weight films seem to produce high ordered structure. Figure adapted from reference 20.......................... 48

Figure 9 - Molecular structure of Polyparaphenylene vinylene (PPV) (top) and its derivatives: poly(2-methoxy-5-(n-hexadecyloxy)-p-phenylene vinylene) (MH-PPV) and poly[2-methoxy-5-(2 -ethyl-hexyloxy)-1,4-phenylene vinylene] (MEH-PPV) (botton).. 52

Figure 10 - Examples of several Polyfluorene chemical structure: a) Poly(9,9-dialkyl-fluorene), b) Poly[(9,9-dioctilfluorenil-2,7-

diil)-co-{1,4 vinilenofenileno)], c) Poly(9,9-di-n-octylfluorene-alt-benzothiadiazole) and d) Poly[9,9-di-(2-etil-hexil)-fluorenil-2,7-diil-2,5-diphenil-1,2,4-oxadiazole]............ 53

Figure 11 – Example of Differential Scanning Calorimetry (DSC) experimental results on Polyethylene polymer film: Glass Transition (T_g) in red, crystallization in blue and the melting of the ordered structure in green............................. 56

Figure 12 - Temperature dependent of the loss tangent measured by Dynamical-Mechanics Thermal Analysis (DMTA) on Polyethylene polymer film: γ, β and α are the relaxation of different segments on the molecule. Figure adapted from reference 62... 58

Figure 13 – ^{1}H Nuclear Magnetic Resonance (NMR) signal of Ethanol. The chemical-shifts differentiate the distinct hydrogen in the molecule: The two protons of the CH_2 group neighboring the oxygen are further to the left in the spectrum, whilst the hydrogens of the CH_3 group that is most remote from the oxygen produce a signal towards the right of the spectrum. The hydrogene attached to oxygen is 'deshielded' due to the electronegative nature of oxygen and this shifts its signal towards the left in the spectrum........... 62

Figure 14 - Series of powder line shapes simulated for different cases: left) rigid regime, centre) intermediated regime and right) fast regime: isotropic movement. It is possible to observe that the natural motion of the molecule average the ^{1}H-^{1}H coupling, producing a narrowing of the line shape.............. 69

Figure 15 – Schematic illustration of the Magic Angle Spinning (MAS). When no spinning is applied, the NMR signal is broad, since it is not possible to align all the internuclear vector in the magic angle direction (left); however, as shown at the right side of the figure, when a rotation of ω_r is applied, the alignment of the spin around the magic angle is achieved and a narrowing of the spectra is observed.......................... 73

Figure 16 – Laboratory, temporary and rotor coordinate systems.......... 74

Figure 17 – a) Sample rotation with the internuclear vector aligned along a direction different from the rotation axis, b) schematic representation of magnetization dephasing due to MAS and rotational echo... 77

Figure 18 – Illustration of the MAS method (left) and Cross Polarization Magic Angle Spinning pulse sequence (right)... 82

Figure 19 – a) Dipolar Chemical Shift Correlation (DIPSHIFT) pulse sequence and b) typical dependence of the DIPSHIFT curves with the dipolar coupling intensity............................ 84

Figure 20 – Comparison between the spin dynamics simulation (points) and equation 43 (lines): Anderson and Weiss approximation fits fairly good until $t_1/t_r = 0.5$... 86

Figure 21 – Top: Exchange NMR sequence and; Botton: examples of the 2D-signal for several reorientation angles.........................88

Figure 22 - Pulse sequences of the CODEX experiment. Pulse-moving scheme of the CSA recoupling periods t_{evol} and t_{reconv} for (b) CONTRA scheme. The length of the mixing period tm must be actively synchronized with the MAS rotation. Adapted from reference 80...89

Figure 23 – Left) Experimental (full symbols) and calculated data (open symbols, full line) for the PMMA COO group and Right) Experimental (full symbols) and calculated data (open symbols, full lines) for the OCH3 (top) and CH3 (bottom) groups in methyl rhamnose glass. Adapted from reference 80... 90

Figure 24 – Example of 2D X-Ray Diffractograms of a) Semi-crystalline with spots and sharp rings and b) amorphous polymer characterized by broad and diffusive rings............... 93

Figure 25 - Idealization (left) and real (right) Current-Voltage (IxV) characteristics for organic crystals, such as Pentacene. Observe that, four regions can be found in a regular IxV: an Ohmic regime, in which the current is proportional to the electric field; the trap-limited SCLC regime, already discussed; the Trap-Filled regime, where all traps in the sample are filled, and finally, the trap-free SCLC.................. 99

Figure 26 – Dielectric loss example for the Poly(aryletherketone). Observe the appearance of the two main relaxation processes. Inset: Arrhenius plot for both relaxations. Adapted from reference 62.. 104

Figure 27 – Illustration of TOF transient: The intersection between the plateau and the extension of the tail is given by the transit time.. 106

Figure 28 - Schematic illustration of the Photo-CELIV method. V_{max} is the top voltage applied; λ is the nanosecond laser pulse; Δj is the extracted transiente current; j(0) is the displacement current; τ_{pulse} is the length of the voltage pulse; τ_{delay} is the delay between the laser pulse and the voltage pulse and τ_{max} is the time at the highest current of Δj. On the right: Schematic illustration of the used device and the molecular structure of F8BT...110

Figure 29 – Molecule Structure of the F8BT polymer material..............112

Figure 30 – Illustration of the sandwich-like devices built for the electrical measurements: The polymer films were grown on cleaned ITO substrates and the aluminum cathode were thermally evaporated... 113

Figure 31 – Differential Scanning Calorimetry (DSC) data for F8BT polymer film; (Top) the heating and (Bottom) the cooling stage... 116

Figure 32 – WAXD measurement setup: Left) Sample holder and detector and Right) Sample holder for each of the experimental geometries (normal and parallel incidences)..... 118

Figure 33 – Wide Angle X-Ray Diffraction (WAXD) results of F8BT films at 298 K for incidences, normal and parallel. Top: 2D images and, Botton: 1D pattern. The inset in the middle represents the lamellar β-phase...120

Figure 34 - WAXD measurements as a function of temperature and for both incidences normal (left) and parallel (right)................. 121

Figure 35 – DMTA results: (Left) tanδ versus temperature for several excitation frequencies and, (Right) the Arrhenius plot for the low-temperature β-relaxation... 123

Figure 36 – ^{1}H NMR results: (Left) spectra for several temperatures. As the temperature increase the signals get narrower: and (Right) the line width versus temperature. Two transition regions is observed, which were attributed to the transition already measured by DSC and DMTA...................................125

Figure 37 – CPMAS results for two temperatures (193 and 373 Kelvins) and the correspondent assignment of carbons and lines.. 127

Figure 38 - DIPSHIFT curves obtained at several temperatures and from different carbons on the polymer chain: side chain (a and b) and main chain (c). The Arrhenius plot of the side chain carbons are presented at d... 129

Figure 39 - CONTRA results of: a) carbons 3 and 5; b) carbon 7. It is possible to observe that the reorientation angle of the main chain increase with temperature... 131

Figure 40 - IxV characteristics for selected temperatures for F8BT thick devices. Observe the presence of the trap-filled limit.... 135

Figure 41 - Total density of traps calculated from the $VTFL$ point of experimental IxV curves of thick films devices......................136

Figure 42 – Top: Absorption Spectrum for F8BT: The laser incidence wavelength was choose at the maximum of absorption (470 nm). Botton: Comparison between electrons and holes TOF transient: Observe that electron transient is stronge than that of holes.. 139

Figure 43 – Top: Typical current mode TOF transient for electrons at T = 340 K; the inset we have the same curve in a log-log representation. Bottom: the calculated mobility for each measured temperature.. 140

Figure 44 – Top: Cole-Cole diagram for selected temperature are presented and Botton: The Real Impedance versus temperature for selected frequencies are illustrated.............. 144

Figure 45 – Arrhenius Plot for the two high-temperature peaks observed in the real impedance versus temperature curves, as signed by the inset... 145

Figure 46 – Top) Real Impedance versus temperature for the frequencies range of 0.1 to 3.16 Hz and; botton) Arrhenius plot for the β-relaxation process.. 148

Figure 47 - Arrhenius Plot for the two high-temperature peaks observed in the real impedance versus temperature curves, as signed by the inset.. 149

Figure 48 - Experimental Current-Voltage characteristics for F8BT thin-film device for several temperatures.............................. 151

Figure 49 – Current-Voltage fitting using the model described at chapter 2. The fitting were made on the SCLC regime for different temperatures... 153

Figure 50 - Calculated mobility at zero-field for each measured temperature in a $\ln\mu \; vs \; T-2$ graph, studied by the GDM model. 155

Figure 51 – Absorption spectrum of F8BT: CELIV laser excitation wavelength was choose to be at 335 nm.............................. 156

Figure 52 – a) Photo-CELIV current extraction obtained for the Al/F8BT/ITO device at 350 K. b) Photo-CELIV current profile for the Al/F8BT/ITO device at several temperatures. As an inset are the $\Delta J / J(0)$ values plotted as a function of temperature.. 158

Figure 53 – a) Mobility calculated from Photo-CELIV transients as a function of temperature together with the dielectric relaxation - tanδ - in order to correlate changes in the mobility with molecular relaxations. b) Plot of $t_{1/2}$, t_{max} and $t_{1/2}/t_{max}$ obtained from the CELIV measurements as a function of $1000/T^2$ and T.. 161

Figure 54 – Comparison between mobility measured by CELIV and modeled by Current-Voltage characteristics of thin-film devices. The blue circle is the dielectric loss in order to illustrate the correlation between the changes observed on the mobility curves and the molecular dynamics measured and discussed in chapter 2..165

Figure 55 - A naive picture of the structural detrapping mechanism in F8BT samples (τ is the hopping time) for several temperatures... 167

LIST OF ABBREVIATIONS

AC	Alternated Current
CELIV	Current-Extraction by Linear Increasing Voltage
CODEX	Centerband-Only Detection of Exchange
CONTRA	Constant Time Recoupling of Anisotropy
CP	Cross Polarization
DD	Dipolar Decoupling
DIPSHIFT	Dipolar Chemical Shift Correlation
DMTA	Dinamical-Mechanics Thermal Analysis
DSC	Differential Scanning Calorimetry
F8BT	Poly(9,9-dioctylfluorene-co-benzothiadiazole)
GPC	Gel Permeation Chromatography
HOMO	Highest Occupied Molecular Orbital
IS	Impedance Spectroscopy
IV	Current-Voltage
LC	Liquid Crystal
LCD	Liquid Crystal Display
LG	Lee-Goldburg
LNLS	Brazilian Synchrotron Laboratories
LUMO	Lowest Unoccupied Molecular Orbital

LVR	Linear Voltage Ramp
MAS	Magic Angle Spinning
M_n	Number Average Molecular Weight
M_w	Average Molecular Weight
PAS	Principal Axes System
PF	Polyfluorene
PL	Photoluminescence
PLED	Polymer Light-Emitting Diodes
PMLG	Phase-Modulated Lee-Goldburg
PPV	Poly(phenylenevinylene)
rf	Radio Frequency
NMR	Nuclear Magnetic Resonance
T_g	Glass Transition
TOF	Time of Flight
TPPM	Two Pulse Phase Modulation
WAXD	Wide Angle X-Ray Diffraction

SUMMARY

1 **Introduction** 35

1.1 Historical Perspective 35
1.2 Polymer Materials: Toward Conjugated Systems 39
1.3 Importance of Charge Transport and Its Correlation with Structure and Dynamics 43
1.4 Outline of the Thesis 47

2 **Materials and Techniques** 51

2.1 Material: Poly(9,9-di-n-octylfluorene-alt-benzothiadiazole) (F8BT) 51
2.2 Thermal Methods 53
2.3 Nuclear Magnetic Resonance Technique (NMR) 56
  2.3.1 Chemical Shift 61
  2.3.2 Dipolar Interaction 62
  2.3.3 Static Hydrogen Spectra (^{1}H) 66
  2.3.4 Excitation and Detection of Organic Compounds 70
  2.3.5 ^{1}H Dipolar Decoupling 71
  2.3.6 Magic Angle Spinning (MAS) 70
  2.3.7 Cross Polarization (CP) 80
  2.3.8 Cross Polarization Magic Angle Spinning Experiment (CPMAS) 81
  2.3.9 Dipolar Chemical Shift Correlation (DIPSHIFT) 81
  2.3.10 Centerband-Only Detection of Exchange (CODEX) 85
2.4 X-Ray Measurements 90

2.5 Electric Measurements 93
  2.5.1 Current versus Voltage Measurements (IxV) 94
  2.5.2 Impedance Spectroscopy (AC) 100
  2.5.3 Time of Flight Technique (TOF) 104
  2.5.4 Current Extraction by Linear Increasing Voltage 108
2.6 Fim and Device Preparation 111

3 **Molecular Relaxation, Dynamics and X-Ray Results** **113**

3.1 Structural Results: Differential Scanning Calorimetry and Wide Angle X-Ray Diffraction 115
3.2. Molecular Dynamic Results: Dinamical Mechanical Thermal Analysis and Nuclear Magnetic Resonance 120

4 **Electrical Results** **133**

4.1 Thick Films Devices 133
  4.1.1 Current versus Voltage (IxV) 134
  4.1.2 Time of Flight Technique (TOF) 138
  4.1.3 Impedance Spectroscopy (AC) 143
4.2 Thin Films Devices 146
  4.2.1 Impedance Spectroscopy 150
  4.2.2 Current versus Voltage (IxV) 156
  4.2.3 Current Extraction by Linear Increasing Voltage 146

5. **Summary: Correlation between Molecular Dynamics and Structure with Electronic Properties** 163

6. **Conclusion and Perspectives** 169

References 171

1 Introduction

In the introduction, it will be presented a brief historic perspective on the polymer science as a field of research. The conjugated polymer material shall be introduced and the importance of understanding charge transport features in this material is addressed. Finally, the first chapter ends by outlining the scope of this thesis.

1.1 Historical Perspective

Organic materials, such as polymers, have been mainly used as insulator materials due to its low conductivity properties. Also, because of its mechanical properties, such as malleability and low cost processing, polymers have stimulated many applications in a day-to-day life of our society. For instance, protection of high voltage wires and houseware objects, as illustrated in figure 1.

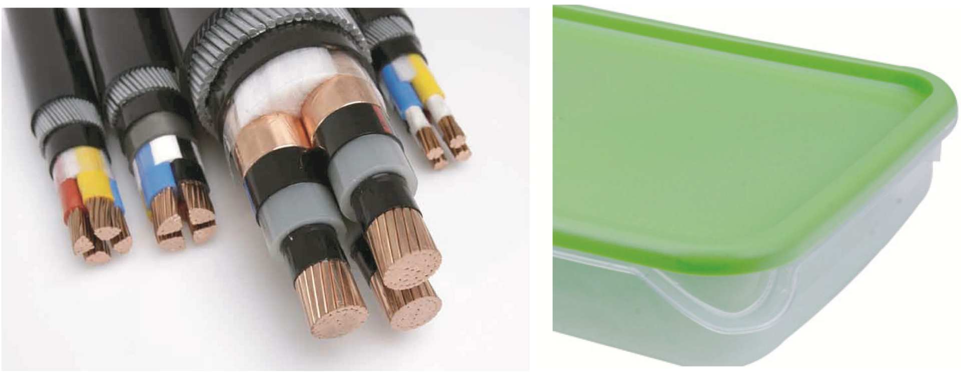

Figure 1 – Illustration of the use of polymers as insulating material: high-voltage wires and houseware objects.

However, this scenario started to broaden in the early 1960s, when organic crystals, such as anthracene, were exploited because of their semiconducting properties[1]. This period contributed heavily for the theoretical understanding of electronic properties of such organic molecules. Nevertheless, no significant breakthroughs concerning advances for industrial application have been reached[2].

The interest of xerography companies in organic semiconductors, started in the 1980s, gave prominence to this field, and most photocopiers and laser printing machines still exploit their photoconductivity properties. Nonetheless, it was just in the very beginning of the 1990s that the polymer has appeared as a protagonist of organic electronics. Jeremy Burroughes and co-workers published the discovery of Polymer Light-Emitting Diodes (PLED) using conjugated polymers as activity layer[3]. This impressive contribution has opened a great perspective both for industrial application, such as optoelectronic devices, and for academic purposes[3-11].

Many spin-off companies have come to the market and some prototypes of monochromatic signs displays, and similar prototype devices made by conjugated polymers technology were promptly launched on the market. Subsequently, both Organic Photovoltaic Cells (OPV) and Organic Field-Effect Transistors (OFET) joined the range of polymer electronics, giving the field extra possibilities of studies and applications[11-13]. However, problems related to the instability and low efficiency of such class of material, compared to inorganic ones, have partially delayed the large-scale industrial production[14-19]. Some of these problems are related to molecular structure, dynamics and morphology[20-25], which make such properties worth investigating. Indeed, today's electronic researches also focus on miniaturizing the size of devices, toward single-molecules devices.

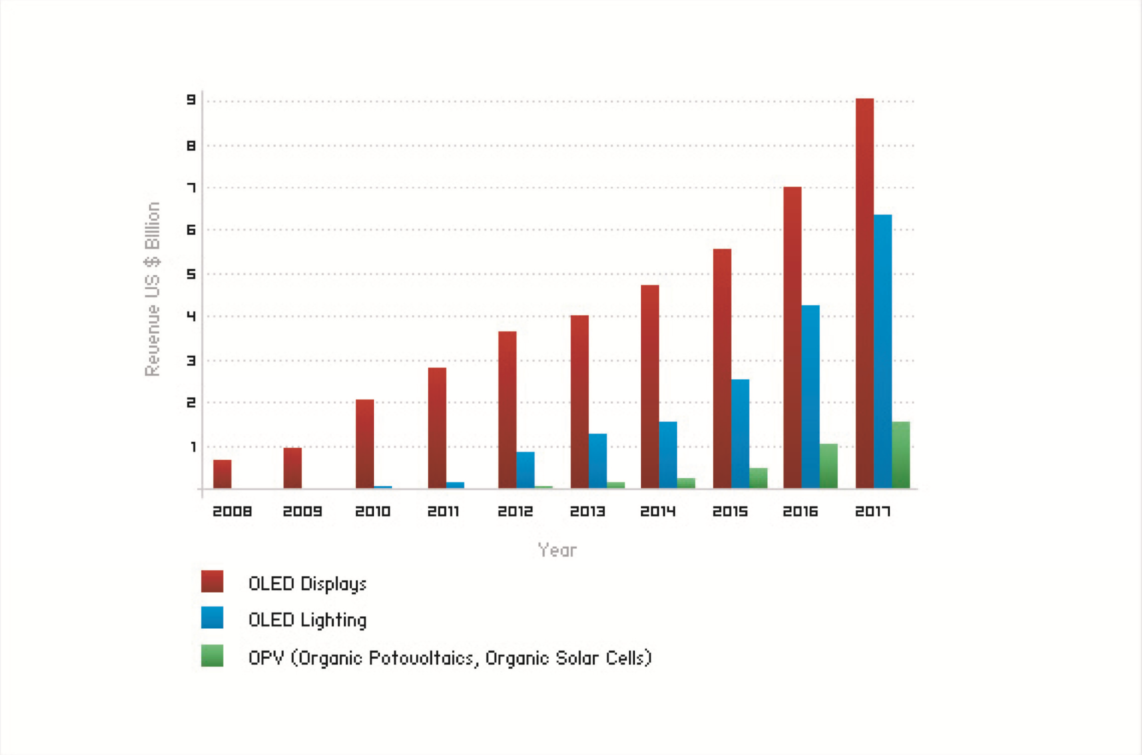

Figure 2 – The projected global organic electronic market from 2008 until 2017: It is expected to reach the total of 19 billion dollars of business on 2017[26].

Despite the problems with instability and efficiency, the current global organic electronic market is increasing significantly, and it is expected to reach approximately 19 billion Dollars in 2017[26] (see figure 2). In late 2007, Sony presented its first prototype of an 11-inch all organic active display[27]. The flexible version was also presented as a prototype in 2010[28]. Last february (2011), the same company introduced two model of professional OLED television at the market, the very first all-organic television to go on sale[29] (see figure 3). These models, with 17 and 25 – inch screens are expected to be on market between October and November 2011. It is worth mentioning that smaller screens (around 3-inch) have been successfully launched at the market, mainly embedded in cell phones and other gadgets devices.

OLED
LCD
SONY
SONY
rototyp
GIZMODO
CES

Figure 3 - Images from the first full Sony OLED television to go on sale. Inset: OLED television resolution versus conventional LED television.

The OLED technology is, then, a reality; however, much needs to be done, especially for better understanding the properties of such class of materials. Therefore, it is important to elucidate molecular features of conjugated polymer materials and correlate them with optoelectronic properties. It is well established that, differently from most inorganic semiconductors and metals, polymer films normally have a random or partially oriented structures, being characterized by loops, coils and kinks leading to entanglement of the polymer chain and the formation of ordered regions[30]. Their highly disordered morphology is the bottleneck for transport properties, since charge carrier conduction in this type of system requires an adequate overlap of the π orbital between adjacent molecules: thus, it is expected that, the more planar the structure, the better the conduction[20,30]. At this point, one might be able to evaluate the importance of studying and understanding correlations between molecular structure, morphology and dynamics with optoelectronic properties of polymeric materials.

In this sense, this thesis intends to contribute to the development of this technology, even a little. For the better understanding of the concepts used throughout this thesis, a brief overview of polymer material will be presented in the following sub-chapter.

1.2 Polymer Materials: Toward Conjugated Systems

As mentioned before, polymer materials have been mainly used for insulating applications. The insulate properties arise from the fact that each carbon in the backbone is generally bonded with other four distinct atoms[31]. Therefore, the polymer's main-chain is composed by σ-bond[31]. A classical example is the polyethylene (- CH_2 -), where each carbon is surrounded by two carbons and two hydrogens and, thus, only single bond are involved. In this type of system, the transition between σ and σ^* orbital requires energies of more than 6 eV[31]. These energies are much higher than the Boltzmann energy at room temperature. As a result, there will be very few free charges in the excited state, and the conductivity of such system is negligible. Moreover, the σ-bond electrons are essential for the backbone cohesion: The excitations of those electrons by high-energy radiation, such as ultraviolet, might damage the polymer structure irreversibly. However, this is not the case for the, so-called, Conjugated Polymer.

Conjugated polymers are characterized by a molecular structure that features alternating single and double bonds[32]. The conducting/semiconducting properties of such class of material derive from the dimerized structure due to the Pierls instability with two carbon atoms in the repeat unit[33-35], as illustrated in figure 4a. Chemically, carbon-carbon double bonds are formed by the "hybridization" between two 2p orbitals and the 2s orbital, called hybrid sp^2 orbital[31], as one may see in figure 4b. These orbital lies on a plane, directed at 120° to one another, forming three σ molecular orbitals from the three "valence electrons". The very last "valence electron", which is located in the perpendicular p_z orbital, overlaps with the adjacent p_z electron in order to form the other hybrid orbital, known as π orbital. This orbital is spread out (delocalized) over the polymer chain.

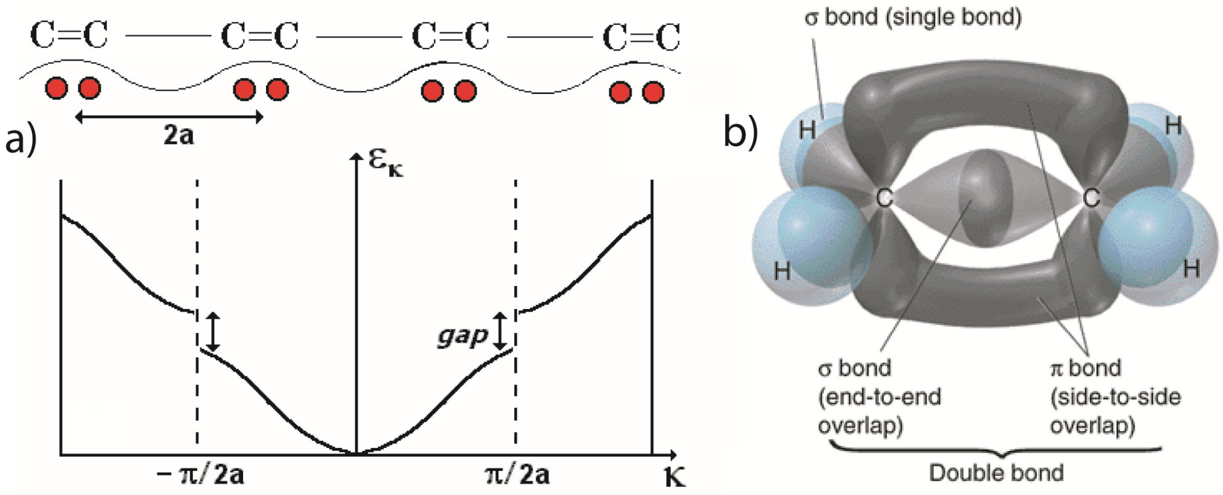

Figure 4 - a) Illustration of the main-chain dimerization due to the Peierls Instability: The band gap in polymeric systems appears since the length of single and double bound are different; therefore, the repeat unit has two atoms and the π orbital is divided in two; b) Illustration of the sp^2 hybridization: π orbital of two consecutives carbons overlaps, giving rise to a delocalized orbital, providing a "highway" for charge mobility along the polymer chain.

The lower energy π orbital is the valence band, while the high-energy π^* orbital lead to the conduction band. In other words, the π band is divided into π

and π^* bands (bounding and anti-bounding, respectively). Since each band supports two electrons, the π one is completely filled, while the π^* is empty. There will be an energy gap between the mentioned bands, which is the reason of the semiconducting properties of CP materials. Many conjugated polymers present a band gap in the range of 1 to 4 eV, which is located exactly on the visible range of electromagnetic radiation, see figure 5. This is also the reason why such class of polymer has been applied successfully to optoelectronic devices[32].

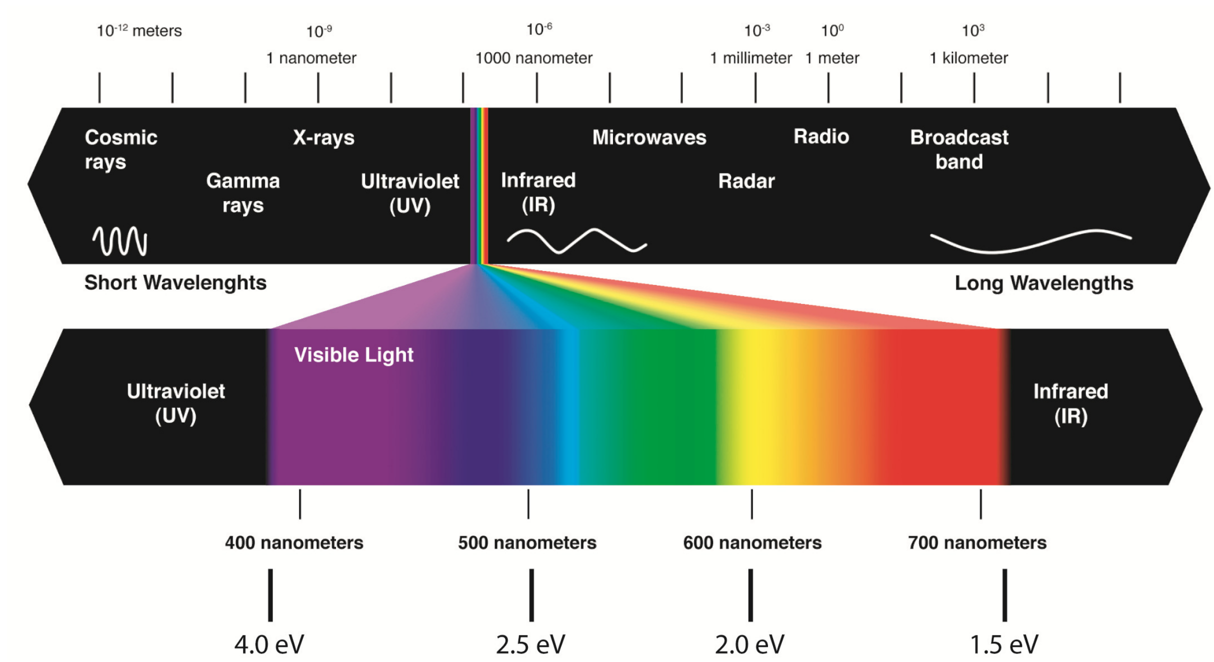

10^-12 meters
10^-9
1 nanometer
10^-6
1000 nanometer
10^-3
1 millimeter
10^0
1 meter
10^3
1 kilometer
Cosmic rays
X-rays
Gamma rays
Ultraviolet (UV)
Infrared (IR)
Microwaves
Radar
Radio
Broadcast band
Short Wavelenghts
Long Wavelengths
Visible Light
Ultraviolet (UV)
Infrared (IR)
400 nanometers
500 nanometers
600 nanometers
700 nanometers
4.0 eV
2.5 eV
2.0 eV
1.5 eV

Figure 5 – Electromagnetic Spectrum: The energy between 1 and 4 eV covers all the visible range. Most of the conjugated polymer emits light in this range of frequency, being then applied with success in optoelectronics devices.

The conducting/semiconducting properties of polymeric materials were accidentally discovered in the 1970s by Shirakawa and co-workers[36]. At that time, they were working on new ways of synthesizing polyacetylene (CH_n) by controlling its proportions of cis- and trans-isomers, as illustrated in figure 6. On one occasion, however, they added too much catalyst by mistake and found a silvery film, which turned out to be pure trans-polyacetylene. Together with

MacDiarmid, Heeger and a talented group of graduate and post-doctoral researchers, Shirakawa submitted a paper reporting that, by doping the trans-polyacetylene with iodine, one may find that the measured conductivity of such system could be a thousand times better than the undoped film[36]. Consequently, in 2000, the authors were laureate by the Chemistry Nobel Prize[37].

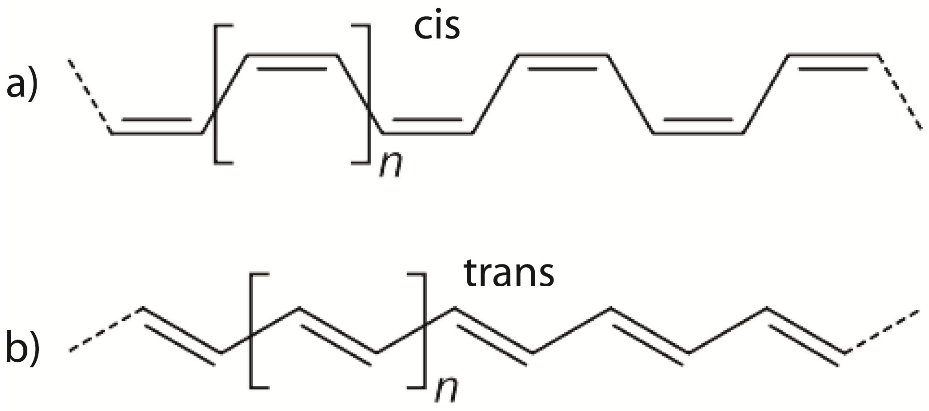

Figure 6 – Molecular structure of different polyacetylene isomers: a) the cis-polyacetylene and b) the trans-polyacetylene.

An important feature of Conjugated Polymers is their easy processing. Nowadays conjugated polymers are usually synthesized with attached alkyls side-chains, which make them soluble in convenient organic solvents, such as xylene, chloroform and toluene[8,11,13]. Therefore, film deposition can be easily obtained by low cost techniques, such as, spin-coating, whereby a drop of polymer solution is placed on a rapidly rotating substrate to form a thin and uniform film. However, the downside is that the obtained polymer morphology and chain packing structure can be extremely random, if compared with its inorganic counterparts, since polymer main-chain tends to twist and coil. Another negative factor is that the attached alkyls solubility side-chain increases the backbone separation and, therefore, reduces the intermolecular overlap[23]. This is harmful to intermolecular hopping and thus, to electrical conduction, although it is beneficial for optical properties, since intermolecular overlap promotes excimer formation[38].

1.3 Importance of Charge Transport and Its Correlation with Structure and Dynamics

The bulk state of polymer normally includes both amorphous and crystalline portions. While the amorphous polymer do not contain any crystalline region, the so-called “crystalline” polymer (generally treated as semi-crystalline), contain an appreciable amount of amorphous material[30]. When the semi-crystalline polymer melts, it normally becomes amorphous. The amorphous polymers, however, do not present melting processes, since they have no crystalline portion to quench.

The microscopic picture of an amorphous and semi-crystalline polymer is shown at figure 7. The bulk structure of an amorphous material can be linked to a pot of spaghetti, where the spaghetti strands weave randomly in and out among each other. Even being amorphous, such structure might present some order. An examination of the relative positions of adjacent strands on the spaghetti-picture will reveal that there exist short regions where the strands appear to lie more or less parallel[20].

Concerning the semi-crystalline polymer, their bulks are never totally crystalline due to the long-chain nature of polymeric materials and their subsequent entanglements. The crystallization dynamics phenomena are rather complex[30]. It might depend of several aspects, but one is important to mention. The regularity of the polymer structure plays an important role. The isotactic and syndiotactic polymers usually tend to be crystalline, whereas, atactic polymers, due to the random fashion do not (with few exceptions). An example is the high regular and semi-crystalline polyamides (nylons®).

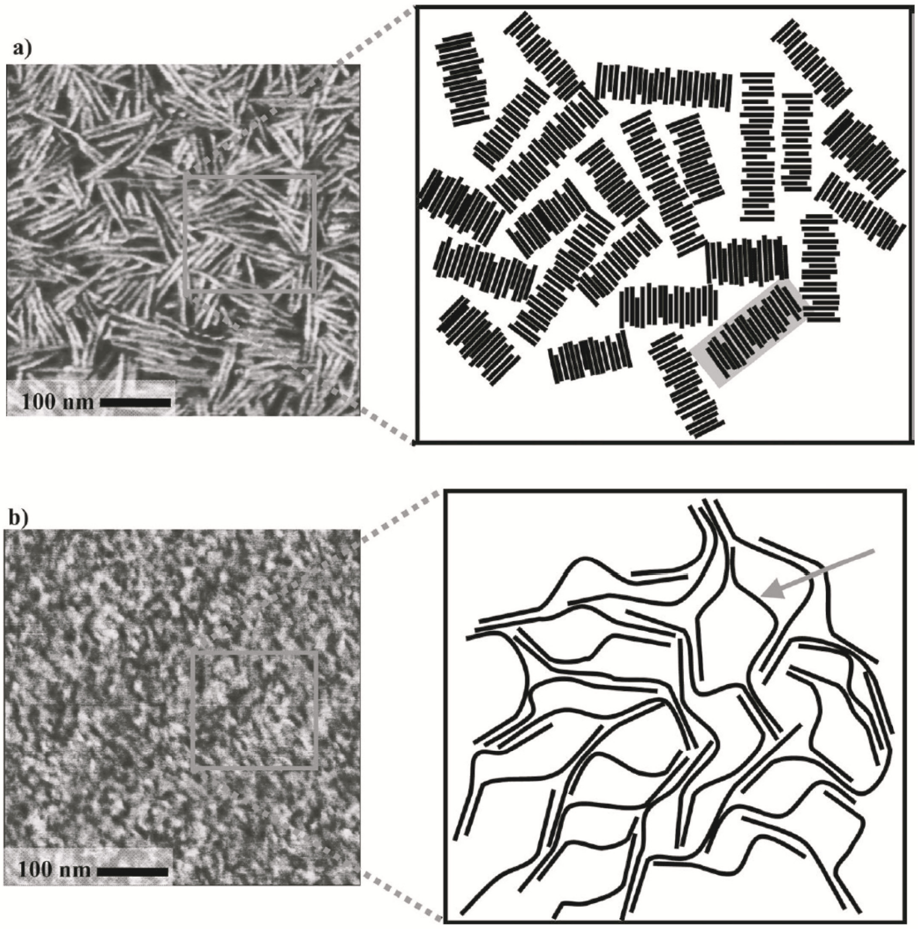

Figure 7 - Model for transport in low and high-MW films. a) Charge carriers are trapped on nanorods (highlighted in grey) in the low MW case. b) Long chains in high-MW films bridge the ordered regions and soften the boundaries. Figure adapted from reference 20.

This rich bulk state can lead to a very broaden and complex morphology and packing structure, which might strongly interfere in the electronic properties of both, amorphous and semi-crystalline polymer materials. The understanding of the electronic structure and, consequently, the charge transport is of current interest because of the success and wide-range application of conjugated polymers. As mentioned in the previous sub-chapter, it is clear that the properties of conjugated polymers depend sensitively on the physical conformation of the polymer chains. Generally, it is expected that the polymer chain packs neatly, in such a way that the π orbitals between adjacent molecules overlap efficiently. In this situation, the conduction orbital is, indeed, delocalized throughout the polymer chains and the charge carriers that are excited to this level can be readily driven out by an external electric field[39]. As a result, the charge carrier mobility increase and a better output performance can be derived.

However, this is not the situation one faces experimentally. Kline and co-worker[20], have published an interesting paper comparing the charge transport of poly(3-hexylthiophene) (P3HT) with different molecular weights (MW). The morphology analysis of the films showed that the low MW films were substantially more crystalline than the high MW (figure 7 and 8). Nonetheless, despite being more crystalline and ordered, the low-MW films presented lower mobility than the high-MW films. The answer to this apparent contradiction was based on the misorientation of neighboring crystals on low-MW films. Also, the authors have explored different processing variations, such as annealing, in order to determine whether the mobility versus MW trend was due to morphology or chain length. They found out that, for high-MW, neither the morphology nor the charge-carrier mobility have changed, while for low-MW the mobility increased hundreds of times depending on the treatment. Undoubtedly, this large variation was due to changes in the low-MW film morphology.

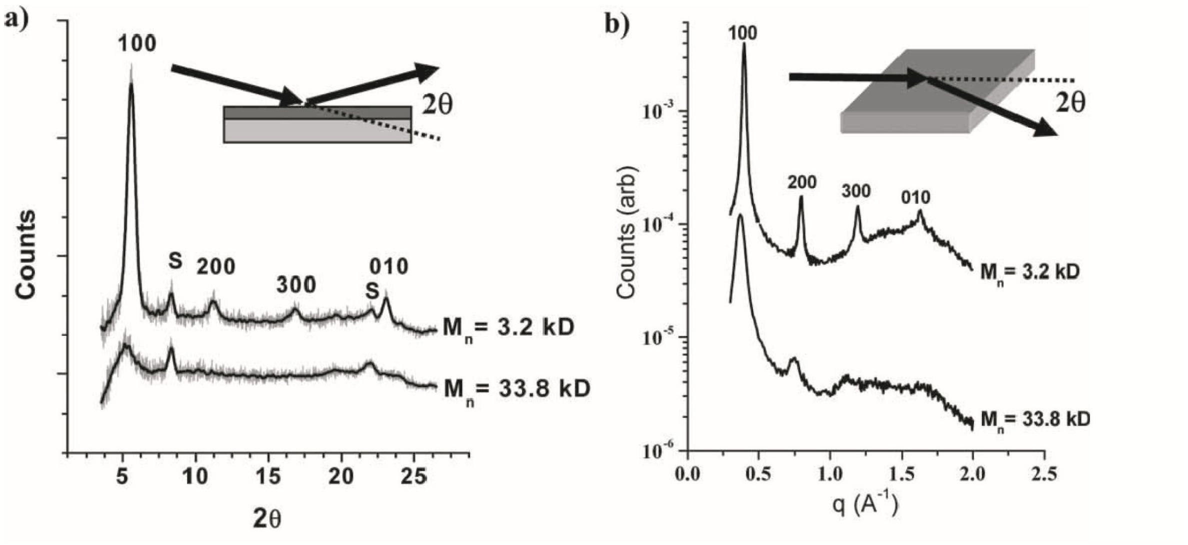

Figure 8 – X-ray analysis of a) out of plane and b) in plane diffraction of P3HT samples with different molecular weight. Note that low molecular weight films seem to produce high ordered structure. Figure adapted from reference 20.

It is not from now that annealing technique has been frequently used to achieve desired morphology and electrical properties of polymer films. Each researcher or research groups have their own assembly receipt to obtain the desired film morphology. Annealing processes involve thermal treatment designed to produce a specific transition, such as glass transition or crystal-to-crystal phase transition, (commonly addressed as crystalline transition), which promotes structural transitions and/or morphological reorientation.

Actually, it is not only the electrical properties that are influenced by film morphology or molecular relaxation. It has been shown that the photoluminescence and absorption properties were also morphological dependent[38]. Indeed, the long conjugated length can be treated as a number of smaller segments of conjugations separated by insulating defects, such as kinks and twists. Single- or small-chain molecules are expected to provide high energy decay of photoluminescence, since, excitons tend to rapidly decay, instead of diffusing throughout the conjugated chain, and, therefore, partially dissipate their energy non-radiactively. Thus, one might expect differences in the photoluminescence profile depending on the morphology and conformation.

By this introduction one may scale the importance of studying the morphology and structure of polymer films and their influence on the desired features, e.g., opto-electronic properties. In the following pages, it will be presented a more detailed discussion of this influence and correlation.

1.4 Outline of the Thesis

The historical introduction and a rapid discussion about polymeric materials, as well as the importance of understanding the correlation between molecular and optoelectronic properties, were addressed in this first chapter.

Chapter 2 deals with the description of the material and technique used throughout this research. A brief theoretical introduction is given for each technique and the most important details and discussion of the technique in question is made for the better understanding of the results of this thesis.

Chapter 3 is devoted to the presentation and initial discussion of the measurements of the molecular relaxation, dynamics and structure while chapter 4 is related to the electrical characterization of thick and thin film devices. A brief correlation between chapter 3 and 4 is established.

Chapter 5 is reserved to the main discussion of this thesis. Results presented in chapter 3 and 4 are compared and the correlation between the molecular and electronic properties of the analyzed material are outlined and discussed.

Finally, chapter 6 is dedicated to conclusions and future perspectives, while, in the last section the references cited in this work are listed.

2 Materials and Techniques

In this chapter, it will be briefly discussed the basic aspects of polyfluorene materials, the main experimental techniques and the theoretical introduction of concepts used throughout this thesis.

2.1 Material: Poly(9,9-di-n-octylfluorene-alt-benzothiadiazole) (F8BT)

As mentioned before, the first evidence of high electric conductivities in synthetic polymers was obtained with polyacetylene, which, unfortunately, is difficult to process and unstable in the presence of oxygen. However, due to the high potential for innovation of such class of materials, more stable and easy-processing polymers were rapidly investigated and developed by the chemists and researchers. This progress has led to the aromatic-based polymers, which were found to be much more stable, efficient and easier to process.

It was not surprising that the first class of light-emitting polymers was the family of polyparaphenylene vinylene (PPV)[40-43]. PPVs are fully aromatic polymers with their band gap varying from 2.0 and 2.5 eV (yellow to red color). Within this class, there were several successful PPV derivatives, such as poly(2-methoxy-5-(n-hexadecyloxy)-p-phenylene vinylene) (MH-PPV) and poly[2-methoxy-5-(2 -ethyl-hexyloxy)-1,4-phenylene vinylene] (MEH-PPV). PPVs examples are illustrated in figure 9. Numerous impressive contributions have been published using these materials, especially those by the group of Sir Richard Friend from Cambridge University, England[3-11,13,32]. Indeed, as mentioned, the pioneer works on polymer light-emitting diodes were developed by them[9]. In order to estimate the impact of this pioneer work on the literature, up to now this article has been cited more than 6000 times[44].

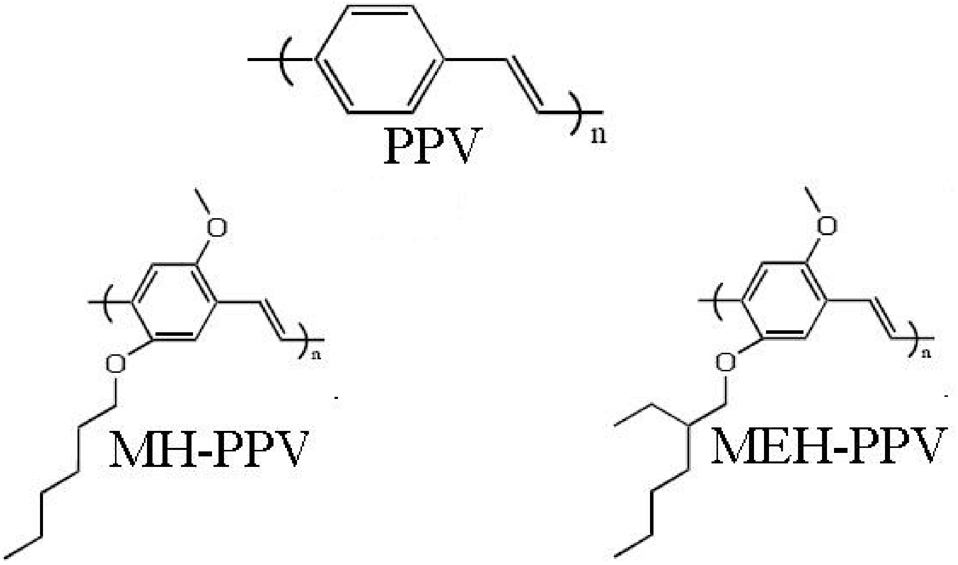

Figure 9 - Molecular structure of Polyparaphenylene vinylene (PPV) (top) and its derivatives: poly(2-methoxy-5-(n-hexadecyloxy)-p-phenylene vinylene) (MH-PPV) and poly[2-methoxy-5-(2 -ethyl-hexyloxy)-1,4-phenylene vinylene] (MEH-PPV) (botton).

However, despite being more stable and easier to process, PPVs have limited band gap, low efficiency and require high operating voltages for industrial applications. In this context, Fukuda and co-workers[45] published the development of the first polyfluorene: poly(9,9-dialkyl-fluorene)s, illustrated in figure 10a. The polyfluorene family have received considerable attention[45-58] due to its rigid biphenyl unit (which leads to a large band gap with efficient blue emission) and a facile substitution at the remote "brigde" carbon (connecting the backbone with the aliphatic species – see arrow at figure 10a), which provides the possibility to improve the solubility and assembly, without significantly increasing the steric interactions in the polymer backbone. Moreover, polyfluorenes can be synthesized together with different co-polymers, resulting in derivatives that emit lights spanning in the entire visible range with appreciable efficiency and operating voltage[45,48-51]. Examples of polyfluorene derivatives are shown in figure 10. The color of the illustration refers to the molecule's emission wavelength.

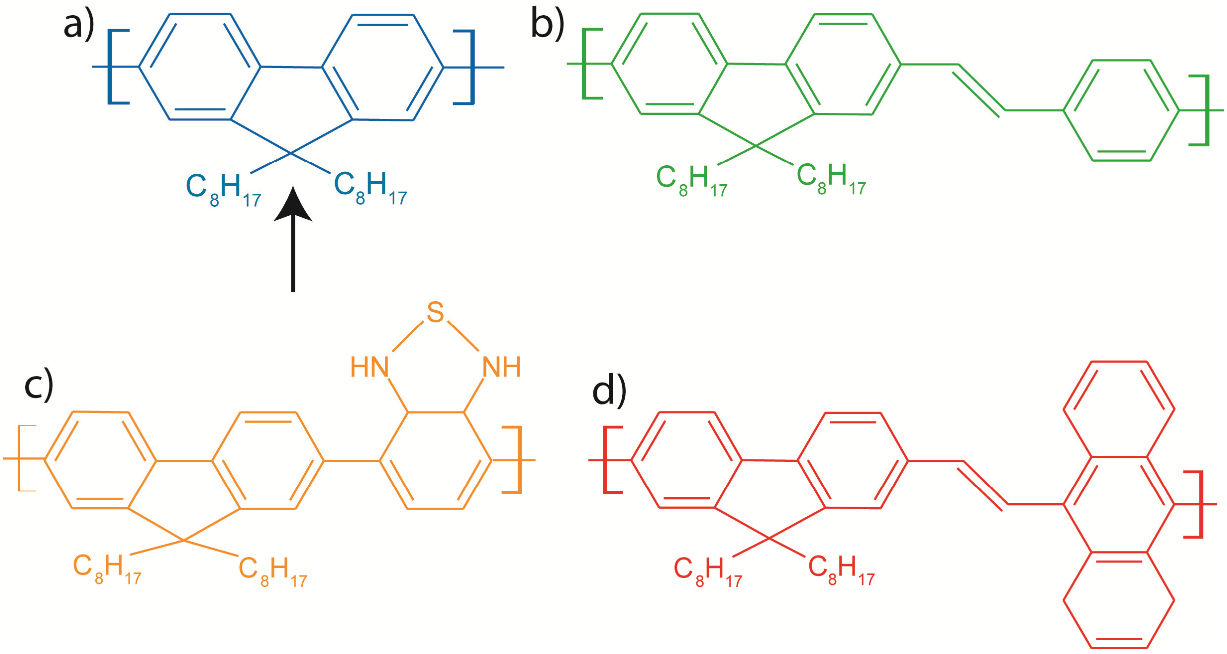

Figure 10 - Examples of several Polyfluorene chemical structure: a) Poly(9,9-dialkyl-fluorene), b) Poly[(9,9-dioctilfluorenil-2,7-diil)-co-{1,4 vinilenofenileno)], c) Poly(9,9-di-n-octylfluorene-alt-benzothiadiazole) and d) Poly[9,9-di-(2-etil-hexil)-fluorenil-2,7-diil-2,5-diphenil-1,2,4-oxadiazole].

Among the polyfluorene derivatives, poly(9,9-di-n-octylfluorene-alt-benzothiadiazole) (F8BT) has attracted special attention in the last years due to its high performance as an active layer in polymer devices. F8BT is a fluorene copolymer characterized by an alternation of the biphenyl unit with the benzothiaiazole molecule (see molecular structure in figure 10c). It has been extensively used as activity layer in reports involving highly efficient light-emitting diodes[59], photovoltaic cells[60] and, recently, the light-emitting transistors[61].

In all cases, F8BT has demonstrated high hole and electron mobility and highly efficient performance. However, the mechanisms that control the conduction of charge carriers (intra and/or interchain charge transport) are not yet well understood. These mechanisms are clearly influenced by the polymer packing structure, since many structural defects or parameters can affect the optoelectronic and charge transport properties of conjugated polymers: for instance, the interchain π-spacing, can affect the rate of charge and exciton transfer between molecules, and the torsion angle between neighboring units, might affect the planarity and effective conjugation length of the backbone.

Indeed, both the polymer structure and main-chain torsion angles are closely connected with the polymer relaxation processes[38]. The most studied relaxation phenomenon is the glass-transition. The basis for such phenomenon is the onset of collective molecular motion in the polymer main-chain. At low temperatures, only vibrational motions are possible, and the polymer is hard and glassy. At the glass transition temperature, (T_g), portions of the polymer soften and its viscoelastic behavior changes. The onset of the molecular motion specifically that in the backbone, may induce changes in the structural packing and torsion angles of the molecule and, thus, directly influence the charge transport properties.

Therefore, it is worth to studying and understanding the polymer relaxation processes and the techniques used to measure such phenomena. The next sub-chapter is devoted to relaxation measurements.

2.2 Thermal Methods

It is well known that polymeric materials undergo molecular relaxation that may interfere with their physical and chemical properties. Polymer relaxation is classified according to the temperature it normally occurs: the lower temperature processes are called γ-relaxation, and are usually associated to mobile groups, such as, methyl (CH3) ending-chain groups; the so-called β-relaxation occurs at intermediate temperature and is related to the quasi-mobile groups (aliphatic segments); and, finally, there is α-relaxation, which occurs at higher temperatures and refers to the rigid groups, such as the main-chain[30].

For semi-crystalline polymers, the α-relaxation is usually related to the reorientation of the crystalline portion, while the higher temperature process is the crystalline-amorphous transition (melting).

Throughout the work analyzed here, we have used mainly two techniques to measure the F8BT's molecular relaxations, namely: Differential Scanning Calorimetry (DSC)[30,62] and Dynamical-Mechanics Thermal Analysis (DMTA)[30,38,62].

The DSC yields peaks relating to endothermic and exothermic transition and shows changes in the heat capacity of the analyzed material. The technique also provides quantitative information of the first order transitions. Essentially, the DSC is a measurement of the difference in the heat flow rate between the analyzed sample and the reference-sample, while they are subjected to a controlled temperature program. When the analyzed material undergoes relaxation, it absorbs or supplies heat from/to the system, and causes a change in the DSC signal. It is worth mentioning for future interpretation, that the glass transition in DSC measurements is identified when the signal baseline shifts from its original level. The crystallization process is normally exothermic, while the melting is expected to be endothermic. Figure 11 illustrates a typical curve for polymer material.

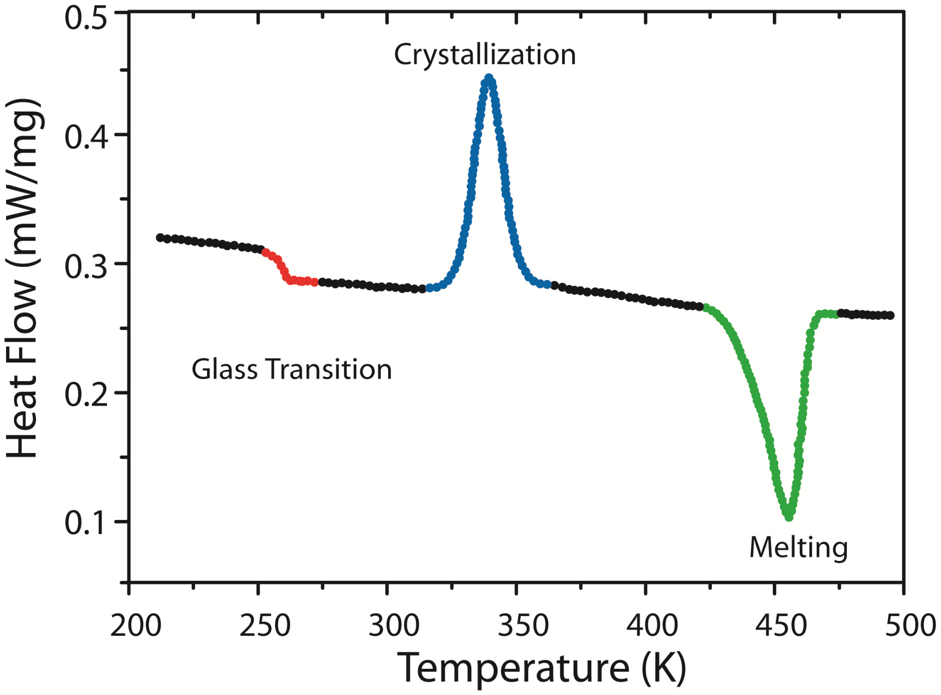

Figure 11 – Example of Differential Scanning Calorimetry (DSC) experimental results on Polyethylene polymer film: Glass Transition (T_g) in red, crystallization in blue and the melting of the ordered structure in green.

The DMTA measurement is, as well as the DSC, a powerful technique to measure and detect molecular relaxation. Indeed, the DMTA can be even more precise than the DSC[63]. It also has a practical advantage: as it involves time-dependent excitation (with different frequencies), which offers the possibility of frequency selectivity.

The DMTA technique determines the Young Modulus of the material by applying a mechanical-tension excitation[63]. The real part of the Young Modulus is denoted as Storage Modulus (*E'*), while the imaginary part is known as Loss Modulus (*E''*). Technically, the storage modulus is a measurement of the energy stored elastically during a deformation, and the loss modulus is a measurement of the energy converted to heat or absorbed by the analyzed system.

Another quantity which is widely used is the Loss Tangent:

$$tan\delta = \frac{E''}{E'} \qquad (10)$$

where δ is the angle between the in-phase and out-of-phase components in the cyclic motion.

The determination of the Young Modulus by the DMTA technique is made by the measurement of the δ phase. A frequency-controlled dynamic stress is applied to the testing sample and the correspondent material's deformation phase and amplitude response is measured. When the material undergoes a relaxation process its viscoelasticity properties change. Consequently, there will be a change in the δ phase. For instance, the maxima of tanδ versus temperature curve, and also of E'', are generally used as the definition of the glass transition (Tg). DMTA is a thermal analysis technique, which means that the measurement occurs under controlled temperature scanning.

As an example the dynamic mechanical response of polyethylene is illustrated in figure 12. The higher temperature tanδ peak is attributed to the glass transition, while the intermediate-temperature peak to the, so-called, β-relaxation (onset of motions of the side-chain in branched polymers). The lower-temperature peak, assigned as γ-relaxation was regarded as the relaxation of ending-chain methyl groups. This schematic DTMA polymer response will be useful for the analysis of our DMTA results.

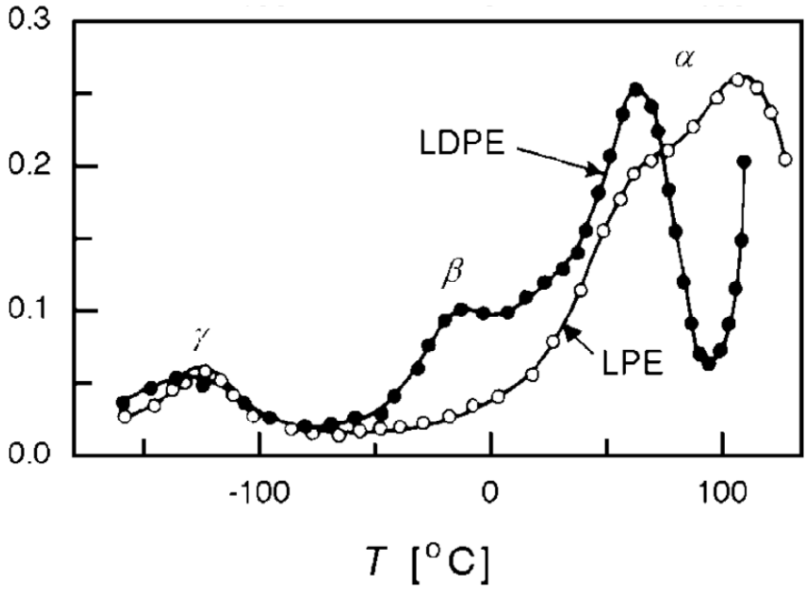

Figure 12 - Temperature dependent of the loss tangent measured by Dynamical-Mechanics Thermal Analysis (DMTA) on Polyethylene polymer film: γ, β and α are the relaxation of different segments on the molecule. Figure adapted from reference 62.

The thermal analysis techniques presented above are essential for location the temperature of the relaxation; nonetheless, they are limited to provide a clear microscopic view of the behavior of molecules and atoms during such a transition. To compensate for this, we have used Nuclear Magnetic Resonance (NMR) techniques, as discussed below.

2.3 Nuclear Magnetic Resonance Technique (NMR)

The phenomenon of nuclear magnetic resonance is generally observed in nuclei having now-vanishing total angular momentum, $\vec{J} = \hbar\vec{I}$, where $\hbar = \frac{h}{2\pi}$, being h the Plank constant and $\vec{I}$ the nuclear spin[64]. Such phenomenon arises due to the Zeeman Effect, in which a split in the spin energy levels is observed in the presence of a static magnetic field ($\overrightarrow{B_0}$). In the case of protons (spin moment: I = 1/2), the Hamiltonian of the interaction between the spin magnetic moment and $\overrightarrow{B_0} = B_0\hat{z}$ is:

$$H = -\vec{\mu}_I.\overrightarrow{B_0} = \hbar(-\gamma B_0)I_z = -\hbar\omega_0 I_z \qquad (2)$$

where $\vec{\mu}_I = \gamma\hbar\vec{I}$ is the nuclear magnetic moment, γ is the giromagnetic ratio and ω_0 is the Larmor frequency. The allowed values of the z-component of I_z are:

$$I_z = m, \qquad m = I, I-1, \ldots - I \qquad (3)$$

where m is the spin magnetic quantum number. For a nucleus of spin $I_z = \frac{1}{2}$, the possible energies are calculated according to the following expression:

$$E = \pm\frac{\hbar}{2}\gamma B_0 \qquad (4)$$

Hence, if an electromagnetic radiation of frequency $\nu = \frac{\Delta E}{h} = \hbar\gamma B_0$ is applied to a sample containing a collection of nuclei with $I_z = \frac{1}{2}$, this radiation can be absorbed by the sample, which results in transitions between the energy levels given by equation 4. This is the basic phenomenon of Nuclear Magnetic Resonance (NMR).

Though the naive discussion above applies to a single spin, it is easily to generalize to the macroscopic magnetization, which is defined as the total magnetic moment:

$$\vec{M} = \sum_i \vec{\mu}_i \qquad (5)$$

When a macroscopic sample is placed in an external magnetic field, the nuclear magnetic moment of individual $\frac{1}{2}$-spins can align in one of the two possible energies given by equation 4. Therefore, the total macroscopic magnetization will be given by the ratio of the populations of the two "orientations". At room temperature, the population of spins in the lower energy level, N^+, slightly outnumbers the population in the upper level (N^-). This ratio is given by the Boltzmann distribution, and for room temperature is approximately 10^{-6}. Indeed, the NMR signal is due to only this small fraction of net population.

At equilibrium, the net magnetization vector lies along the direction of the applied magnetic field and is called the equilibrium magnetization (M_o). In this configuration, the Z component of magnetization, M_Z, is equals M_o, and there is no transverse (M_X or M_Y) magnetization. It is possible to disturb this equilibrium situation by applying an oscillating magnetic field (known as $\vec{B}_1$), which is perpendicular to $\vec{B}_0$. By using frequencies similar to the Larmor frequency (in radio-frequency range - MHz), it is possible to induce energies transitions between the energy levels, changing the total equilibrium magnetization. The spins respond to this pulse in such a way that the magnetization vector rotates about the direction of the applied $\vec{B}_1$ field. The rotation angle depends on the length of time the field is on, τ, and its magnitude $\vec{B}_1$.

A 90° (or $\frac{\pi}{2}$) pulse is the one which rotates the magnetization vector clockwise by 90° about the X or Y plane (the phase of the RF pulse, defines the rotation direction). A 180° (or π) pulse will rotate down the magnetization vector by 180 degrees along the -Z axis. When $\vec{B}_1$ is turned off, the disturbed magnetization executes a precession movement about $\vec{B}_o$, which can be detected as an induced voltage to the NMR coil. This signal is known as Free Induction Decay (FID) and is the observable NMR signal.

Nevertheless, the effect of magnetic resonance is not as straightforward as described above. In real systems and molecules the nuclear resonance frequency may vary due to the spin interactions. The most important spin interactions for organic compounds are the so-called chemical-shift and the magnetic dipolar coupling. These interactions will be briefly discussed for solid systems in the next two sections.

2.3.1 Chemical Shift

The Chemical-Shift arises from the coupling of the nuclear spin and the electron's orbital movements[64,65]. These movements generate local magnetic fields in the nucleus, changing its local magnetic field. Since the magnetic resonance frequency is dependent on the resulting magnetic field over the nuclei, the NMR signals are expected to resonate with frequencies shifted from the natural nuclei Larmor frequency (γB_0). Thus, the nuclear resonance frequency depends on the chemical environment - and similar atoms placed in distinct electronic environments - and may lead to a different resonance frequency[65].

Therefore, the chemical-shift is crucial for NMR as a spectroscopy technique, since it makes possible that different chemical groups, which have distinct electronic clouds, are distinguished in NMR spectra. A classic example is ethanol (CH_3-CH_2-OH), of which the spectrum is sketched in figure 13: there are clearly three chemically distinct hydrogens. The ethanol spectra show three signals having different frequencies, which are defined by the electronic shielding in each nucleus. Moreover, an intensity ratio of 1:2:3 can be found, corresponding to the distinct hydrogens in the molecule.

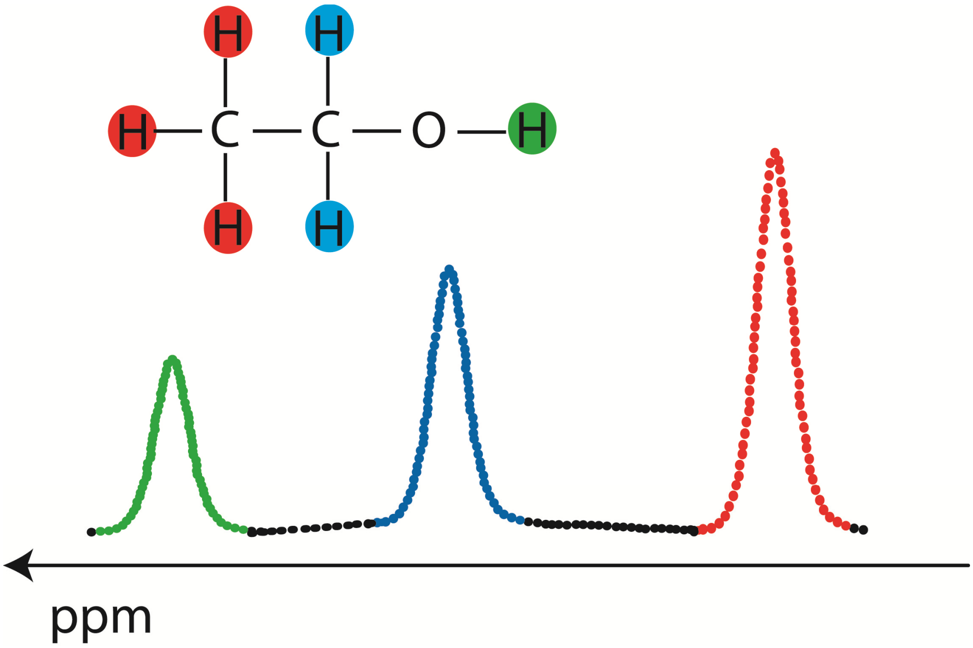

Figure 13 – **^{1}H Nuclear Magnetic Resonance (NMR) signal of Ethanol. The chemical-shifts differentiate the distinct hydrogen in the molecule: The two protons of the CH_2 group neighboring the oxygen are further to the left in the spectrum, whilst the hydrogens of the CH_3 group that is most remote from the oxygen produce a signal towards the right of the spectrum. The hydrogene attached to oxygen is 'deshielded' due to the electronegative nature of oxygen and this shifts its signal towards the left in the spectrum**

In general, the chemical shift Hamiltonian is given by:

$$H_{cs} = \vec{\mu} \cdot \left(\hat{\sigma} \cdot \overrightarrow{B_0}\right) = \gamma\hbar\left(\vec{I} \cdot \hat{\sigma} \cdot \overrightarrow{B_0}\right) \qquad (6)$$

where $\hat{\sigma}$ is a second order tensor, representing the proportionality factor between $\vec{B}_0$ and the local magnetic fields originated from the electrons' spatial orbital motion. Such movements are induced by the application of the static magnetic field (Faraday Law). Assuming that $\vec{B}_0 = B_0\hat{z}$, the chemical shift Hamiltonian results in[64,65]:

$$H_{cs} = \gamma\hbar\left(I_x\sigma_{xz} + I_y\sigma_{yz} + I_z\sigma_{zz}\right)B_0 \qquad (7)$$

The induced magnetic fields are small compared to B_0; consequently, the chemical shift parameters σ_{ij} are of the order of 10^{-6}, resulting in shifts of the Zeeman energy levels of the order of parts per million (ppm). Therefore, the chemical shift might be treated as a first-order perturbation with respect to the Zeeman Interaction and, the effective Hamiltonian can be simplified and expressed as follows[65]:

$$H_{cs} = \gamma\hbar(I_z\sigma_{zz})B_0 \qquad (8)$$

Taking into account both Zeeman and chemical shift interactions, the full Hamiltonian results in

$$H = H_z + H_{cs} = -\hbar(\gamma B_0)(1 - \sigma_{zz})I_{zz} \qquad (9)$$

Nonetheless, it is convenient to express the Hamiltonian in terms of coordinate system in which the chemical shift tensor $\hat{\sigma}$ turns diagonal. This axis frame is known as the principal axis system (PAS), or x^{PAS}, y^{PAS}, z^{PAS} and, to correlate PAS to the laboratory axis frame (LF), where the resonance frequencies are measured, it is normally used an Euler rotation, according to which:

$$\hat{\sigma}^{LF} = \hat{R}(\phi,\theta,0)\hat{\sigma}^{PAS}\hat{R}^{-1}(\phi,\theta,0) \qquad (10)$$

where, the matrix rotation $\hat{R}$ and $\hat{\sigma}^{PAS}$ are given by:

$$\tilde{R}(\phi,\theta,0) = \begin{pmatrix} \cos\phi\cos\theta & \sin\phi\cos\theta & -\sin\theta \\ -\sin\phi & \cos\phi & 0 \\ \cos\phi\sin\theta & \sin\phi\sin\theta & \cos\theta \end{pmatrix} \quad \tilde{\sigma}^{PAS} = \begin{bmatrix} \sigma_{xx}^{PAS} & 0 & 0 \\ 0 & \sigma_{yy}^{PAS} & 0 \\ 0 & 0 & \sigma_{zz}^{PAS} \end{bmatrix} \quad (11)$$

By doing so, the NMR Hamiltonian can be expressed in terms of θ and ϕ:

$$H_{cs} = \gamma\hbar I_z[\sigma_{XX}^{PAS}(\sin\theta\cos\phi^2) + \sigma_{YY}^{PAS}(\sin\theta\sin\phi)^2 + \sigma_{ZZ}^{PAS}\cos\theta^2]B_0 \qquad (12)$$

It can also be expressed in relation to the average value of the interaction, the isotropic term (σ_{iso}^{PAS}), the anisotropic factor (δ) and the asymmetry parameter (η) listed below:

$$\sigma_{\mathrm{iso}}^{\mathrm{PAS}} = \frac{\sigma_{\mathrm{xx}}^{\mathrm{PAS}} + \sigma_{\mathrm{yy}}^{\mathrm{PAS}} + \sigma_{\mathrm{zz}}^{\mathrm{PAS}}}{3} \quad , \quad \delta = \sigma_{\mathrm{iso}}^{\mathrm{PAS}} - \sigma_{\mathrm{zz}}^{\mathrm{PAS}} \quad , \quad \eta = \frac{\sigma_{\mathrm{yy}}^{\mathrm{PAS}} - \sigma_{\mathrm{xx}}^{\mathrm{PAS}}}{\delta} \qquad (13)$$

Using these values, the secular chemical shift Hamiltonian becomes:

$$H^{sec} = \sqrt{3}C\sigma_{iso}^{PAS}T_{0,0} + \sqrt{\frac{3}{2}}C\delta T_{2,0}\left[\frac{3\cos^2\theta - 1}{2} + \frac{1}{2}\eta\sin^2\theta\cos 2\phi\right] \qquad (14)$$

where C is a Constant equal to $\gamma\hbar$, , $T_{0,0} = -\frac{I_z B_0}{\sqrt{3}}$ and $T_{2,0} = \sqrt{\frac{2}{3}}I_z B_0$.

2.3.2 Dipolar Interaction

The dipolar interaction refers to the coupling between nuclear spins. This classic dipole-dipole interaction can occur among two similar spins, the so-called homo-nuclear dipolar interaction, or between two different spins, called hetero-nuclear dipolar interaction. The main feature of the dipolar interaction is that it depends on the distance between both interacting nuclei (inter-nuclear distance)[65].

Classically, the dipolar energy of two interacting magnetic moments $\vec{\mu}_1$ and $\vec{\mu}_2$ is given by:

$$E = \frac{\vec{\mu}_1 \cdot \vec{\mu}_2}{r^3} - \frac{3(\vec{\mu}_1 \cdot \vec{r})(\vec{\mu}_2 \cdot \vec{r})}{r^5} \qquad (15)$$

where r is the distance vector between $\vec{\mu}_1$ and $\vec{\mu}_2$. To express the dipolar Hamiltonian we take $\vec{\mu}_1 = \gamma\hbar\vec{I}_1$ and $\vec{\mu}_2 = \gamma\hbar\vec{I}_2$, and we assume that the gyromagnetic factors and spins might be different. By generalizing for N spins, the dipolar Hamiltonian can be represented by[64,66]:

$$H_D = \sum_{j=1}^{N}\sum_{k=1}^{N} \vec{I}_j \cdot \widetilde{D} \cdot \vec{I}_k \qquad (16)$$

where $\widetilde{D}$ is defined by

$$D_{mn=}\, \gamma_1\gamma_2\hbar^2 \frac{\vec{e}_m \cdot \vec{e}_n - 3\left(\vec{e}_m \cdot \vec{r}_{jk}/\left|\vec{r}_{jk}\right|\right) \cdot \left(\vec{e}_n \cdot \vec{r}_{jk}/\left|\vec{r}_{jk}\right|\right)}{r_{jk}^3} \qquad (17)$$

where $\vec{e}_1$, $\vec{e}_2$, and $\vec{e}_3$ are the basis vectors of the coordinate system in which the tensor $\widetilde{D}$ is represented.

Taking two spins, I_1 and I_2, and expressing I_{1x}, I_{2x}, I_{1y} and I_{2y} in terms of the raising and lowering operators I_1^+, I_2^+, I_1^-, and I_2^-, and switching the Cartesian coordinates into spherical coordinates, we are able to rewrite the dipolar Hamiltonian in a convenient form:

$$H_D = \frac{\gamma_1\gamma_2\hbar^2}{r^3}(A + B + C + D + E + F) \qquad (18)$$

where

$$\begin{array}{ll} A = I_{1z} I_{2z} \left(1 - 3\cos^2\theta\right) & D = -\frac{3}{2}\left(I_1^- I_{2z} + I_{1z} I_2^-\right)\left(\sin\theta\cos\theta\right)e^{-i} \\ B = -\frac{1}{4}\left(I_1^+ I_2^- + I_1^- I_2^+\right)\left(1 - 3\cos^2\theta\right) & E = -\frac{3}{4} I_1^+ I_2^+ \sin^2\theta e^{-i2\phi} \\ C = -\frac{3}{2}\left(I_1^+ I_{2z} + I_{1z} I_2^+\right)\left(\sin\theta\cos\theta\right)e^{-i} & F = -\frac{3}{4} I_1^- I_2^- \sin^2\theta e^{i2\phi} \end{array} \qquad (19)$$

and θ is the angle between the distance vector $\vec{r}$ and $\vec{B}_0$.

The Zeeman Effect corresponds to interactions of a nuclear moment with magnetic fields of the order of 1-10 Tesla, while the dipolar interaction corresponds to interactions with a field of about 1 Gauss. Therefore, the dipolar interaction can also be treated as a first-order perturbation with respect to the Zeeman Interaction and the effective dipolar Hamiltonian can be shortened to the first two elements A and B[64-66]:

$$H_D = \frac{\gamma_1 \gamma_2 \hbar^2}{r^3}(A + B) \qquad (20)$$

If the dipolar interaction occurs among unlike spins (hetero-nuclear dipolar interaction), only the term A is necessary for the first-order perturbation calculations. Consequently the Hamiltonian is given by:

$$H_D^{hetero} = \frac{\gamma_1 \gamma_2 \hbar^2}{r^3}(3\cos^2\theta - 1) I_{1z} I_{2z} \qquad (21)$$

For similar spins (homo-nuclear dipolar interaction), both terms are included, and the Hamiltonian is expressed as follows:

$$H_D^{homo} = \frac{\gamma_1 \gamma_2 \hbar^2}{r^3}(3\cos^3\theta - 1)\left[3I_{1z}I_{2z} - \vec{I}_1 \cdot \vec{I}_2\right] \qquad (22)$$

A common property of the Hamiltonians shown in equation 21 and 22 is that they are diagonal in the I_z basis and have the same angular dependence $(3\cos^3\theta - 1)$. Furthermore, both the dipolar and the chemical shift interaction (equation 14) have, as well, the same angular dependence. Therefore, the nuclear spin interaction Hamiltonian can be generalized and re-written in a general way:

$$H^{sec} = \sqrt{3}C\sigma_{iso}^{PAS}T_{0,0} + \sqrt{\frac{3}{2}}C\delta T_{2,0}\left[\frac{3\cos^2\theta - 1}{2} + \frac{1}{2}\eta\sin^2\theta\cos 2\phi\right] \qquad (23)$$

Where, $T_{0,0} = -\frac{I_z B_0}{\sqrt{3}}$ and $T_{2,0}$ will depend on the type of the spin interaction, as organized in table 1.

Table 1 – Irreducible tensor components of the nuclear spin interaction.

Interaction	Chemical Shift	Dipolar
$T_{2,0}$	$\sqrt{\frac{2}{3}}I_z B_0$	$\sqrt{\frac{1}{6}}\left(3I_{1z}I_{2z} - \vec{I}_1 \cdot \vec{I}_2\right)$

Hence, the transition energies and, consequently, the anisotropic part of the NMR frequencies, can be written in a general form, for all spin interactions, as:

$$\omega(\theta,\phi) = \omega_{iso} + \omega_{aniso}(\theta,\phi) = \omega_{iso} + \delta\left(\frac{3\cos^3\theta - 1}{2} + \frac{\eta\sin^2\theta\cos 2\phi}{2}\right) \qquad (24)$$

The anisotropy of the internal interaction in the solid state makes NMR a unique tool for probing molecular orientation, local structure, relative conformation between sites, and molecular motion. Many of the Solid-State NMR techniques used to study these properties are based on the anisotropy of the internal interactions.

These methods allow detailed studies of dynamics occurring over a wide range of frequencies. The fast and intermediate dynamics (within the kHz frequency scale) can be characterized, to some extent, by line-shape analysis or methods that involve the correlation between dipolar and chemical shift interaction. Slow dynamics (1Hz – 1kHz) can be studied by the so-called Exchange NMR experiments, where relatively slow conformation transitions or segmental reorientations are observed due to changes in the orientation-dependent NMR frequencies.

In the following sections, some of these methods and their capability to probe molecular dynamics will be addressed.

2.3.3 Static Hydrogen Spectra (^{1}H)

The ^{1}H NMR measurements are particularly interesting, since, by a simple line-shape analysis as a function of temperature, it is possible to investigate the molecular dynamics and, therefore, the molecular relaxation processes. The analysis of the behavior of the NMR line shapes is one of the most traditional procedures for probing molecular dynamics using solid-state NMR[64].

In the case of ^{1}H NMR measurements, the dominating interaction is the homonuclear dipolar interaction (^{1}H-^{1}H), shown in equation 22. In amorphous or polycrystalline samples, the molecules, and consequently the internuclear vector are randomly oriented. Thus, the dependence of the anisotropic interaction on the molecular orientation produces a strong broadening. Besides, multi-spin effects result in a Gaussian line shape[65], in which the width is proportional to $< \delta >$, i.e., the mean of the multi-spin reorientation.

The molecular motion is normally described by its correlation time (τ_c). One might observe three situations concerning the dynamic regimes: the slow regime, characterized by $\tau_c \gg \frac{2\pi}{\delta}$, the intermediate regime ($\tau_c \approx \frac{2\pi}{\delta}$) and the fast regime ($\tau_c \ll \frac{2\pi}{\delta}$). The molecular dynamic motion affects the anisotropic term of equation 24 through the orientation of the molecule with respect to the external magnetic field. The ^1H line width, seen in figure 14, changes mainly when the motion is in the fast regime. The width spectra depend on the geometry of the molecular motion, i.e., number of jump sites, reorientation angles, etc.

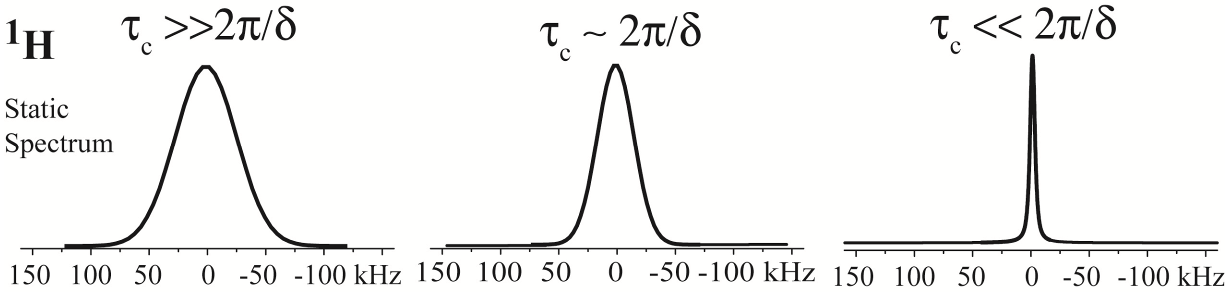

Figure 14 - Series of powder line shapes simulated for different cases: left) rigid regime, centre) intermediated regime and right) fast regime: isotropic movement. It is possible to observe that the natural motion of the molecule average the ^1H-^1H coupling, producing a narrowing of the line shape.

As the motion becomes faster, the line width narrows due to the averaging of the ^1H-^1H coupling, which is known as motional narrowing[64-67]. Therefore, by monitoring the ^1H NMR spectra as a function of temperature, one can identify the onset of molecular dynamics on the sample, simply by observing its motional narrowing.

The experiment itself is rather simple. An excitation pulse is applied in resonance with the ^{1}H, and the subsequent response is measured. The spectra are obtained for several temperatures, and the width of the line shape at half height is analyzed.

2.3.4 Excitation and Detection of Organic Compounds

The atoms and molecules in liquid samples usually execute fast and random reorientation, which average out the anisotropic component of the spin interactions, and the remaining contribution is only due to the spin interactions presenting isotropic components, i.e., isotropic chemical shift and scalar couplings[65]. Thus, solution NMR yields very narrow lines, which are normally used to analyze the chemical composition and structure of the sample.

Solid-state samples belong to a distinct physical chemistry reality. In such systems, the molecules normally have restrictions on their movements leading to a non-average (or partially average) anisotropic component of the spin interactions. Since the anisotropic components are orientation-dependent, in non-oriented samples, (i.e., amorphous or semi-crystalline), there will be a substantial distribution of the resonance frequencies, which results in a broad spectrum, making it very difficult to distinguish different carbons in the molecule based on their isotropic chemical shift difference.

In organic compounds another challenge needs to be overcome. The natural abundance of ^{13}C is just 1%, and its gyromagnetic constant is low (γ_c = 10.705

MHz/T). This usually leads to a low NMR signal and long relaxation times. Thus, to increase the resolution and sensibility of the ^{13}C NMR spectra it is necessary to use a combination of special NMR techniques, namely: ^{1}H Dipolar Decoupling, Magic Angles Spinning (MAS) and Cross-Polarization (CP). In the next sections, we will briefly describe the main feature of these methodologies.

2.3.5 ^{1}H Dipolar Decoupling

In general decoupling techniques are used to suppress the dipolar interaction between two nuclear spins. Here we shall discuss the heteronuclear Carbon-Hydrogen decoupling, which is used to eliminate the ^{13}C-^{1}H dipolar coupling during the ^{13}C acquisition, avoiding a strong spectra broadening due to the anisotropic nature of this interaction.

The most commonly used ^{1}H decoupling method consists of a continuous irradiation in resonance with hydrogen, while the carbon signal is measured. Such irradiation will artificially rotate the hydrogen's magnetization in such a way that the dipolar field in the carbon site is averaged out[68,69]. To efficiently suppress the C-H dipolar coupling the intensity of the applied irradiation field (B_1) must satisfy the relation:

$$\gamma B_1 > \Delta\omega_{dip} \qquad (25)$$

where $\Delta\omega_{dip}$ is the spectral line broadening induced by the dipolar interaction. Eventually, ones observe a residual broadening, due to the insufficient power of decoupling. The use of very high power must be avoided by employing more elaborate decoupling schemes[65,66], e.g., the so-called Two-Pulse Phase Modulation

(TPPM), where the phase of the irradiated magnetic field is alternated between +ϕ and -ϕ at each time interval of $t = \frac{\pi}{\gamma B_1}$. This improves the decoupling performance up to 30% and, was actually the decoupling method used throughout this work.

2.3.6 Magic Angle Spinning (MAS)

The Magic Angle Spinning (MAS) technique was proposed independently by Andrew and Lowe in 1959[70,71] and is a powerful method to suppress the dipolar interaction. Later, it was shown that the MAS is also able to eliminate the anisotropic component of other interactions, such as chemical shifts the and first-order quadrupolar interaction[72].

In order to understand the basic features of the MAS method, we must remind that the dipolar magnetic field produced by ^{1}H over one nearby carbon is:

$$B_{dip} \approx \left(\frac{\mu_H}{r^3}\right)(3\cos^2\theta - 1) \qquad (26)$$

The angular dependence is given by $(3\cos^2\theta - 1)$, as already shown. In order to suppress the dipolar coupling, one must choose a proper angle which eliminates the angular dependence. Hence, if $\theta_m = 54.74^o$, $[3\cos^2(54.74) - 1 = 0]$ the dipolar interaction is theoretically suppressed.

However, except for single crystals and some few materials, it is technically impossible to align every single internuclear vector in the same direction. The method used to overcome this problem consists in rotating the sample around an axis inclined at the so-called, “magic-angle” ($\theta_m = 54.74^o$), as illustrated in figure

15a. The spinning speed is normally high enough to satisfy $\nu_r > \Delta\nu_{dip}$, where ν_r is the spinning frequency and $\Delta\nu_{dip}$ is the line broadening due to the dipolar interaction. Under this condition, the nuclear spins will be all aligned around the "magic direction", yielding a null dipolar magnetic field.

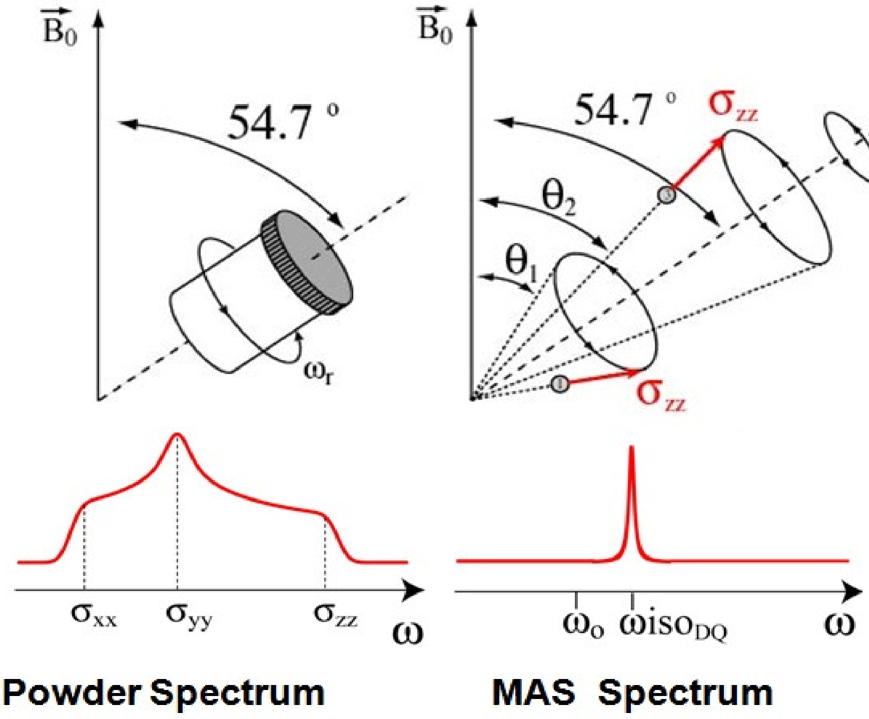
$\vec{B}_0$
54.7 °
ω_r
$\vec{B}_0$
54.7 °
σ_{zz}
θ_2
θ_1
ω_r
σ_{zz}
σ_{xx}
σ_{yy}
σ_{zz}
ω
ω_o
ωiso_{DQ}
ω
Powder Spectrum
MAS Spectrum

Figure 15 – **Schematic illustration of the Magic Angle Spinning (MAS). When no spinning is applied, the NMR signal is broad, since it is not possible to align all the internuclear vector in the magic angle direction (left); however, as shown at the right side of the figure, when a rotation of ω_r is applied, the alignment of the spin around the magic angle is achieved and a narrowing of the spectra is observed.**

As described before, other nuclear spin interactions, such as the chemical shift, have the same angular dependence as the dipolar interaction. The same procedure can be applied to suppress other spin nuclear interactions; however, it is necessary to apply a rotation, with $\nu_r > \Delta\nu$, where $\Delta\nu$ is the line broadening due to the spin interactions in question. For the dipolar interaction, $\Delta\nu_{dip}$ ranges from 1 to

100kHz, while the anisotropic ^{13}C chemical-shift in an external magnetic field of 9.4 T, has a $\Delta\nu_{CSA}$ ranging from 1 to 10kHz.

We shall now analyze MAS in a more quantitative way. For this purpose, let us start by using the general secular Hamiltonian as in equation 23[73]:

$$H^{sec} = C\left(T_{0,0}R_{0,0} + T_{2,0}R_{2,0}\right)$$
$$= \sqrt{3}C\sigma_{iso}^{PAS}T_{0,0} + \sqrt{\frac{3}{2}}C\delta T_{2,0}\left[\frac{3\cos^2\theta - 1}{2} + \frac{1}{2}\eta\sin^2\theta\cos 2\phi\right] \qquad (27)$$

In order to introduce the effects of MAS, we have to express the $R_{l,m}$ tensor in a frame system associated to the rotor, as illustrated in figure 16, which components are represented by $\nu_{l,m}$.

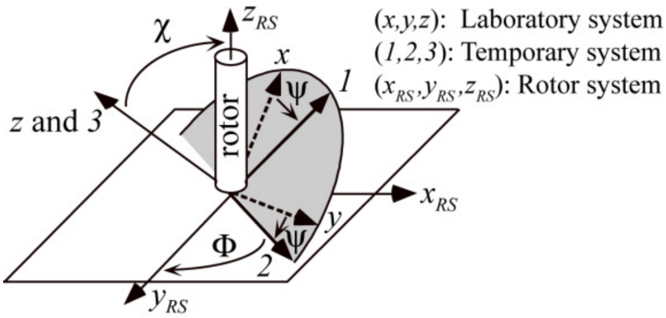
χ
z_{RS}
x
Ψ
1
z and 3
rotor
x_{RS}
y
Φ
Ψ
2
y_{RS}
(x,y,z): Laboratory system
(1,2,3): Temporary system
(x_{RS},y_{RS},z_{RS}): Rotor system

Figure 16 – Laboratory, temporary and rotor coordinate systems .

In figure 16, x, y and z are the laboratory system; x_{RS}, y_{RS} and z_{RS} the rotor system (RS) and $1,2$ and 3 the temporary system. The latter represents the transition between laboratory and rotor systems. In order to connect the laboratory and the rotor system, we have to make use of the Wigner rotation equation, given by:

$$R_{l,m} = \sum_{m=-l}^{l} \Upsilon^{\mathrm{l}}_{\mathrm{m,m}}\,(\Psi,\chi,\Phi)\nu_{l,m} \qquad (28)$$

Because H^{sec} is invariant under rotations around $\vec{B}_0$, the Euler angle, Ψ, can be chosen to be zero. The angle between the rotor spinning axis and $\vec{B}_0$, χ, will be the magic angle. The angle Φ represents the phase,($\omega_r t$), during the rotation of the sample with frequency ω_r around z_{RS}. Considering all these statements, the secular Hamiltonian can be rewritten as:

$$H^{sec} = C\big(T_{0,0}R_{0,0} + T_{2,0}R_{2,0}\big)\textstyle\sum_{m=-2}^{2} \Upsilon^{2}_{\mathrm{m,m}}\,(\Psi,\chi,\Phi)\nu_{2,m} =$$

$$CT_{0,0}\nu_{0,0} + CT_{2,0}\left[\tfrac{1}{2}(3\cos^2\chi - 1)\nu_{2,0}\right] + CT_{2,0}\left[\sqrt{\tfrac{3}{8}}\sin 2\chi\big(\nu_{2,1}e^{-i\omega_r t} - \nu_{2,-1}e^{-i\omega_r t}\big) +\right.$$

$38\sin 2\chi(\nu 2{,}2e-i2\omega rt-\nu 2{,}-2e-2i\omega rt) \qquad (29)$

Now, $\nu_{l,m}$ components can be diagonalized by a new Wigner rotation to its principal axis system (PAS), where its components are denoted by $\rho_{2,m}$ and written in the following way:

$$\nu_{l,m} = \sum_{m\prime=-l}^{l} \Upsilon^{\mathrm{l}}_{\mathrm{m\prime,m}}\,(\alpha,\beta,\gamma)\rho_{l,m\prime} \qquad (30)$$

The angles α, β and γ are the Euler angles and connects the PAS to the RS. Using the equation above we have[73]:

$$
\begin{aligned}
H^{sec} &= C\left(T_{0,0}R_{0,0} + T_{2,0}R_{2,0}\right) \\
&= C\rho_{0,0}T_{0,0} + \sqrt{\frac{3}{2}}C\delta T_{2,0}(3\cos^2\chi - 1) \\
&\times\left[\frac{1}{2}(3\cos^2\beta - 1) + \frac{\eta}{2}(\sin^2\beta\cos 2\gamma)\right] + \sqrt{\frac{3}{2}}\delta C T_{2,0}\xi(t) \qquad (31)
\end{aligned}
$$

where

$$\xi(t) = C_1\cos\omega_r t + S_1\sin\omega_r t + C_2\cos 2\omega_r t + S_2\sin 2\omega_r t \qquad (32)$$

and

$$
\begin{aligned}
C_1 &= \frac{1}{2} sin\,2\chi\, sin\,\beta\left[\cos\beta(\eta\cos 2\gamma - 3)\cos\alpha - \eta sin\,2\gamma\, sin\,\alpha\right] \\
S_1 &= \frac{1}{2} sin\,2\chi\, sin\,\beta\left[\cos\beta(3 - \eta\cos 2\gamma)\, sin\,\alpha - \eta\, sin\,2\gamma\cos\alpha\right] \\
C_2 &= \frac{1}{2} sin^2\chi\left\{\left[\frac{3}{2} sin^2\beta + \frac{\eta}{2}\cos 2\gamma\left(1 + \cos^2\beta\right)\right]\cos 2\alpha - \eta\cos\beta\, sin2\gamma sin2\alpha\right\} \\
S_2 &= \frac{1}{2} sin^2\chi\left\{-\left[\frac{3}{2} sin^2\beta + \frac{\eta}{2}\cos 2\gamma\left(1 + \cos^2\beta\right)\right] sin2\alpha - \eta\cos\beta\, sin2\gamma\cos 2\alpha\right\}
\end{aligned}
\qquad (33)
$$

From equation 31 it can be observed that, when the sample is spun around the magic angle ($\chi = \theta_m$) with frequency ω_r, the secular Hamiltonian becomes:

$$H^{sec} = C\rho_{0,0}T_{0,0} + \sqrt{\frac{3}{2}}C\delta T_{2,0}\xi(t) \qquad (34)$$

Thus, if $v_r \gg \Delta v$, $\xi(t)$ averages to zero and, $H^{sec} = C\rho_{0,0}T_{0,0}$, which is identified as the isotropic part of the spin interactions. However, if this condition $(v_r \gg \Delta v)$ is not satisfied, the spectrum will present spinning sidebands (SS). Before discussing the spinning sidebands in detail, let us illustrate how they are formed, using the ^{13}C-^{1}H dipolar interaction to exemplify this phenomenon. Normally, each individual internuclear vector $\vec{r}$ is tilted by an angle ε in relation to the z_{RS} axis, as shown in figure 17a. By spinning the sample around the magic-angle, the orientation $\theta(\omega_r t)$ of the internuclear vector relatively to $\vec{B}_0$ oscillates within the interval $(\theta_m - \varepsilon, \theta_m + \varepsilon)$. Since the ^{1}H dipolar magnetic field on the ^{13}C site depends on $\theta(\omega_r t)$ as $\left[3\cos^2\theta(\omega_r t) - 1\right]$, it will also oscillate. Therefore, the resonance frequency of each ^{13}C will oscillate periodically with a period of $t_r = 2\pi/\omega_r$, returning to the original frequency after complete a turn.

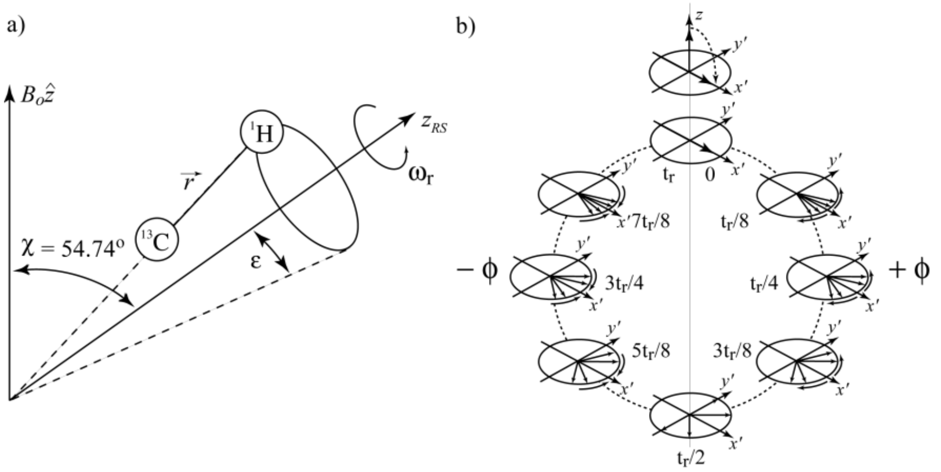

Figure 17 – a) Sample rotation with the internuclear vector aligned along a direction different from the rotation axis, b) schematic representation of magnetization dephasing due to MAS and rotational echo.

In the real case of an amorphous or polycrystalline sample, there will be ^{13}C-^{1}H pairs of which internuclear vectors will make all the possible ε angles in relation to z_{RS} axis. Hence, during the rotation period t_r, there will be an interval of resonance frequencies for each individual ^{13}C-^{1}H pair, $\omega : [\omega_{mín}, \omega_{máx}]_\varepsilon$. After the ^{13}C nuclei excitation (figure 17b) there will be a coherent transverse magnetization consisting of the vector sum of all individual ^{13}C magnetic moments, which, under

MAS, evolves with frequencies that oscillate within the specific interval $\omega:[\omega_{mín},\omega_{máx}]_{\varepsilon}$. At $t_r/2$, the ^{13}C magnetic moments will spread out on the transverse plane, resulting in a strong decrease in the NMR signal. However, at t_r, all the ^{13}C magnetic moments will have the same resonance frequencies they had after the excitation, which lead to a refocalization of the spins, as in a spin-echo experiment. This echo effect will occur after every rotation period, producing a train of echoes called rotational echoes.

The respective NMR spectrum, obtained after the Fourier transformation of this series of rotational echoes, will result not only in the spectral lines expected for each isotropic chemical shift of the ^{13}C belonging to the molecule, but also in several replicas of them. These replicas are known as spinning sidebands (SS) and are equally separated from the real isotropic chemical shift frequencies by multiples of the spinning frequency ν_r. When $v_r > \Delta v$, the rotational echoes disappear and the corresponding spectrum will contain only the isotropic chemical shift frequencies. This, together with the magic angle condition, ensures the suppression of the anisotropic components of the secular Hamiltonian.

In order to describe quantitatively the SS, let us now return to the analysis of MAS using the secular Hamiltonian under the magic angle condition[73], now only for the case of chemical shift anisotropy:

$$\mathrm{H}_{cs}^{\sec} = \hbar(-\gamma B_0)\sigma \mathrm{I}_Z + \hbar(-\gamma B_0)\delta\xi(t)\mathrm{I}_Z \qquad (35)$$

In this case, each individual ^{13}C nucleus *i* present a chemical shift resonance frequency given by

$$\omega_i = \omega_0\sigma_i + \omega_0\delta_i\xi_i(t) \qquad (36)$$

and, therefore, evolves on the transverse plane with the following phase:

$$\phi_i(t)=\int_0^t \omega_i(t')\,dt'=\int_0^t \omega_0\sigma_i dt'+\int_0^t \omega_0\delta_i\xi_i(t')\,dt' \qquad (37)$$

One important property of equation 37 is that the second integral vanishes after each rotational period, meaning that the total phase added due to the anisotropic internal interactions is zero for one rotation period. So,

$$\phi_i(t)=\int_0^t \omega_0\delta_i\xi_i(t')dt'=\int_0^{t/2}\omega_0\delta_i\xi_i(t')dt'+\int_{1/2}^{t}\omega_0\delta_i\xi_i(t')dt'=0 \qquad (38)$$

and $\phi_i(t)=\omega_0\sigma_{iso}t_r$. Therefore, under MAS the phase accumulated due to the chemical shift anisotropy is zero, and only the evolution under the isotropic chemical shift remains.

Although the broadened lines are often not desired, the spin interactions can also provide very useful information. Hence, it is usually employed the so-called "Recoupling of Anisotropies"[64-66], which consists in a set of pulses to reintroduce, for a certain period of time, the anisotropic component of spin interactions which should be averaged by MAS. From equation 38, the accumulated phase acquired over one MAS rotational period vanishes. Thus, the recoupling of the anisotropies can be achieved by applying 180° pulses spaced by half a rotation period ($t_{r/2}$). In this situation, the total phase acquired by the magnetization under this pulse sequence after a rotation period (t_r) is:

$$\Phi^{\text{rec}}=+\int_0^{t_{r/2}}\omega_n\delta_i\xi_i(t)dt-\int_{t_{r/2}}^{t_r}\omega_n\delta_i\xi_i(t)dt=2\phi_i \qquad (39)$$

This procedure can be repeated, and the total phase acquired after N rotational periods is $2N\phi_i$.

Although the theory involving the MAS indicates that the anisotropies of spin interactions are completely averaged out, it is hard to achieve such a situation in the laboratory. The MAS efficiency is closely dependent on the spinning frequency (ν_r), since one needs to satisfy $\nu_r > \Delta\nu_{INT}$, with $\Delta\nu_{INT}$ being the line broadening due to the spin interaction. As mentioned, the $\Delta\nu_{CSA}$, due to the chemical shift, ranges from 1 to 10 kHz. Thus, it is reasonable to achieve a spin rotation of tens of kHz with conventional NMR probes, and, therefore, it is not difficult to completely average out the chemical shift. However, the dipolar interaction has an intensity of $\Delta\nu_{DIP}$ ranging from 10 to 100 kHz. In this case, it is not easy to reach an ν_r of hundreds of kHz, and the averaging of the dipolar interaction via MAS is not fully efficient, even though recent high-cost NMR probes are able to reach MAS frequencies of 70kHz.

2.3.7 Cross Polarization (CP)

As mentioned, it is quite difficult to measure high resolution experimental spectra in solid samples, especially those with low abundance nuclei (e.g, ^{13}C) and low gyromagnetic constants. To overcome this problem, it is common to use the method known as Cross Polarization (CP). Such method is based on the transference of polarization from abundant nuclei with low relaxation times, e.g. ^{1}H, to non-abundant species, such as ^{13}C.

During the CP, the magnetization of the non-abundant species increases by a factor of, $\gamma_{\text{abundant}}/\gamma_{\text{non-abundant}}$[65,67]. In the case of ^{1}H and ^{13}C, this factor is 4. Another feature is that, by using the CP, the intervals between measurements are determined by the ^{1}H relaxation time, which is lower than that of ^{13}C. Consequently, a large number of averages can be made and an increase in sensibility is obtained.

In order to achieve the best condition for the transference of magnetization between the abundant (^{1}H) to the non-abundant (^{13}C) nuclei, it is necessary to satisfy the so-called Hartmann-Hahn condition[64-67], which is given by:

$$\gamma_H B_{1H} = \gamma_C B_{1C} \qquad (40)$$

It means that B_{1H} and B_{1C} must be applied simultaneously in such a way that the precession frequency of both nuclei is absolutely the same. As a result, transfers of resonant energy between both species occur by a mutual flip of spins.

2.3.8 Cross Polarization Magic Angle Spinning Experiment (CPMAS)

The combination of the techniques mentioned before, i.e., decoupling, MAS and CP, is used in order to converge to the well-known Cross-Polarization Magic Angle Spinning (CPMAS) experiment. It was suggested by Scheafer and Stejskal[74] in 1976, and can be considered the starting point of the High-Resolution Solid-State NMR Spectroscopy for non-abundant nuclei.

In a few words, the experiment starts with a ^{1}H excitation pulse ($\pi/2$), followed by CP pulses. Afterwards, the NMR signal is acquired under heteronuclear decoupling. The experiment can be repeated until the signal to noise ratio reaches the desired values. Throughout the experiment, the sample is kept at MAS condition. An illustration of the pulse sequence is shown below.

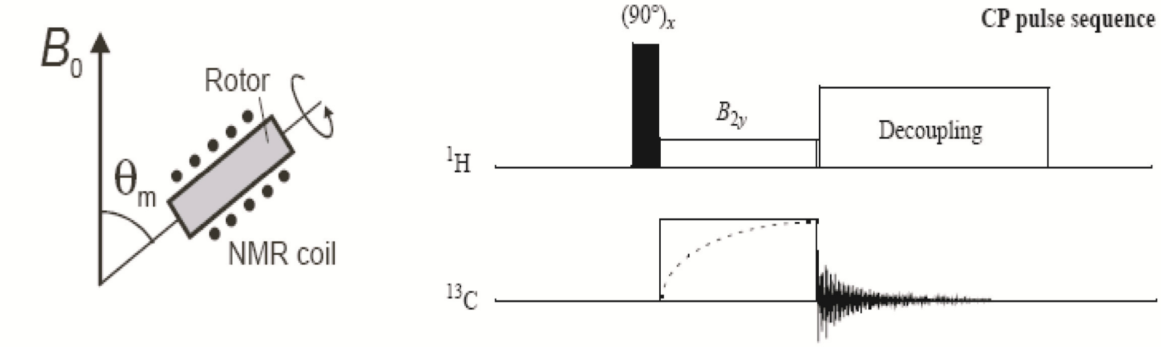

Figure 18 – Illustration of the MAS method (left) and Cross Polarization Magic Angle Spinning pulse sequence (right)

2.3.9 Dipolar Chemical Shift Correlation (DIPSHIFT)

The DIPSHIFT methodology correlates two spin interactions already discussed in this work, the heteronuclear dipolar interaction (^1H – ^{13}C) and the ^{13}C chemical-shift, and provides useful information concerning internuclear distance, torsion angles of molecular dynamics.[64-68]

Technically, the NMR spectrum acquired in this experiment is obtained under ^1H decoupling, CP and MAS. Therefore, it is possible to measure high resolution ^{13}C spectra, composed by narrow lines arising from carbons in different chemical groups. Molecular motions with correlation times higher than 100 kHz naturally average out the dipolar coupling between carbons and hydrogens, allowing the distinction between mobile and rigid segments. By comparing numerical simulation and experimental data, it is also possible to estimate both the amplitudes and correlation times of the molecular movements. Since the DIPSHIFT involves the averaging of the dipolar interaction, it is more accurate when probing dynamics of segments with intermediate to fast regimes, i.e., correlation time between 1 to 100 kHz.

The DIPSHIFT method provides a measurement of the ^{13}C-H magnetic dipolar coupling of each chemical group[75], by probing the dependence of the signal amplitude on an evolution period (t_1), where the nuclear spins evolve under the action of the CH magnetic dipolar coupling. This produces a curve $S(t_1)/S(t_1 = 0) = S(t_1)/S(0)$, which depends on the dipolar coupling strength (δ_{CH}).

The experiment involves an excitation via CP, as illustrated in figure 19a. Afterwards, the ^{13}C magnetization evolves, during t_1, under the influence of the dipolar interaction (^{1}H – ^{13}C). The time t_1 may vary from 0 to one MAS period (t_r). During t_1, it is applied a homonuclear (^{1}H-^{1}H) decoupling sequence in order to eliminate coupling between hydrogens and allow the spins to evolve only under the C-H dipolar coupling and the chemical shift interaction. During t_1, the ^{13}C magnetization is modulated by the dipolar coupling and, throughout the remaining period (t_r-t_1), a heteronuclear decoupling is applied. Immediately after one period of MAS (t_r), a carbon 180° pulse is applied, in order to produce an spin echo at $2t_r$, refocusing the chemical-shift interaction. The pulse sequence is illustrated in figure 19a.

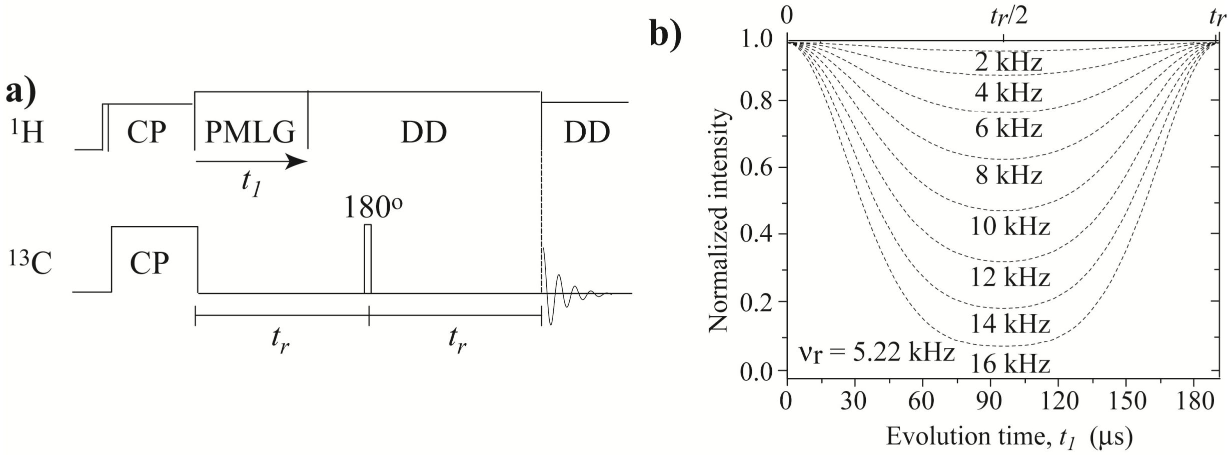

Figure 19 – a) Dipolar Chemical Shift Correlation (DIPSHIFT) pulse sequence and b) typical dependence of the DIPSHIFT curves with the dipolar coupling intensity.

After such a pulse sequence, the signal amplitude is given by:

$$S(t_1) = \langle \cos(\omega_{CH} t_1) \rangle \qquad (41)$$

where $\omega_{CH} = \frac{\delta_{CH}}{2}(3\cos^2\theta - 1)$ with $\delta_{CH} \approx \frac{1}{r_{CH}^3}$.

Therefore, by measuring the signal's amplitude as a function of t_1, one obtains a smile-like curve, (see figure 19b), which depends on the ω_{CH}. Figure 19b, presents several simulated curves for different dipolar coupling ($\frac{\omega_{CH}}{2\pi}$). The dip-in the DIPSHIFT curves is proportional to the dipolar C-H coupling, which is therefore measured in a DIPSHIFT experiment[65,75]. The more rigid the molecular movement is, the higher the dipolar coupling will be. On the other hand, the curve tends to reach the normalized value of 1, when the dipolar coupling diminishes. At this point, the dynamic is said to be at the fast limit.

The DIPSHIFT curves also depend on the correlation time (τ_C). Figure 20 illustrates simulated curves for several correlation times. It is possible to observe that the bigger τ_C is, the lower the minimum of the smile-like curve is. This means that curves with deeper minimums are related to slow molecular dynamics and, consequently, poor dipolar coupling suppression, while, curves associated with fast regimes tend to reach minimums close to the normalized value of 1.

The experimental DIPSHIFT curves can be simulated in order to derive the correlation times (τ_C) of the molecular movement. A powerful method for achieving this purpose is the Anderson-Weiss approximation (AW)[75]. The AW consists of three main approximations. The first is that the magnetic local field, due to the spin interaction, obeys a Gaussian distribution of frequencies which do not change. The local magnetic field fluctuations induced by the molecular movement are assumed to be random and the stochastic loss of correlation is described by a mono-exponential correlation function:

$$g_{therm}(t) = exp\left(-\frac{t}{\tau_C}\right) \qquad (42)$$

An extension of the AW theory was published by Clugh and Gray[77], and considers the diffusive anisotropic movement. In this case, the NMR signal due to the dipolar coupling between two spins under MAS is given by:

$$S(t) = exp\left[-M_2^{rigid}\left\{S^2\left(\frac{2}{3}f(\omega_R, 0, t) + \frac{1}{3}f(2\omega_R, 0, t)\right)\right.\right.$$
$$\left.\left.+ (1 - S^2)\left(\frac{2}{3}f\left(\omega_R, \frac{1}{\tau_C}, t\right) + \frac{1}{3}f(2\omega_R, \frac{1}{\tau_C}, t)\right)\right\}\right] \qquad (43)$$

where

$$f\left(\omega_R, \frac{1}{\tau_C}, t\right) = \frac{t\tau_C}{1+(\omega\tau_C)^2} - \frac{{\tau_C}^2[1+(\omega\tau_C)^2]}{[1+(\omega\tau_C)^2]^2} \times \left[1 - exp\left(-\frac{t}{\tau_C}\right)\cos(\omega t)\right]$$

$$- \frac{2\omega{\tau_C}^3}{[1+(\omega\tau_C)^2]^2} exp\left(-\frac{t}{\tau_C}\right)\sin(\omega t) \qquad (44)$$

and ω_R is the angular MAS frequency, τ_C the correlation time of the motion and $M_2 = \langle \omega_D^2 \rangle$ is the second moment of the Gaussian local field distribution.

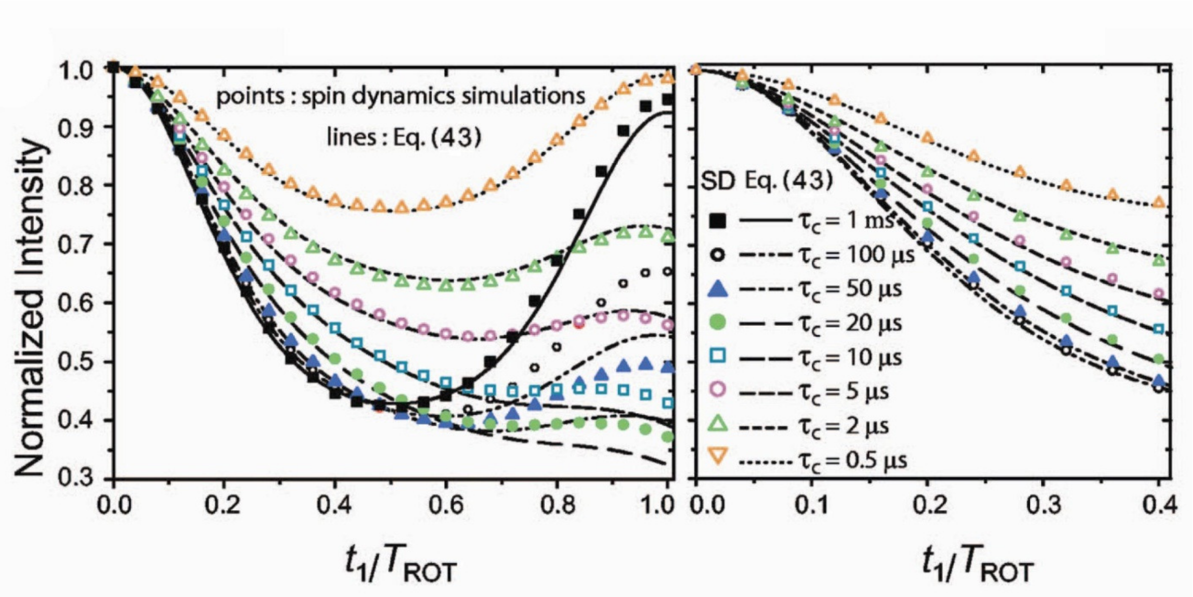

Figure 20 – Comparison between the spin dynamics simulation (points) and equation 43 (lines): Anderson and Weiss approximation fits fairly good until $t_1/t_r = 0.5$.

The equations above allow us to calculate the MAS signals under the effect of molecular movements. However, due to the approximations made by the AW theory, it not is adequate to fit the DIPSHIFT curve throughout the range of t_1 (see figure 20). Nonetheless, it works well until $t_1/t_r = 0.5$. A recent article[75] has compared the full spin simulation with AW approximation for DIPSHIFT curves. The conclusion was that, for $t_1/t_r < 0.5$, the AW approach can be used to extract the correlation time with good accuracy, even though the motion is not fully isotropic.

2.3.10 Centerband-Only Detection of Exchange (CODEX)

The CODEX technique is a NMR methodology which belongs to a set of experiments known as Exchange[64-68]. Essentially, the Exchange methods measure changes in the molecular orientation by probing the orientation of the chemical-shift tensor, which occurs in the time scale ranging from seconds to milliseconds. Consequently, Exchange methods are appropriate to probe low molecular dynamics with movements raging from 0.1 to 1 kHz[64].

Quantitatively, during an Exchange experiment, an excitation pulse is applied to the nuclei which shall be used to probe the motion. In our case, we excited the ^{13}C nuclei using a CP excitation pulse. Afterwards, the transversal magnetization is left to evolve during a period of time (t_1). Such an evolution occurs with a NMR frequency of $\Omega(\theta_1, \phi_1)$, which depends on the PAS orientation of the anisotropic spin interaction relative to that of the external magnetic field ($\vec{B}_0$) during t_1. Subsequently, a $\frac{\pi}{2}$ pulse is applied, and the magnetization is stored along the the z-axis (parallel to $\vec{B}_0$), where it should freely evolve for a period, called mixture time (t_m), without the influence of the spin interaction, since the NMR Hamiltonian commutes with the operator I_z. Then, a $\frac{\pi}{2}$ pulse is applied again, and the magnetization is moved to the XY plane (perpendicular to $\vec{B}_0$). The NMR signal is acquired during the period t_2, being characterized by a NMR frequency of $\Omega(\theta_2, \phi_2)$.

If no molecular reorientation motion has happened during t_m, $\Omega(\theta_1, \phi_1) = \Omega(\theta_2, \phi_2)$; otherwise, the NMR frequencies will be different (see figure 21). Hence, by comparing the NMR frequencies before and after t_m, it is possible to obtain information concerning the molecular reorientation occurring within this period. A general scheme of the pulse sequence is illustrated in figure 21(top). Note that, when using the ^{13}C chemical shift anisotropy to probe the molecular dynamic, heteronuclear decoupling needs to be applied during the evolution (t_1) and detection (t_2) times, to ensure that the spin evolution will be only due to the ^{13}C chemical shift anisotropy.

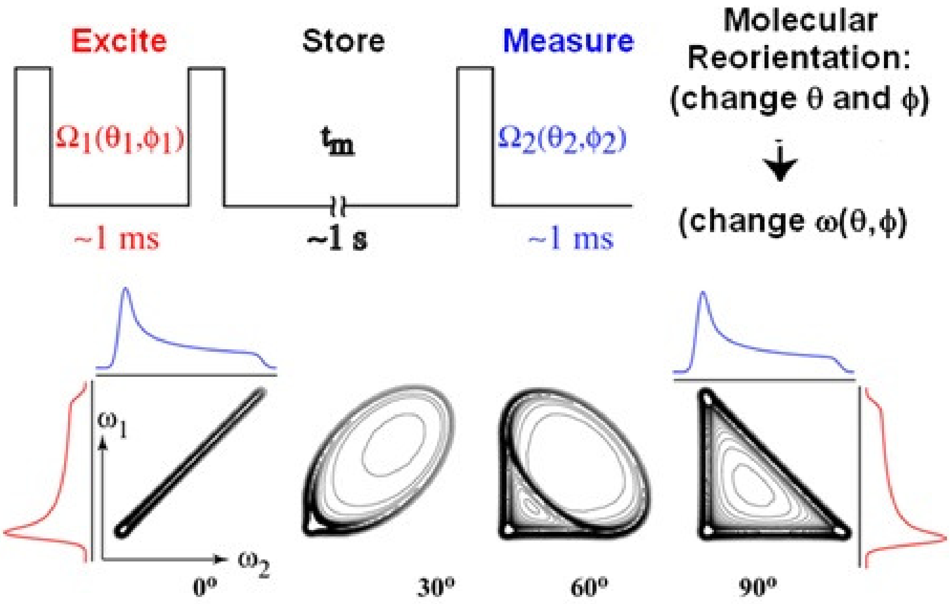

Figure 21 – Top: Exchange NMR sequence and; Botton: examples of the 2D-signal for several reorientation angles.

The Exchange methodologies were initially developed for static experiments, i.e., without MAS, since the magic angle spinning averages the anisotropic terms of the spin interactions and, therefore, the angular information on $\Omega(\theta_1,\phi_1)$ and $\Omega(\theta_2,\phi_2)$. Nevertheless, without the MAS it is not possible to measure high resolution ^{13}C NMR spectra. In this sense, the CODEX[78] technique has been suggested to overcome this difficulty, by reintroducing the chemical-shift anisotropy during MAS, using the traditional scheme called recoupling, already described in section 2.2.4.2.

In this thesis, we have used a variant of the CODEX sequence known as Constant Time Recoupling of Anisotropies (CONTRA)[80]. The pulse sequence for the CONTRA variant is shown in figure 22a:

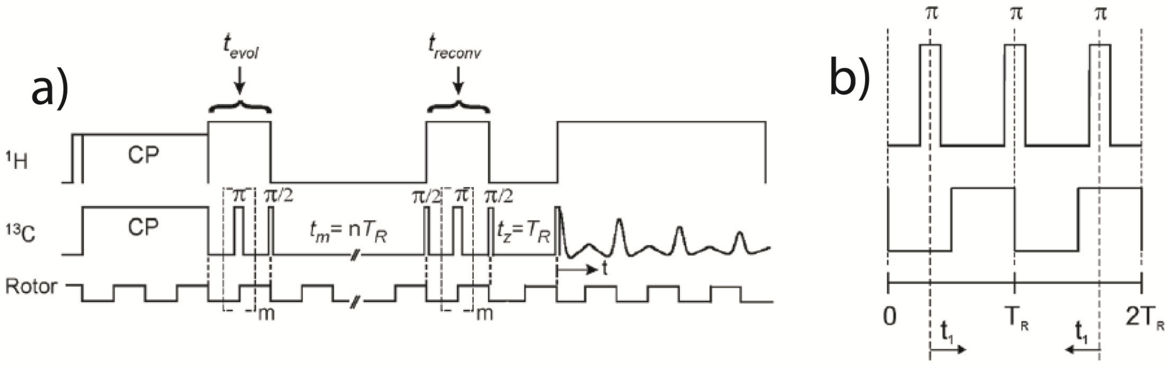

Figure 22 - Pulse sequences of the CODEX experiment. Pulse-moving scheme of the CSA recoupling periods t_{evol} and t_{reconv} for (b) CONTRA scheme. The length of the mixing period tm must be actively synchronized with the MAS rotation. Adapted from reference 80.

After cross-polarization, the magnetization evolves, during t_{evol}, purely under the anisotropic chemical-shift, which is reintroduced, even under MAS, by a series of 180° pulses. Then, following the idea of the Exchange method, the magnetization is stored along z-axes for the mixing time t_m. It is worth noticing that t_m is synchronized with the MAS rotation time (t_r). Subsequently, the magnetization is moved to the xy-plane for the second evolution time (t_{reconv}). The chemical-shift is once again re-coupled by a series of 180° pulses. Finally, the NMR signal is measured.

Quantification is performed by taking line intensities of the NMR spectrum obtained after applying the pulse sequence, (S), and subtracting it from the corresponding intensities obtained in a reference spectrum, (S_0) . The reference spectrum is acquired in such a way that no molecular motion effects are encoded, but it has the same intensity reduction due to relaxation effects as the S spectra. The intensity difference obtained for each individual line in the spectra is then normalized ($\Delta S/S_0 = (S_0 - S)/S_0$) and plotted as a function of t_m or t_1, producing a curve that depends on the correlation times (t_m dependence) or on the reorientation angle (t_1 dependence) of the slow molecular motion, as illustrated in figure 23.

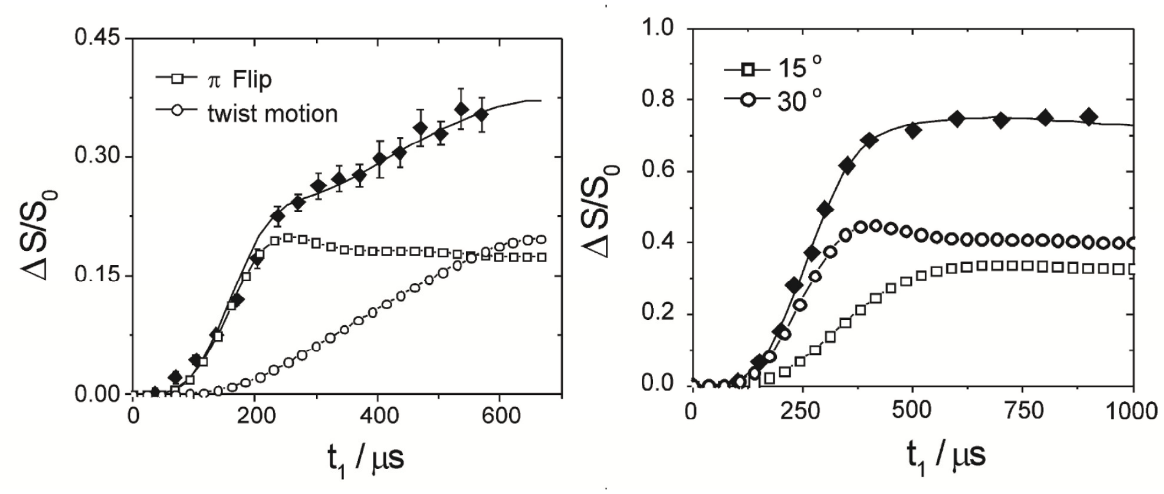

Figure 23 – Left) Experimental (full symbols) and calculated data (open symbols, full line) for the PMMA COO group and Right) Experimental (full symbols) and calculated data (open symbols, full lines) for the OCH3 (top) and CH3 (bottom) groups in methyl rhamnose glass. Adapted from reference 80

2.4 X-Ray Measurements

The main reason to study the structure of different materials is to investigate basic concepts such as their unit cells. Considering polymers, how could one fit their long-chain structure into unit cells that were known to be only several angstroms in size? The answer is that, besides being macromolecules, microscopically the polymer mers tend to organize and pack and, consequently, one may propose an adequate unit cell[30,38,62]. X-Ray diffraction has been widely used for such a purpose in polymer science; however, it requires highly developed modeling and simulation procedures. Moreover, depending on the polymer, the 3D structure analysis can be extremely difficult.

Despite the extraordinary possibility of interpreting and modeling X-Ray diffractions, it is worth mentioning that the treatment and interpretation used to evaluate the X-Ray results of the work presented here are rather superficial. Essentially, the X-Ray method was chosen because it gives a direct and broad overview of the polymer structure and its modifications as the temperature changes. Our main goal was to probe and follow the structure evolution of F8BT polymer film under several temperature conditions. Nevertheless, important aspects for understanding the X-Ray measurement and our future results are discussed below.

The most widely used measurement to deal with crystalline substances is the X-Ray diffraction. X-rays are high-energy electromagnetic radiation, with wavelengths ranging from 0.1 to 100 Å; however, the wavelengths used for polymer investigations vary from 1 to 3 Å. The phenomenon of diffraction occurs when the electromagnetic radiation reaches microscopic gratings or structures with the same size of its wavelength. The diffraction angle depends on the relation between the size of the measured structure and the wavelength of the radiation. If such wavelength is shorter than the structure, the diffraction angle is small. On the other hand, if both sizes are comparable, the diffraction angles increases.

By considering crystals as reflection gratings for X-rays, Bragg derived his famous equation for the distance (d) between successive identical planes of atoms in the crystal[30]:

$$d = \frac{n\lambda}{2sin\theta} \qquad (45)$$

where λ is the X-ray wavelength, θ is the angle between the X-ray beam and the atomic or molecular planes and n is the diffraction order, which can be any integer number.

The propagation direction is normally known as $\vec{\kappa}_i$ (for the incident beam) and $\vec{\kappa}_d$ (diffracted or scattered beam). Based on these vectors, it is of great use to describe the diffraction in the reciprocical space. In this description, the diffracted vector ($\vec{q}$) is written as:

$$\vec{q} = \vec{\kappa}_d - \vec{\kappa}_i \qquad (46)$$

The modulus of such subtraction is $q = 2\vec{\kappa}_i \sin(\theta)$, in which, together with the Bragg equation yields:

$$q = \frac{4\pi}{\lambda} \sin(\theta) \qquad (47)$$

where we have used $\kappa = \frac{2\pi}{\lambda}$.

This is a convenient expression, used by most X-ray experts, since one can eliminate the wavelength dependence, resulting easy to compare X-ray data, even when acquired with different equipment and wavelengths. Normally, the x-axis of standard X-ray data is expressed by the vector q, which is correlated with the real Bragg distance d, by the simple expression:

$$d = \frac{2\pi}{q} \qquad (48)$$

The diffraction of crystalline materials results in diffractograms with spots and sharp rings, as illustrated in figure 24a. Amorphous materials also diffract X-rays, but such diffraction is much more diffusive and the diffractograms contain broad rings, called halos. These features are illustrated in figure 24b.

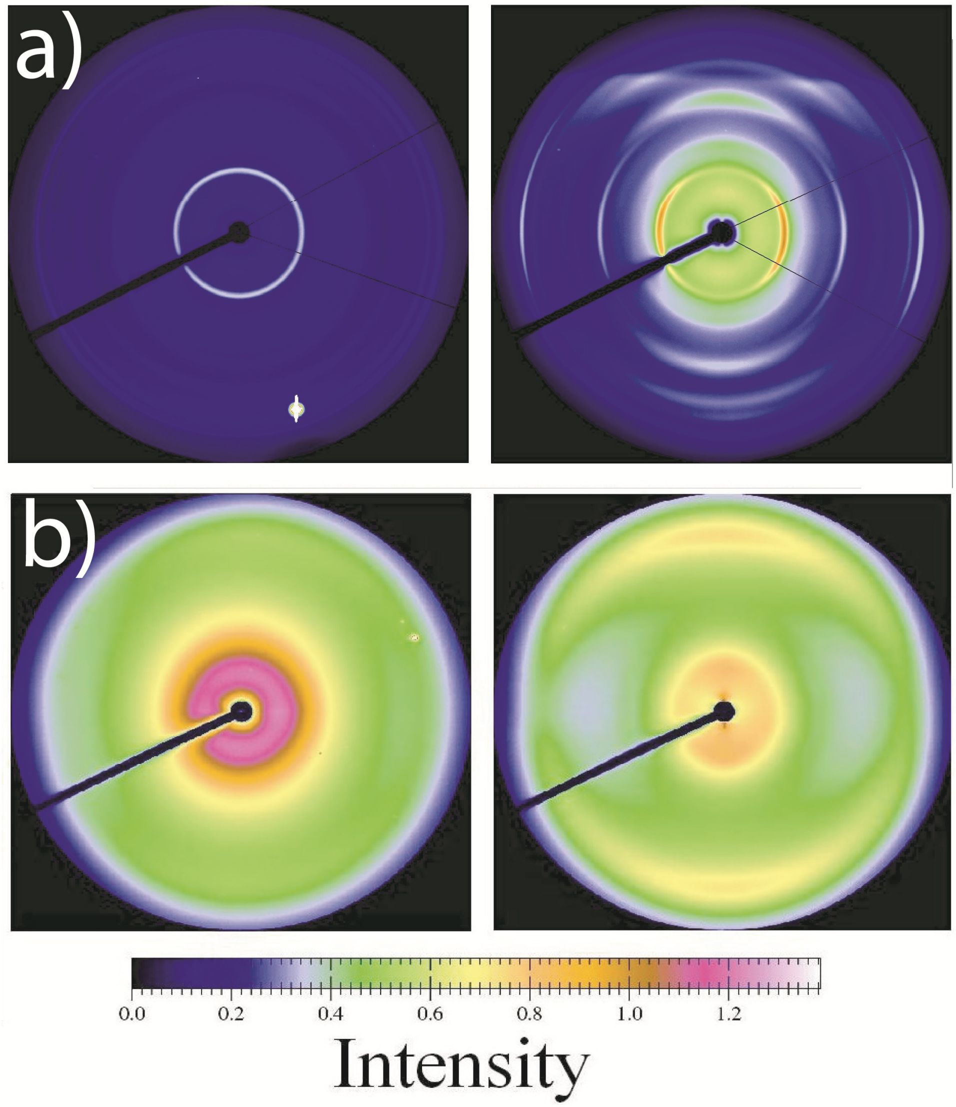

Figure 24 – Example of 2D X-Ray Diffractograms of a) Semi-crystalline with spots and sharp rings and b) amorphous polymer characterized by broad and diffusive rings.

Although X-Ray can elucidate the 3D structure of many systems, mainly those purely crystalline, the main reason for the using of X-Ray diffraction is because it allows one to identify the presence of ordered structures and to observe possible changes in them, as a function of temperature, for instance. In favorable cases, specific types of molecular packing can be identified with a simple analysis of the peak position.

2.5 Electric Measurements

The charge transport on conjugated polymers has been studied for more than two decades. The principal aim of these studies is in the development of the conductivity (σ) and charge-transport mobility (μ) in such semiconducting polymer for device applications. The conductivity is fairly straightforward to measure. In the simplest case, the resistance between two electrodes is measured and converted into conductivity. The charge-carrier mobility can be measured directly or indirectly, but whatever the method, its measurement is slightly more complicated than that of conductivity[39].

Nonetheless, the conductivity and charge carrier mobility are correlated by the following basic equation:

$$\sigma = ne\mu \qquad (49)$$

where n is the charge carrier concentration and e is the elementary charge (e = 1.602 x 10^{-19} C). The value n is complicated to evaluate, since it may vary during the measurement, mainly due to bimolecular recombination and charge-trapping processes (capture of charge carrier).

Despite the complexity of measuring, analyzing and modeling the electrical properties of conjugated systems, in the following sub-chapter we present the concepts ideas of the techniques and also the details of analysis and modeling used in this thesis.

2.5.1 Current versus Voltage Measurements (IxV)

The well-known IxV measurement is one of the most used techniques to characterize both organic and inorganic devices. The measurement itself is rather simple: a stepwise voltage is applied to the electrodes and the subsequent current is registered. The measurement is conducted using a regular voltage-source/current-meter.

Despite the simplicity of the method, the data analysis is normally complicated. The current measured may have a contribution from charges injected by the electrodes and accumulated within the bulk. Moreover, bulk processes, such as charge carrier traps and recombination, increase the difficulty of analyzing and modeling the results.

Traps in polymeric systems are quite controversial. One of the most accepted theories for traps formation is the Polarons Model (MP)[2,30]. Essentially, it says that the lattice is polarized around by a specific charge. Such a polarization acts moving the surrounding atoms and, consequently, trapping the charge by electrostatic interactions. Therefore, the trapping energy or, the Energetic Density of State, (distribution of the trapping energy state), depends on polymer morphology and structure. Technically, the lower-energy traps are known as “Shallow-traps”, while the higher-energy traps are known as “Deep-traps”.

In a semi-crystalline polymer, the boundary between the crystalline and amorphous portion can also act as charge trapping, due to the considerable disorder transition in this interface. Therefore, semi-crystalline polymers can lead to a lower conductivity because of this strong trapping region (crystalline-amorphous interface), an effect akin to the Maxwell-Wagner Interfacial Polarization[30].

Regarding the injection processes, two important phenomena must be cited: the thermal injection and the tunneling effect. Both phenomena occur due to the energetic barrier formed when the cathode/anode is evaporated over the polymeric material. This energetic barrier results from the difference between the metal’s work function and the polymers’s LUMO/HOMO and is known as Schottky Barrier.

The thermal injection has its origin in the thermionic effect, in which charge carriers flow over a potential energy barrier induced by heating processes. This effect was described by Owen Richardson in 1901. The tunneling effect[81] is related to the quantum tunnel-effect, where, the wave-function of a specific charge has a non-vanishing probability beyond the potential barrier. In this case, the higher the charge carrier energy is, the higher is the tunneling probability. In inorganic devices this phenomenon is known as Fowler-Nordheim Tunnel Effect. The injection current is then the sum of both contributions[81].

The steady-state conduction is assumed to be the case when neither the number of charge carriers nor the local electric field changes with time. In the simplest case, the current is given by:

$$J = ne\mu E \qquad (50)$$

Let us now assume an ohmic electrode (cathode/anode). Such electrode is the one that has no potential barrier for injection and is capable of providing an infinite supply of charge carriers. By making use of the Poisson's equation, it is possible to derive, for trap-free dielectric, the so-called Child's law[81]:

$$J = \frac{9}{8}\varepsilon\mu\frac{V^2}{d^3} \qquad (50)$$

where ε is the dielectric constant, V is the applied voltage and d is the sample thickness. The origin of the deviation from Ohm's law is the inability of the solid to transport all the injected charge. Therefore, accumulation of charge may occur, limiting the conducted current. This effect is widely known as Space-Charge Limited Current (SCLC).

If there are traps in the solid, the SCLC may decrease by several orders of magnitude. Rose and co-workers argued that neither the charge density nor the field distribution should be altered by trapping, but the equation relating current to voltage needs to be modified by a trap-limiting parameter (θ) which establishes the proportion of trapped charge to the free charge. The current density equation is then written as:

$$J = \frac{9}{8}\varepsilon\mu\theta\frac{V^2}{d^3} \qquad (51)$$

The trap-limiting parameter can be described considering that a single set of trap is located at an energy E_T below the conducting state. In the low injection limit, most traps are empty and the parameter is given by:

$$\theta = n_d \exp\left[-\left(\frac{E_T}{kT}\right)\right] / \left\{N + n_d \exp\left[-\left(\frac{E_T}{kT}\right)\right]\right\} \qquad (52)$$

where n_d is the density of states in the conduction band and *N* is the density of traps. Assuming N ≫ $n_d \exp\left[-\left(\frac{E_T}{kT}\right)\right]$, we have:

$$\theta = n_d \exp\left[-\left(\frac{E_T}{kT}\right)/N\right] \qquad (53)$$

Substituting θ in equation 51, one finds:

$$J = \frac{9}{8}\varepsilon\mu n_d \exp\left[-\left(\frac{E_T}{kT}\right)/N\right]\frac{V^2}{d^3} \qquad (54)$$

This equation refers to the Child's law for an insulator with shallow traps. As the traps are being filled, the current approaches the so-called trap-filled regime. At this point, there is a tremendous increase in the current as the last traps are filled.

The reason for the interest in SCLC lies in the wealthy information which can be obtained from the current-voltage curves. Changes in crystallinity, orientation or even tacticity can affect electrical properties. The study of the SCLC currents represents one way of tackling such effect.

When plotting the equation 54 in a log-log axes system, one expects to find a linear behavior. Unfortunately, this is not the case in real devices. The theory involving equation 54 is rather simplified and ought to be applied only to a very limited range of voltage. Moreover, during the derivation of equation 54, no electric field or thermal dependence of the mobility is considered.

Usual IxV curve in organic systems might present different conduction regimes. Figure 25 illustrate an idealization (left) and experimental IxV curves for organic crystals, such as Pentacene (right). Observe that, at least four regions can be found in a regular IxV: an Ohmic regime, in which the current is proportional to the electric field; the trap-limited SCLC regime, already discussed; the Trap-Filled regime, where all traps in the sample are filled, and finally, the trap-free SCLC. Due to its complexity, it is always a hard task to model and fit such IxV characteristics.

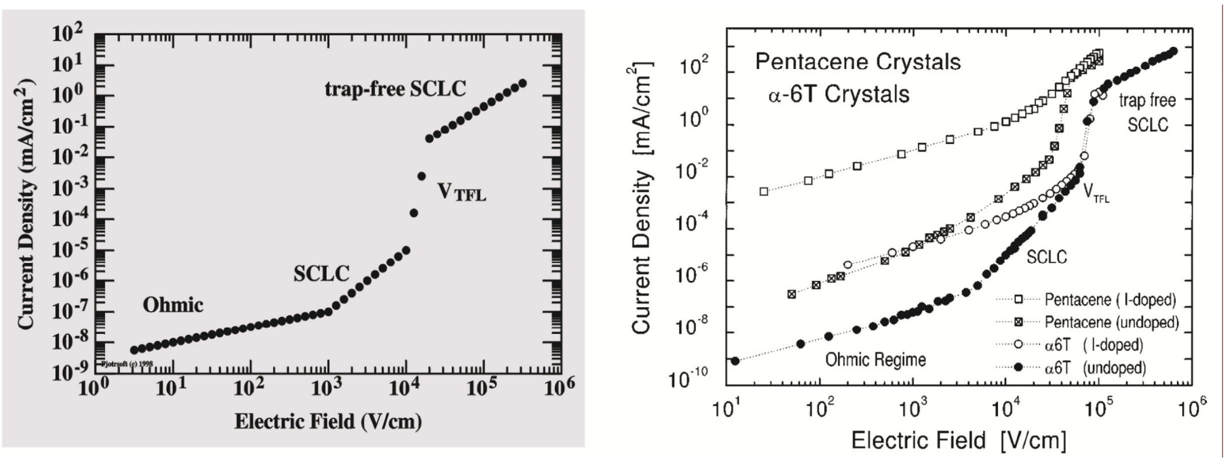

Figure 25 - Idealization (left) and real (right) Current-Voltage (IxV) characteristics for organic crystals, such as Pentacene. Observe that, four regions can be found in a regular IxV: an Ohmic regime, in which the current is proportional to the electric field; the trap-limited SCLC regime, already discussed; the Trap-Filled regime, where all traps in the sample are filled, and finally, the trap-free SCLC

There are several articles in the literature[82-85] on the improvement of the simplified trap-limited SCLC theory, and some of them shall be discussed here. The first accurate proposal was the electric field dependent mobility, as given by the equation[82,83]:

$$\mu(E) = \mu_0 e^{\gamma\sqrt{E}} \qquad (55)$$

where μ_0 is the mobility at zero field, and γ describes the "field activation" of the mobility.

In order to calculate the current density (J) versus the electric field (E) dependence, one needs to use a set of three equations: the time-independent

Continuity equation, Poisson's equation and equation 50. By solving the set of coupled differential equations, it is possible to derive the following expression:

$$J = 2\frac{\varepsilon\varepsilon_0}{L}\mu_0\frac{1}{\gamma^4}\left(6 + e^{\gamma\sqrt{E}}\gamma^3E^{3/2} - 3\gamma^2Ee^{\gamma\sqrt{E}} + 6\gamma\sqrt{E}e^{\gamma\sqrt{E}} - 6e^{\gamma\sqrt{E}}\right) \qquad (56)$$

In such equation, the free parameters are μ_0 and γ.

This is obviously an approximation. The shortcoming of such model is that it does not include bulk disorder. Moreover, no distribution function is used to describe the density of charge (n). Recent advances[86] in modeling of I-V curves consider that the charge transport in conjugated polymers is described by hopping of charge carrier over a Gaussian Density of State, which can broaden due to disorder, the so-called Gaussian Disorder Model (GDM)[21,87,88]. It also considers that the density of charges is affected by charge trapping. In this sense, the trap states are also expressed by a Gaussian distribution, and occupied by the Fermi-Dirac (FD) statistic.

Nicolai and co-workers[86] have recently published an impressive paper in which it is demonstrated that the I-V characteristics can be simulated by a trap-limited current, calculate by assuming that the occupancy of the trap distribution is given by the product of FD statistics over a Gaussian trap distribution. The calculation entails the solution of the well-known Gauss-Fermi Integral, which only recently has been approximated with accuracy[89].

The implementation of this Gaussian Trap Distribution Model (GTDM) is made assuming a drift diffusion described elsewhere[86]. Due to the complexity of implementation of the GTD model, our results will be analyzed and discussed using our simplified model; however, some results obtained by Nicolai[86] will be used to increase the level of discussion.

Another technique, which sensible to the molecular reorientation, is the Impedance spectroscopy or, simply, AC measurement. The main feature of this method is described on the following pages.

2.5.2 Impedance Spectroscopy (AC)

Impedance spectroscopy is a technique widely used in the study of electrical properties of dielectric materials, both liquids and solids[90,91]. This method is based on the measurement of the electrical response to the application of an oscillating electric field. Essentially, when the alternating voltage is applied to a dielectric material, its electrical response is normally lagged regarding the original voltage signal[90].

This lag is expressed by the electrical displacement equation, as follows:

$$D^*(\omega) = \varepsilon^*(\omega)\varepsilon_r E^* \qquad (57)$$

where D^* is the electrical displacement, $\varepsilon^*(\omega)$ is the frequency dependent dielectric constant, ε_r is the relative electrical permittivity and E^* is the electric field. Note that the signal (*) means the quantity is represented in the complex notation. The permittivity constant is a measure of the ability of a material to be polarized or not by an electric field, being defined as:

$$\varepsilon^*(\omega) = \varepsilon'(\omega) - i\varepsilon''(\omega) \qquad (58)$$

where $\varepsilon'(\omega)$ and $\varepsilon''(\omega)$ are respectively, the real and imaginary part. Similarly, as introduced in DMTA for the Young complex modulus, the real component is related to the stored energy, while the imaginary component is due to the energy lost by the system.

Experimentally, the technique in question measures the material's Impedance (Z), which can be characterized by[90] "*the ratio of a sinusoidal voltage, applied across two terminals of a measurement cell, to the sinusoidal component of the current flowing between the terminals that results from the applied voltage*". Unless the system is purely resistive, the impedance is a complex quantity, as the current will have a different phase from the applied voltage:

$$Z^*(\omega) = \frac{V(\omega)}{I(\omega)e^{-i\theta}} = Z'(\omega) + iZ''(\omega) \qquad (59)$$

where $V(\omega)$ is the sinusoidal voltage excitation, $I(\omega)$ is the measured current, θ is the phase between voltage and current and $Z'(\omega)$ and $Z''(\omega)$ are the real and imaginary component of the impedance. The material complex conductivity ($\sigma^*(\omega)$) can also be calculated by the relation:

$$\sigma^*(\omega) = i\varepsilon_0\omega\varepsilon^*(\omega) \qquad (60)$$

Based on the physical quantities introduced here, one may explore electrically the dielectric properties of several types of materials. Nonetheless, how can IS measurements be correlated with molecular relaxation?

It has been repeatedly emphasized, that working with polymers means dealing with an ensemble of chains which can exist in a manifold of conformational states. Molecular relaxation is a dynamic process where the polymer chains, or part of them, change between these states when enough thermal energies is supply to the system. In other words, the molecular chains move, and these macroscopic dynamics involves the reorientations of two types of dipoles: the permanent and the one induced by the applied electric field.

In the context of IS, it is usual to speak of dipoles in the sense of two electric charges of magnitude $+e$ and $-e$ at a small distance $\mathbf{r}$ apart. A dipole is a vector and can respond to a field by altering its length $\mathbf{r}$ or the direction of $\mathbf{r}$. The length may be $|\mathbf{r}|=0$ for zero field, when the molecule is said to have no permanent dipole (momentary dipole). The permanent dipole, on the other hand, is the one with $|\mathbf{r}| > 0$ even for $E = 0$. Some chemical compounds contain molecular grouping of well-defined permanent dipole moments, for instance $C = N$ or $C = O$. The former occurs in the F8BT molecule. In this molecular group, the positive charges are centered near to carbon and the negative ones near the nitrogen.

These dipoles may resonate with the oscillating electric field, generating the measured dipole current. The IS can be done in a wide frequency range (from 0.1 to 10^6 Hz in the case to be reported on this thesis). When the applied oscillating voltage resonates with the frequency of the molecular reorientation, part of the energy is absorbed and one may measure an increase in the dielectric loss (ε'').

For non-polar polymers, such as Polyethylene, the same phenomena might be measured, although, with lower intensity. The reason is related to the nature of the dipoles. In CH_2 the dipoles are temporary, being induced by the applied voltage. In this case, the measured energy loss is much lower, and the resonance with the molecular dynamics has smaller intensity.

The dielectric behavior of a conjugated polymer is exemplified by figure 26. At lower temperatures, the polymer shows relaxation peaks which refer to the movements of individual non-polar groups, such as CH_3 and CH_2 (γ and β relaxation). At rising temperatures, the polymer softens and the high-temperature peak appears, which is attributed to a cooperative disordering of the solid, happening mainly on the backbone (polar groups) and know as glass transition (α-relaxation). The inset in figure 25 is the Arrhenius plot. Observe that, the activation energy for the α process is higher than that for the β.

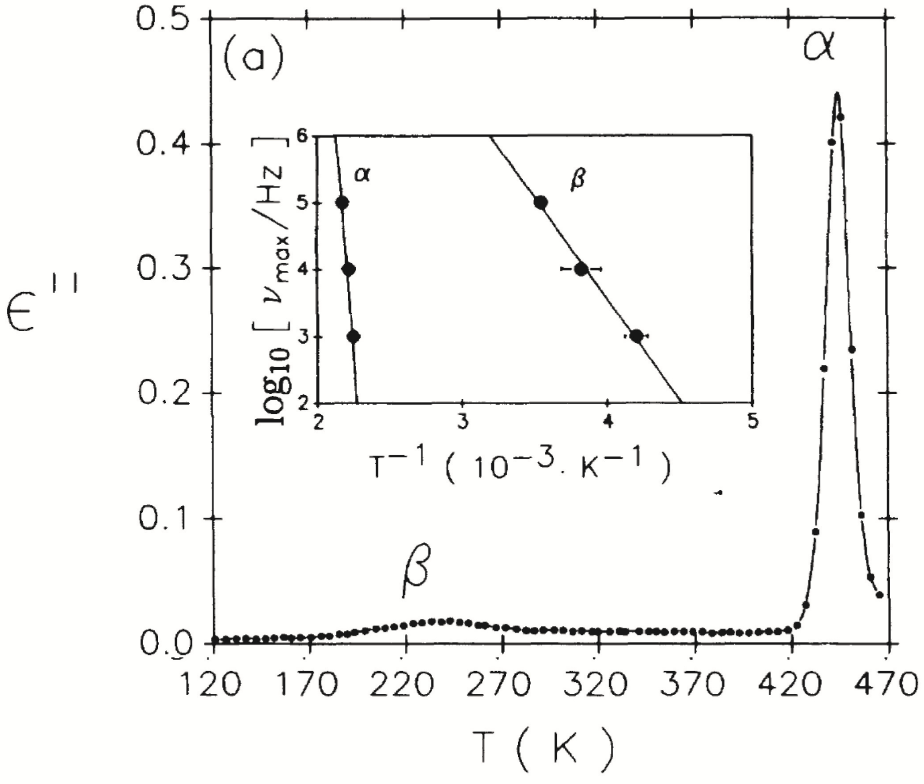

Figure 26 – Dielectric loss example for the Poly(aryletherketone). Observe the appearance of the two main relaxation processes. Inset: Arrhenius plot for both relaxations. Adapted from reference 62.

In summary, as observed in DMTA, the IS can be sensible to molecular dynamics of specific segments of the polymer chain. Such characteristic is of great importance for the work described here, since it arises as the first measurement directly connecting the electrical properties and the molecular dynamics and relaxation.

In the next sub-chapters, two types of charge-carrier mobility measurements will be discussed. The mobility seems not to be directly correlated with molecular properties as the IS is; however it provides important information about the drift of charge carrier throughout the polymer bulk. Undoubtedly, since the charge carriers diffuse within the polymer chain, their mobility must be affected by molecular dynamic processes.

2.5.3 Time of Flight Technique (TOF)

The Time of Flight Technique, or simply TOF, is a traditional method used to measure the charge carrier mobility in semiconductors or dielectric materials placed between electrodes, being at least one of them semi-transparent[2,20,39,87,88]. The technique is performed by injecting a thin sheet of charge carriers into the material. Normally, such injection is stimulated by a short laser pulse with wavelength in the absorption band of the material. Subsequently, the charge carriers injected are driven out by an applied DC potential. When the leading edge of the packet reaches the opposite electrode, a transit time transient (t_T) is measured, from where it is possible to extract the average transit time and the effective charge-carrier mobility (μ). The relation between μ and t_T is simply given by the following equation[20]:

$$\mu = \frac{d}{t_T E} \qquad (61)$$

where d is the sample thickness and E is the applied electric field. If the drift velocity of the packet is constant, a plateau in the current is observed for times below the transit time. This leads to a well-defined inflection point demarcating the transit time of the packet, as illustrated in figure 27.

In an ideal case, in which all charges propagate on a plane wave, the phocurrent should display a rectangle-like shape. However, in general, polymer materials do not exhibit such ideal rectangular transient, as shown in figure 26. The deviation from the ideal response reveals important information regarding the disorder of the system and its influence on the charge carrier transport. Several reports have dealt with such disorder transport, and many models describing it statistically and qualitatively have appeared[39,88,87].

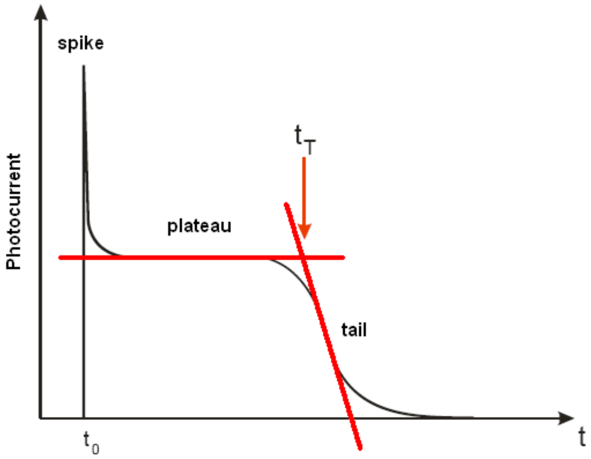

Figure 27 – Illustration of TOF transient: The intersection between the plateau and the extension of the tail is given by the transit time.

One interesting aspect of the charge carrier mobility in polymer is its temperature dependence. The temperature may interfere in the time needed for the packet of charge to achieve its dynamic equilibrium. Therefore, when the time to achieve such equilibrium is comparable to the transit time, the packet does not propagate with a constant drift velocity. Under this condition, the current transients do not show the plateau region and the transport may be described as dispersive (D). Otherwise, the transport is said to be non-dispersive (ND).

One of the transport models that have been suggested to explain the temperature dependence of the mobility was the so-called Gaussian Disordered Model (GDM). The model assumes a Gaussian Density of States and that the charge diffusion occurs via hopping processes[21,87,88]. The GDM predicts a temperature dependence of the charge carrier mobility as $\mu \propto e^{(-c\hat{\sigma}\theta)^2}$ and a ND-D transition at a given temperature T_c, where $\hat{\sigma} = \frac{\sigma}{k_B T}$ is the energy disorder parameter. This model allows us to derive two expressions for the carrier mobility: one above (non-dispersive) and another below (dispersive) T_c:

$$\mu(T) = \mu_o exp\left(-\left(\frac{2}{3}\frac{\sigma}{k_B T}\right)^2\right) = \mu_o exp\left(-\left(\frac{T_o}{T}\right)^2\right); \quad T > T_c, \qquad (62a)$$

$$\mu(T) = \mu_o exp\left(-\left(\frac{1}{2}\frac{\sigma}{k_B T}\right)^2\right) = \mu_o exp\left(-\left(\frac{T_0'}{T}\right)^2\right); \quad T < T_c, \qquad (62b)$$

where $-T_0^2$ and $-T'^2_0$ are the slopes of the $ln\mu\ vs. T^{-2}$ curve above and below T_c, respectively, being their ratio $\frac{T_o}{T_0'} = \frac{4}{3} = 1.33$.

The dispersiveness can be quantified by the spread of the transient, since the transient increases with disorder[21]. The dispersiveness parameter (W) is defined by

$$W = \frac{t_{1/2} - t_T}{t_{1/2}} \qquad (63)$$

where $t_{1/2}$ is the time for the transient to decay to one half of its plateau value.

Besides the modeling discussion, some interesting works have been published concerning the behavior of the drift mobility at the glass transition temperature. Some motivating results indicate that the charge transport is, indeed, sensible to the dynamic phenomena which occurs during the glass transition process[21,87,88]. The evidences suggest that, below the glass transition temperature the conduction is trap-controlled and, above it, the trapped charge carriers are released by the backbone molecular motion. This implies that a structural detrapping mechanism dominates the charge conduction above T_g. Such interpretation will be used in our future results.

Despite the success of TOF to extract the mobility of charges, it has limitations that must be described. Firstly, in order to prevent the redistribution of the electric field, the material's dielectric relaxation time (τ_σ) should be longer than the delay time between the application of the voltage and the light pulse. Therefore, at room temperature, relatively high bulk conductivity ($\sigma \approx 10^{-5}\ \Omega^{-1}\text{cm}^{-1}$) and short τ_σ indicate violation of the TOF.

The second and even more important limitation is that τ_σ must be longer than the transit time (t_T). If this condition is not fulfilled, the number of equilibrium carriers is sufficient for significant redistribution of electric field within times shorter than the transit time.

Finally, the last restriction is concerned to the polymer film thickness. As TOF involves light incidence, the absorption depth needs to be much smaller than the sample thickness. Otherwise, the sheet of charge is created far from the incident electrode and the drift mobility is overestimated. Therefore, sub-micrometer samples must be avoided.

In this sense, Juska et al.[92] have presented a new method to study charge transport, which overcome thickness related TOF limitations, allowing the measurements of the charge mobility of samples with thicknesses below that of TOF resolution. The method, known as CELIV (Current Extraction by Linear Increasing Voltage), is discussed next.

2.5.4 Current Extraction by Linear Increasing Voltage (CELIV)

Originally, this PhD project did not involve the use of the Photo-CELIV technique. The mobility in thin-film devices would be extracted by measuring the saturation current in thin-film organic transistors (OTFT). Nevertheless, the conduction of charge carrier in OTFT occurs between two interdigitated electrodes. Thus, the conduction plane is different from that of a conventional OLED, and it would not be straightforward to directly correlate it with IxV and IS. For this reason, during my short-term period in Darmstadt, it was proposed to Prof. von Seggern the implementation of the Photo-CELIV technique. He accepted the idea, and, together with Mr. Bernd Stoll, we assembled the CELIV technique successfully.

In the Photo-CELIV[92-94] technique, the incident nanosecond laser pulse I_0 penetrates the whole sample through the transparent electrode and is reflected by the opposite metal electrode, thereby generating photo-carriers uniformly throughout the bulk. A linear voltage ramp (LVR) is applied to the electrodes with a delay time τ_{delay} with respect to the laser pulse I_0. A stretch of the setup is illustrated in figure 28. The photo-carries are then driven out of the sample by the applied electric field, and the transient current Δj is recorded as the difference between two successive voltage sweeps. According to the literature the mobility can be calculated by the relation:

$$\mu = \frac{2d^2}{3A\tau_{max}^2\left(1 + 0{,}36\frac{\Delta j}{j(0)}\right)} \qquad (64)$$

where d is the film thickness, A the voltage rate of LVR and j(0) the displacement current. The dispersiveness of the transport is usually quantified by the ratio $t_{1/2}/\tau_{max}$, in which $t_{1/2}$ is the width at half maximum of the conduction current profile of Δj^{93}. Hence, the higher (lower) $t_{1/2}/\tau_{max}$ is, the more (less) dispersive the charge transport will be.

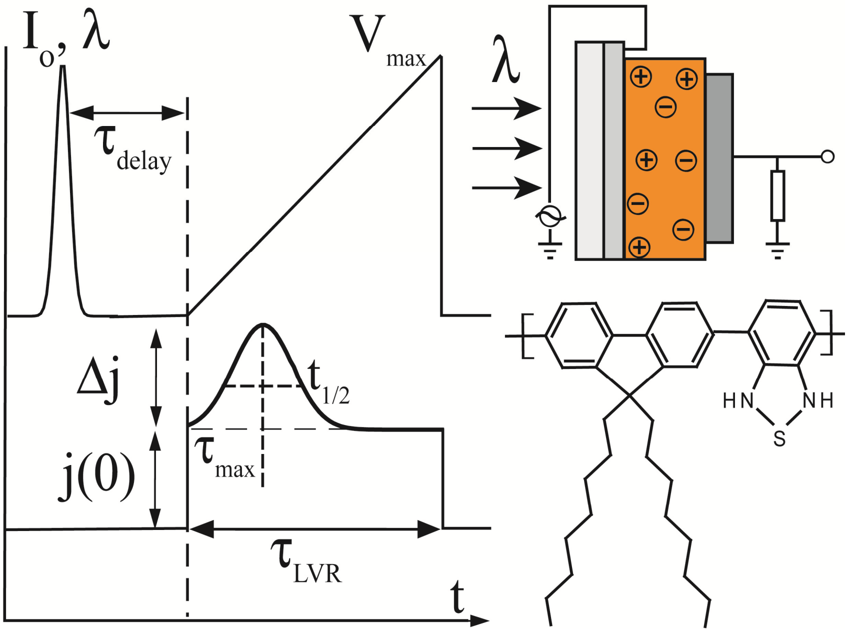

Figure 28 - Schematic illustration of the Photo-CELIV method. V_{max} is the top voltage applied; λ is the nanosecond laser pulse; Δj is the extracted transiente current; j(0) is the displacement current; τ_{pulse} is the length of the voltage pulse; τ_{delay} is the delay between the laser pulse and the voltage pulse and τ_{max} is the time at the highest current of Δj. On the right: Schematic illustration of the used device and the molecular structure of F8BT

Despite being different from it, the calculated mobility has a physical origin similar to that of TOF. Therefore, we used analysis and modeling similar to the one on the TOF section.

Although it appeared as a powerful technique, the CELIV has some weaknesses that are worth mentioning. Initially, the equation 64, used to calculate the charge-carrier mobility, was derived under certain ideal conditions which are difficult to be found in real devices. The most critical one is that the system is assumed to have a homogeneous density of equilibrium charges. In most cases, real devices exhibit non-equilibrium and inhomogeneous distribution, with holes close to the anode and the electrons close to the cathode. The non-equilibrium of both electron and holes density promotes the appearance of a phenomenon known as bimolecular recombination[93].

Bimolecular recombination is the phenomenon which occurs when two opposite charges meet one another. Such meeting annihilates them giving rise to phonons/photons of energy (heat or light). This effect can occur during the extraction of the CELIV current; nonetheless, it was not been taken into account in the analysis of the current transient by the current formalism. Bange et. al. have treated this problem in a recent publication[93]. Although the bimolecular recombination is amplified in photovoltaic cells, which is different from our case, it is important to revise the CELIV results before making further interpretations.

2.6 Film and Device Preparation

Two milligrams of purified poly(9,9-dioctylfluoren-2,7-diyl-co-benzothiadiazole) (F8BT) material was purchased from Fraunhofer Institute in Golm. The polymer chemical structure is illustrated in figure 29. The molecular weights and the polydispersivity were measured by Gel Permeation Chromatography (GPC) using polystyrene as reference. The measured values were M_n = 206 kg/mol and M_w/M_n = 3.

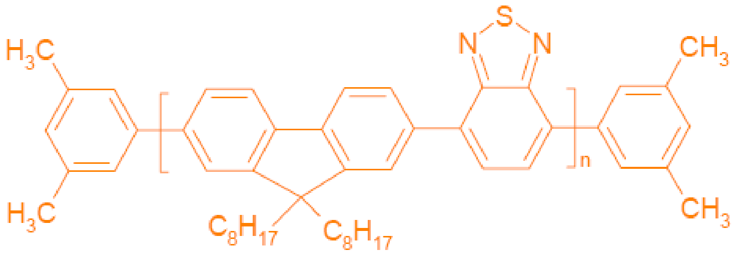

Figure 29 – Molecule Structure of the F8BT polymer material.

A 5 μm thick self-standing polymer film, used in the molecular relaxation, dynamics and structure measurements, were obtained by drop-cast deposition of a 20 mg/mL toluene solution and dried inside the Inertec AG Glove box with saturated solvent environment, in order to slow down the evaporation process. After the solvent evaporation, the samples were stored in the dark and under vacuum for several days before the measurements were performed.

For electrical measurements, light-emitting diodes with thick (4 μm) and thin (200 nm) films were assembly following these steps: Firstly, patterned ITO (20 Ω/) were cleaned by ultrasonication at 70 °C for 10 min in an alkaline soap solution (Denonex®); after rinsing in ultra-pure water, dried substrates were once again ultrasonicated at 70 °C for 10 min in acethone, and subsequently dried with N_2, finally, the cleaned substrates were treated with plasma ozone for fifteen minutes.

For thin layer devices, the film deposition was obtained by spin coating a 12 mg/ml toluene polymer solution with 1800 rpm, which was followed by a thermal treatment at 320 K for 5 min. All film deposition procedures were conducted in an inert and controlled atmosphere with an amount of O_2 and water vapor below 3 ppm.

For thick layer devices, the film depositions were obtained by drop-casting the 20 mg/ml toluene polymer solution over the cleaned substrate. Afterwards, the freshly deposited devices were stored under vacuum and in the dark for 96 hours inside the same an inert and controlled atmosphere.

Finally, 120 nm of aluminum cathode was thermally evaporated with evaporation rate of 2 Å/s at 10^{-7} Torr. The sandwich-like devices were, then, ready for measurements. A stretch of the devices built is show in figure 30.

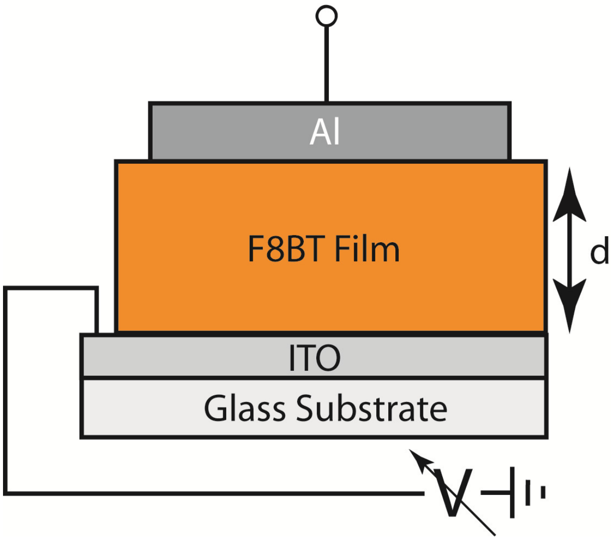

Figure 30 – Illustration of the sandwich-like devices built for the electrical measurements: The polymer films were grown on cleaned ITO substrates and the aluminum cathode were thermally evaporated.

3 Molecular Relaxation, Dynamics and X-Ray Results

In this chapter we will discuss the structural aspects of F8BT thick films obtained by DSC and WAXD, followed by the molecular dynamics results achieved by DMTA and NMR techniques. Correlations between them will be addressed.

3.1 Structural Results: Differential Scanning Calorimetry and Wide Angle X-Ray Diffraction

In order to start investigating the structural parameters and molecular relaxation processes, we firstly used the Differential Scanning Calorimetry (DSC). For this purpose, a TA Instrument DSC-910 differential scanning calorimeter was used to determine the transition temperatures of the F8BT samples. DSC experiments were conducted in two stages: a heating stage from room temperature to 570 K, followed by cooling down to 230 K. All heating/cooling rates were fixed to 10 K/min. During the measurements the samples were kept in argon environment with a flow rate of 100 mL/min.

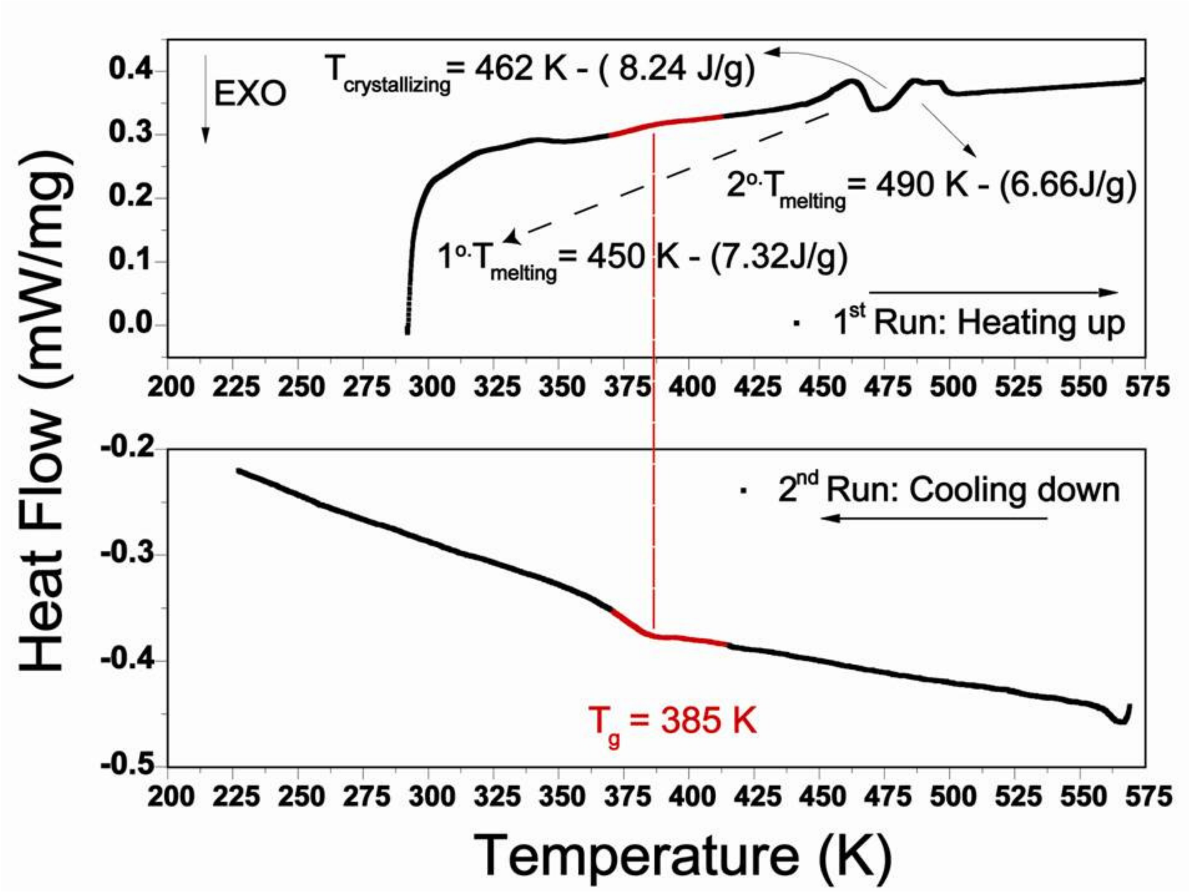

Figure 31 – Differential Scanning Calorimetry (DSC) data for F8BT polymer film; (Top) the heating and (Bottom) the cooling stage.

The DSC results are illustrated in figure 31. Both heating and cooling curves, revealed a baseline shift at T = (385 ± 10) K, which is attributed to the glass transition of the F8BT. A similar temperature had been previously measured as the glass transition point for the same material, using the same technique[95]. The second transition at T = (450 ± 10) K was registered only during the heating stage, being an endothermic process due to the melting of a pre-existent crystalline phase. Immediately after, an exothermic process, which is assigned as a recrystallization, occurs at approximately T = (460 ± 10) K. Finally, the polymer exhibits an endothermic transition at around T = (490 ± 15) K, due to the melting (T_m) into a liquid crystalline phase.

These temperatures shall be used to define the range of temperature used in the next experiments, especially those dedicated to molecular dynamics and electrical properties. However, as the molecular processes revealed by DSC involve a change of structural states, it is necessary to confirm and reanalyze such change by other measurements. For this reason, X-ray measurements are one of the most indicated methods to probe such structural parameters.

The WAXD experiments were performed at the D11A-SAXS beam line of the LNLS (Brazilian Synchrotron Light Laboratory). The wavelength used was 1.488 Å, and the sample detector distance was approximately 138.9 mm in all cases. The films were set up in two configurations: with the incident X-ray beam perpendicular (⊥) and near-parallel (//) to the film plane. The samples were examined using a two-dimensional (2D) CCD detector with 15 minutes of data-acquisition, see figure 32.

Average radial intensity profiles were obtained integrating an arbitrary 15 ° angular sector in the case of the isotropic scattering pattern (⊥ incidence) and a similar sector centered around the maximum in the oriented scattering ring (// incidence). Intensities were normalized by the integrated intensity of the bean incident on the sample during the exposure and by the sample absorption. For temperature-dependence measurements, the samples were placed in a hot stage cell specially designed for X-ray scattering measurements (THM 600, *Linkam Ltda*), see figure 32 (right). For each of the experimental geometries (⊥ and // incidences), the films were placed in a sample support adapted to the hot stage, as illustrated in figure 32. The difference between the values of the sample temperature and the values set on the controller was less than 5 K for all scans in the range 123 to 523 K, allowing a fairly precise determination of the thermal state of the sample. The *in situ* measurements were performed allowing

10 minutes of stabilization and 15 minutes of data acquisition for each desired temperature.

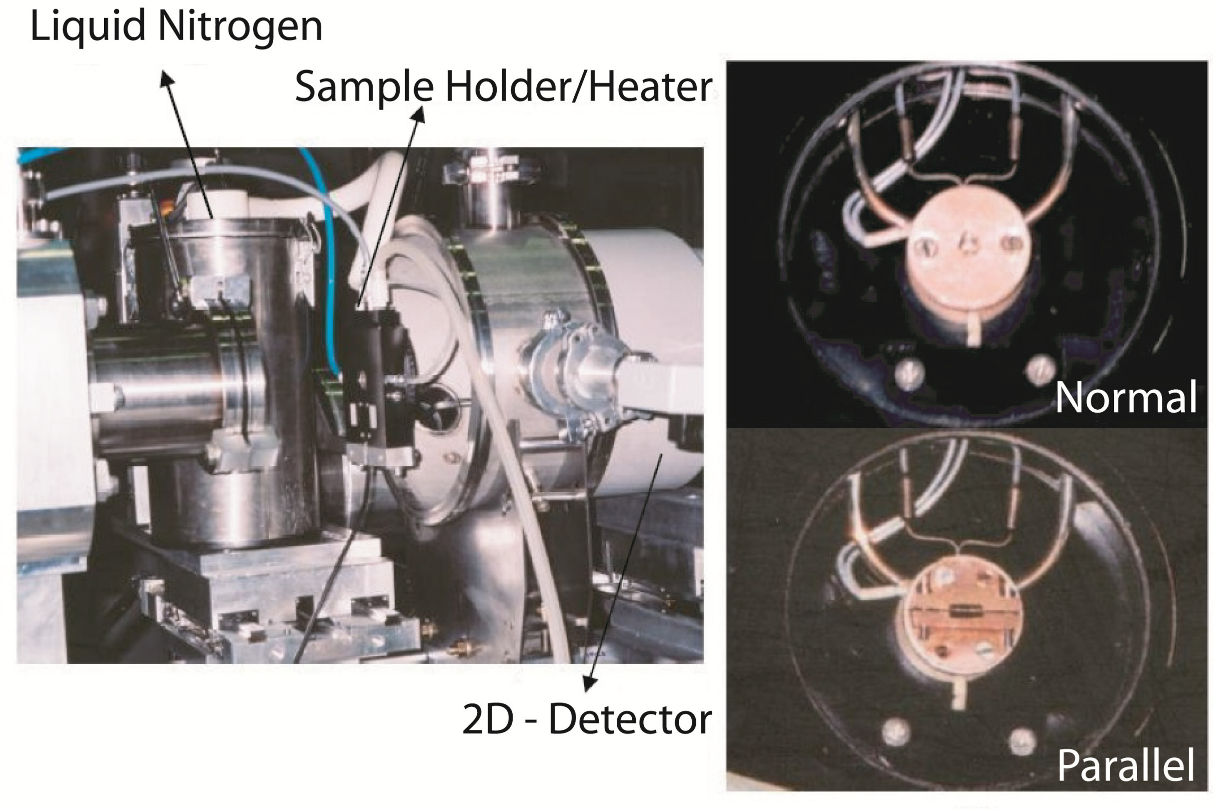

Figure 32 – WAXD measurement setup: Left) Sample holder and detector and Right) Sample holder for each of the experimental geometries (normal and parallel incidences).

The result obtained at room temperature (298 K) is shown in figure 33. The upper part illustrates the 2D WAXD images for both normal and near-parallel incidence. The normal incidence images is composed of diffraction rings with roughly uniform intensity, whereas, for near parallel incidence, one may observe small arcs and diffuse semi-rings with non-uniform intensity. This indicates the presence of an anisotropic morphology, as usually observed for films of conjugated polymers[38]. Also, the results suggest that there exits certain periodic microscopic structures, which tend to be preferentially oriented parallel to the film surface and randomly disoriented on the plane.

The correspondent 1D pattern of the 2D images is shown in the bottom part of figure 33. Three equally spaced diffraction peaks can be seen for both incidences corresponding to characteristic lengths of ($d_i = \frac{2\pi}{q_i}$): d = 16, 9.8 and 5.6 Å. Such equally spaced distance suggests that the peaks arise from different reflections order of a lamellar phase, with interplanar distances of 5.6 Å. Such distance is known as the π-stacking distance between two parallel adjacent backbones. A simple illustration of such lamellar phase is printed as an inset in the middle of figure 33. Lamellar phases of this type are usually referred to the literature as β-phase[38]. Such structure, which has been observed in several polyfluorenes and derivatives[38,103,104], is known to be highly organized, and its formation is attributed to the aging of organic solvent.

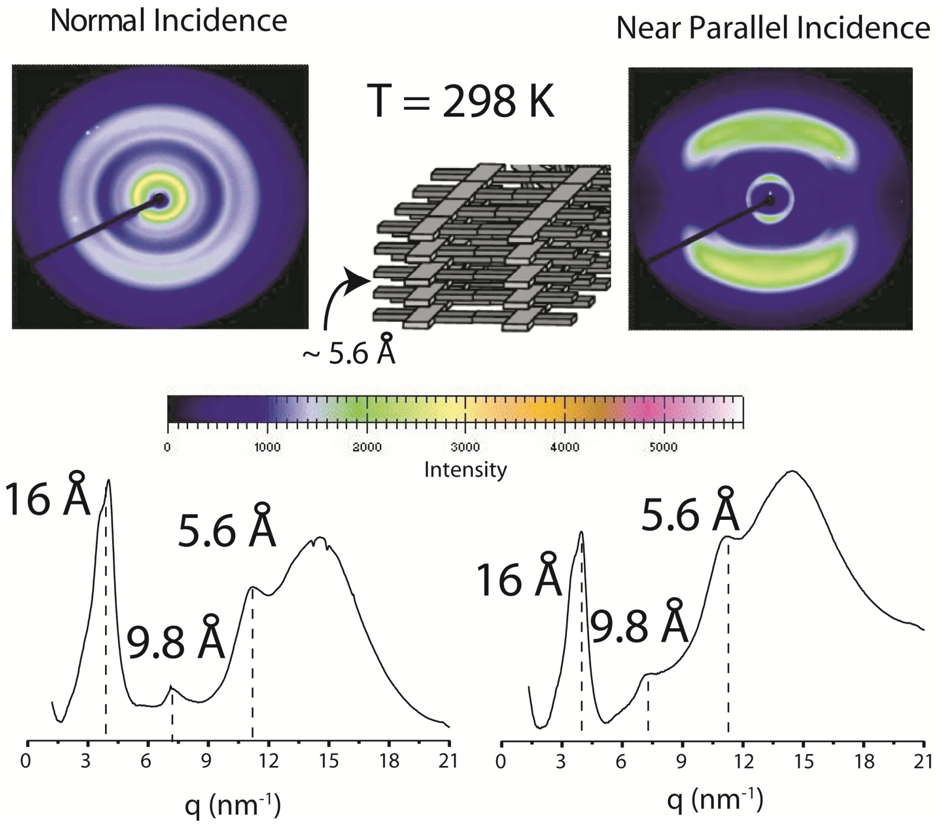

Figure 33 – Wide Angle X-Ray Diffraction (WAXD) results of F8BT films at 298 K for incidences, normal and parallel. Top: 2D images and, Botton: 1D pattern. The inset in the middle represents the lamellar β-phase.

WAXD measurements were also performed as a function of temperature, from 173 to 523 K, giving an important insight into the changes in the microstructure of the F8BT polymer. The results are shown in figure 34 for both incidences. The β-phase remains unchanged up to nearly 398 K, suggesting that it is highly stable as the temperature increases. However, at 398 K the profile starts to narrow and a collection of new sharp peaks start showing up, especially between 10 and 20 nm^{-1}. Note that 398 K is the region of the appearance of the glass transition, measured by the DSC method. This suggests that the collective movement of the backbone, which occurs during the T_g, is the onset of the dissipation of the β-phase, giving rise to a new crystalline phase.

This phase transition starts at around 400 K and continues up to 473 K. At 498 K a series of well-defined sharp peaks appears, indicating that the new phase has been entirely formed. Such new phase is known as the α-phase and it is commonly observed in several polyfluorenes and derivatives[103,104]. One may observe that such structural phase is highly ordered, being formed by the crystallization processes identified by thee DSC experiments at ≈ 475 K.

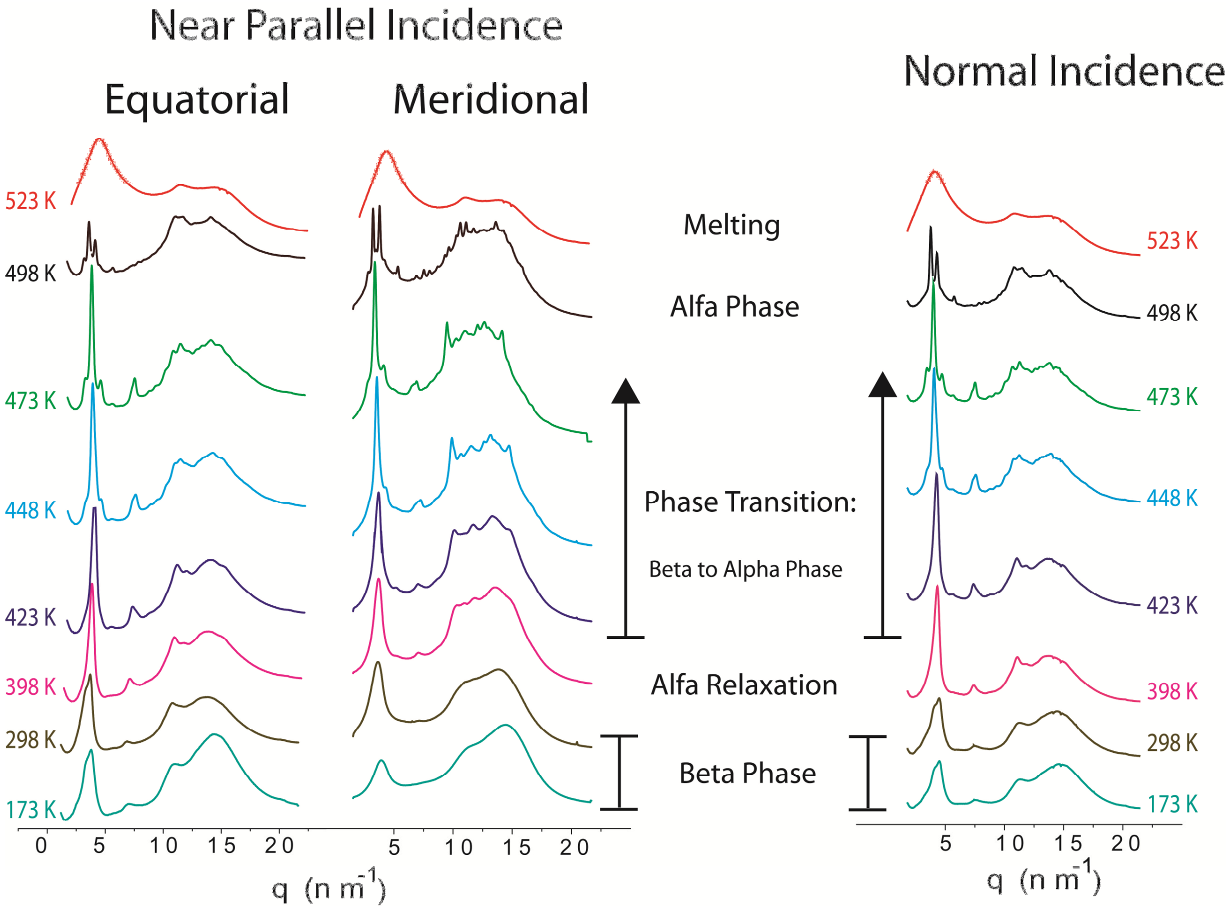

Figure 34 - WAXD measurements as a function of temperature and for both incidences normal (left) and parallel (right).

Subsequently, the crystalline α-phase is melted (1D pattern at 523 K), yielding a pattern typical of a nematic liquid crystalline phase. Such melting was also measured at about the same temperature registered by the DSC experiments (≈ 500 K).

Finally, one may observe that, even before the melting temperature, there is a background contribution (amorphous halo) in the F8BT diffractograms that resembles the pattern of the liquid crystalline phase after melting. It confirms the statement made in chapter 2 that there are no full crystalline polymers, but semi-crystalline ones, since the ordered crystalline part is normally embedded in a disordered amorphous background, as suggested by our WAXD experiments.

3.2 Molecular Dynamic Results: Dynamical Mechanical Thermal Analysis and Nuclear Magnetic Resonance

The DSC and WAXD measurements revealed a rich structural evolution of F8BT films. The crystallization of the α-phase, started exactly around the glass transition, indicates that relaxation and dynamical processes may play an important role in the transition between phases in polymeric systems. Hence, it is crucial to investigate the molecular relaxation more accurately. DMTA is an important tool to reveal polymer relaxations. In this sense, DMTA measurements were performed the using a tension mode Netzsch 242C instrument, with frequencies ranging from 0.01 to 100 Hz and a heating rate of 2 K/min from 100 to 400 K.

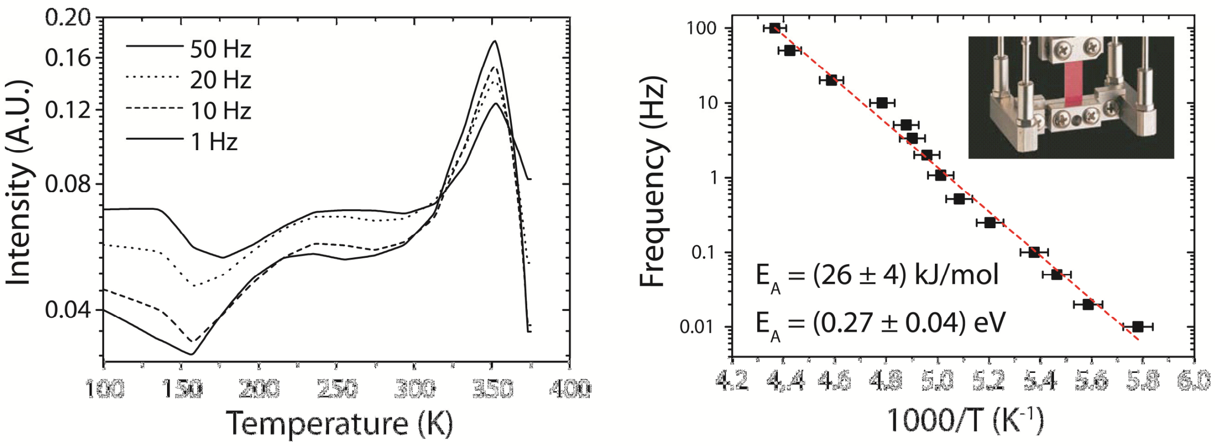

Figure 35 – DMTA results: (Left) tanδ versus temperature for several excitation frequencies and, (Right) the Arrhenius plot for the low-temperature β-relaxation.

Figure 35 (left) shows the temperature dependence of the tanδ for excitation frequencies ranging from 1 to 50 Hz. The lower temperature peak (β-relaxation), composed of a single broad peak for all excitation frequencies, was observed from 160 to 250 K. The higher temperature peak, at T = (360 ± 15) K, is undoubtedly assigned as the glass transition and it is consistent with that measured by DSC.

Figure 35 (right) shows the Arrhenius plot of the frequency at the maximum DMTA intensity for the peaks corresponding to the β-relaxation. The activation energy was calculated by fitting the frequency versus 1/T dependence of the tan δ according to the Arrhenius law:

$$f = f_o e^{-\frac{E_A}{RT}} \qquad (65)$$

where f is the frequency (Hz), f_o is the pre-exponential factor (Hz), E_A is the activation energy (J mol^{-1}), T is the absolute temperature at which the maximum of tan δ occurs for each relaxation process, and R is 8.32 J/Kmol. The calculated activation energy was $E_A = (26 \pm 4)$ kJ/mol. This value is typical of local motions of specific segments, as published before[38].

Unfortunately it was not possible to derive an Arrhenius plot for the glass transition, since, at T_g, F8BT films soften in such a way that they slip off the DMTA sample holder. Nonetheless, a recent article published by Faria and co-workers[38] showed an Arrhenius plot for the glass transition temperature measured by DMTA. It was shown that the obtained curve was clearly nonlinear, exhibiting a typical Vogel-Fulcher behavior (exponential decay), as expected for the glass-rubber transition[30,62].

As presented in chapter 2, another technique used to identify the onset of molecular relaxation in bulk samples is the ^1H NMR. The measurements respective were performed using a Varian Inova spectrometer at ^1H frequency of 400.0 MHz. A 7-mm Doty NMR static probe head with variable temperature (VT) was used. Typical $\pi/2$ pulses lengths of 4.5 µs were applied for the ^1H.

Figure 36 (left) shows the ^1H NMR spectra of F8BT for several temperatures (120 to 470 K). It is easy to notice that the NMR line shape narrows at increasing temperatures. As already discussed, this narrowing effect is due to the onset of molecular dynamic of specific molecular segments, resulting in a local averaging of the nuclear spin interactions, particularly the H-H dipolar coupling.

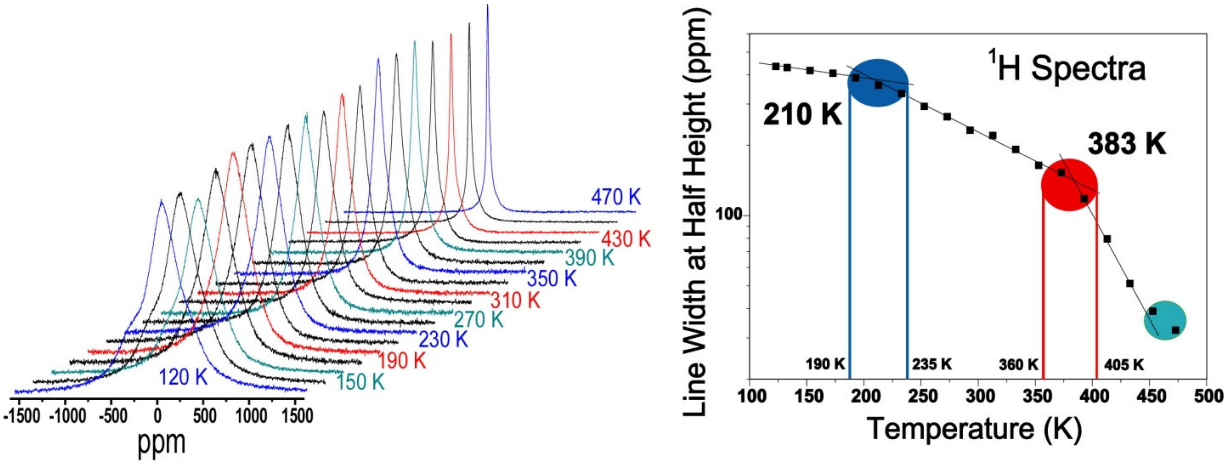

Figure 36 – ^{1}H NMR results: (Left) spectra for several temperatures. As the temperature increase the signals get narrower: and (Right) the line width versus temperature. Two transition regions is observed, which were attributed to the transition already measured by DSC and DMTA.

The ^{1}H NMR line widths at half-height are plotted against the temperature figure 36 (right). We can observed two transition regions, one at T = (210 ± 20) K and the other at T = (383 ± 20) K. Interestingly, the first transition corresponds to the β-relaxation measured by DMTA and the second to the glass transition measured by both DMTA and DSC.

It is worth mentioning that different techniques resulted in a similar conclusion. The ^{1}H NMR technique is rather local, compared to the DMTA or DSC. Even though, it has led to the same interpretation concerning the molecular relaxation. The question that arises is: what are the nature and the mechanism of such molecular transitions? To answer this question, we carried out High-resolution NMR measurements, which are reported below.

High-resolution solid-state NMR experiments were performed using the VARIAN INOVA spectrometer at ^{13}C and ^{1}H frequencies of 100.5 and 400.0 MHz, respectively. A VARIAN 7-mm MAS double-resonance probe head with variable temperature (VT) was used. The spinning speeds, varying between 4 and 10 kHz, were controlled by a VARIAN pneumatic system which ensures a rotation stability of ± 2 Hz. Typical $\pi/2$ pulses lengths of 3.5 and 4.5 μs were applied for ^{13}C and ^{1}H, respectively. Time Proportional Phase Modulated (TPPM) proton decoupling with field strength of 60 kHz, cross-polarization time of 1 ms and recycle delays varying between 3 and 5 s were used. Slow molecular motions were investigated using the Centerband-Only Detection of Exchange (CODEX) technique[78] with its constant time scheme (CONTRA)[80], and a mixing time t_m of 300 ms and maximum evolution times ($4Nt_r$) of 800 μs. The temperature dependence of C-H dipolar coupling was measured by the DIPSHIFT technique[75], in which H-H homonuclear decoupling was achieved by the Phase-Modulated-Lee-Goldburg (PMLG) sequence[65], using field strengths of approximately 60 kHz.

Figure 37 shows the CPMAS spectra for F8BT at two temperatures, together with the corresponding line assignments according to the carbon's numbering. Note that the side-chain (aliphatic group) is placed at the right side of the graph, from 60 to 0 ppm, while the backbone is found at higher ppm values on the left side (from 110 to 160 ppm). It is an expected result, since the electronic cloud is concentrated on the conjugated chain (backbone), shifting the carbon's magnetic resonance to high ppm due to the electronic shielding of the magnetic field. The assignments were achieved by comparison with the ^{13}C NMR spectra, of similar compounds found in the literature, for both liquid and solids.

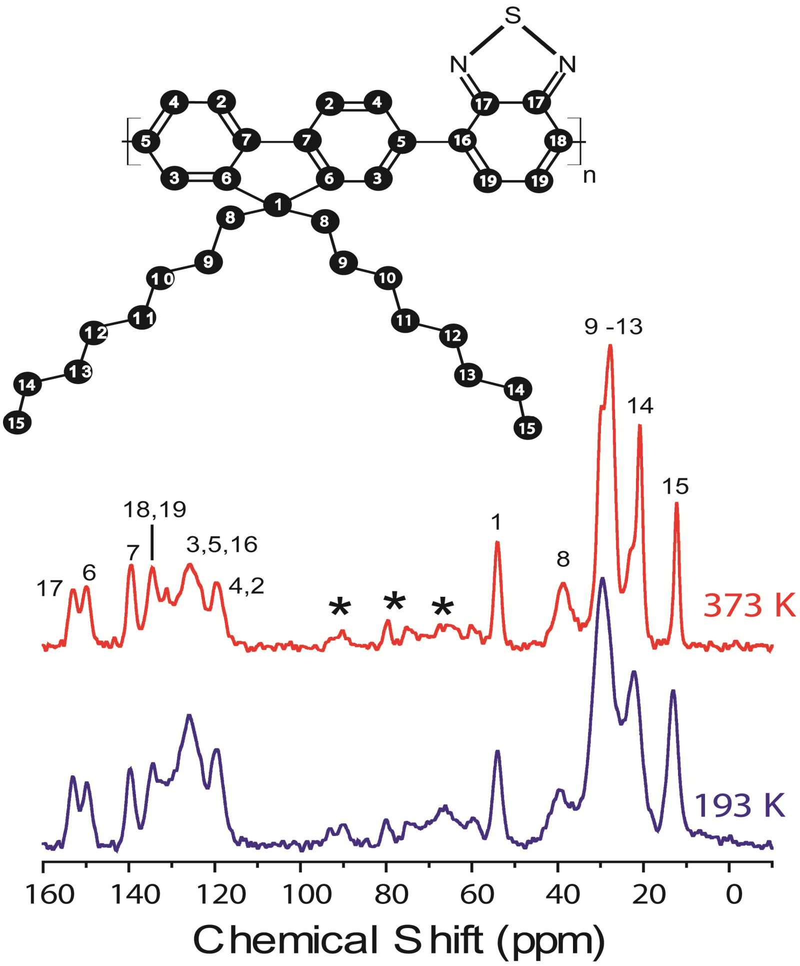

Figure 37 – CPMAS results for two temperatures (193 and 373 Kelvins) and the correspondent assignment of carbons and lines.

At higher temperature (373 K) the lines associated to the side-chain, mainly from 40 to 20 ppm, start narrowing, indicating that these molecular segments execute molecular rotations at rates high enough to partially average the ^{1}H-^{1}H dipolar interaction (dynamics at rates of few kHz).

No evidence of narrowing is observed for the backbone, though, suggesting that, even at 373 K, no or very slow dynamics (much less than kHz) dominate the molecular movement scenario for this segment.

Unfortunately, the CPMAS technique is not able to give more detailed information about molecular motions. For our purposes, the CPMAS is an important technique both to assign the carbons to the corresponding lines and to give some insight about the molecular rotations of the segments. More specific information concerning the molecular dynamics must be obtained from specific NMR methodologies developed to probe well defines regimes of dynamics. One of them is the DIPSHIFT technique presented below.

As discussed in chapter 2, the DIPSHIFT technique measures the CH magnetic dipolar coupling, which is sensible to molecular motions with rates between 10^3 and 10^7 Hz. The CPMAS measurements suggested that, due to the narrowing of the side-chain lines, such segments were executing molecular rotations at rates that might be sensible to DIPSHIFT.

Figure 38 shows the DIPSHIFT curves obtained at several temperatures for selected main-chain and side-chain carbons. The curves corresponding to the backbone (figure 38a) do not present any considerable change as a function of temperature, confirming the absence of dynamics on the backbone, as revealed by CPMAS. In contrast, the curves obtained from lines arising from carbons on the side-chain (figure 38 b and c) show a steady increase in the minimum of the smile-like DIPSHIFT curve as the temperature rises, suggesting the existence of molecular reorientation in the carbons in question, with dynamic rates sensible to the DIPSHIFT measurement.

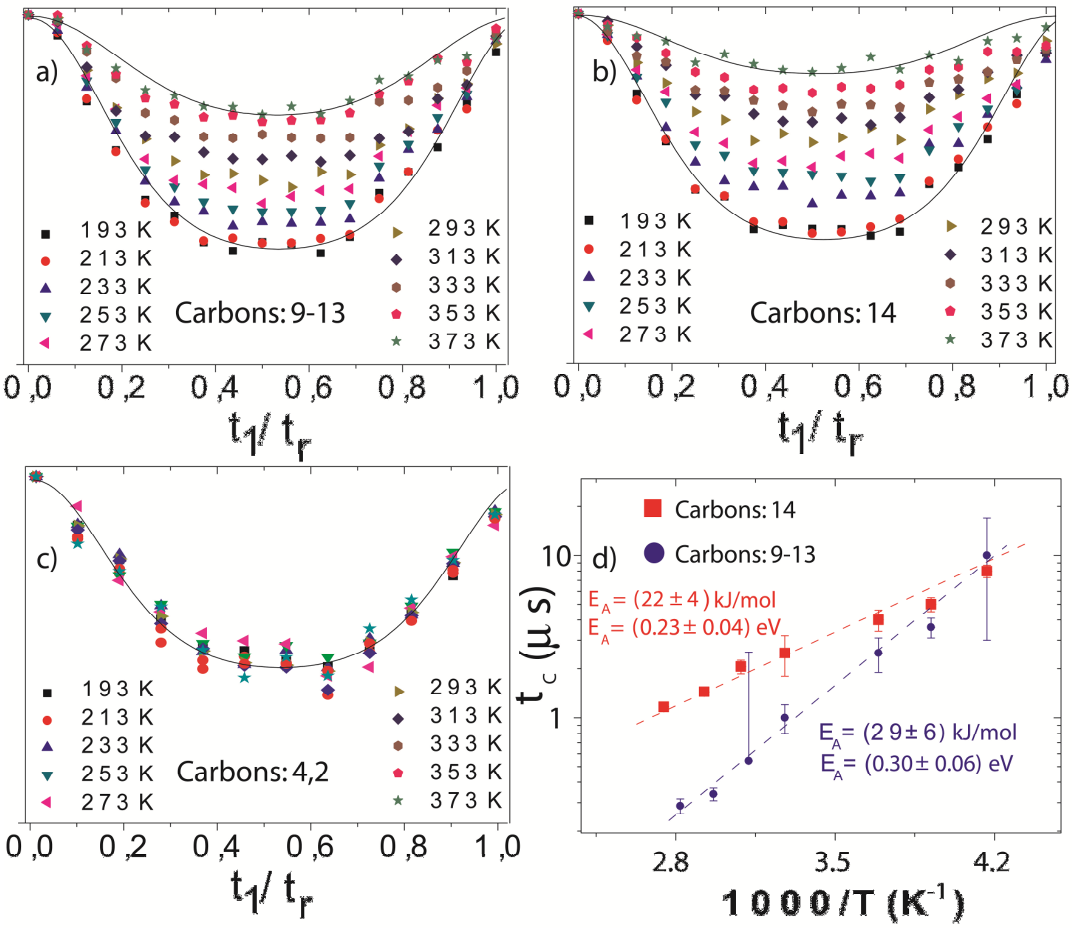

Figure 38 - DIPSHIFT curves obtained at several temperatures and from different carbons on the polymer chain: side chain (a and b) and main chain (c). The Arrhenius plot of the side chain carbons are presented at d.

From 193 to 213 K, the minimum of the DIPSHIFT curve remains almost constant, due to the lack of molecular dynamics on the side-chain. However, as the β-relaxation temperature is reached (≈ 210 K), such minimum of the DIPSHIFT curve starts to increase, because of the onset of molecular movements responsible for the β-relaxation. At increasing temperatures, there is a reciprocal increase in the minimum, suggesting that the motion rate is also constantly increasing.

Nevertheless, for carbons 9-13, the last two temperatures (353 and 373 K) produces almost identical DIPSHIFT curves. This feature implies that the fast limit motion regime (motional rates » dipolar coupling frequencies) has been achieved. Such a regime occurs when the DIPSHIFT curves have no dependence on the motional rates, being completely defined by the residual CH dipolar coupling.

The residual CH dipolar coupling arises as a result of the anisotropic rotation, which is not random enough to fully average the dipolar interaction. The intensity of the residual coupling is then an image of the motion geometries. Note that, on the high temperature DIPSHIFT curves for carbons 14, the fast limit regime has not been achieved. This is reasonable, as, at the end of the side-chain, the CH_2 are freer to move, compared to the ones in the middle of the side chain.

Another important characteristic of the molecular dynamics that can be extracted from the DIPSHIFT curves is the correlation time. To do so, we used the modeling treatment known as Anderson-Weiss approximation, which considers a Gaussian distribution of local dipolar fields and diffusive anisotropic motions, being the correlation time the single fitting parameter. The fitting is shown for the first and last curves in figure 38 ab.

Arrhenius plots of the correlation times were derived for the side-chain CH_2 segments and are illustrated, with the corresponding activation energies, in figure 38 d. Although the energies are slightly different for the distinct CH_2 segments on the side-chain, both are in agreement with the activation energies estimated from the DMTA measurements, confirming that these motions are indeed responsible for the β-relaxation process. It is worth mentioning that rather different techniques, with distinct approaches, such as the DMTA, led to similar results.

Despite the information about the side-chain and β-relaxation obtained by DIPSHIFT, no information concerning the backbone and, consequently, the glass transition relaxation arose. To investigate such process, we used the CONTRA NMR technique, to be discussed next.

As mentioned in chapter 2, the CONTRA technique detects the signal reduction due to changes in the orientation-dependent chemical shift frequencies, which take places during the mixing time. The quantification is made by the normalized intensity, $\Delta S = \left(\frac{S_0 - S}{S_0}\right)$, giving rise to a curve that is dependent of reorientation angle of slow molecular dynamics.

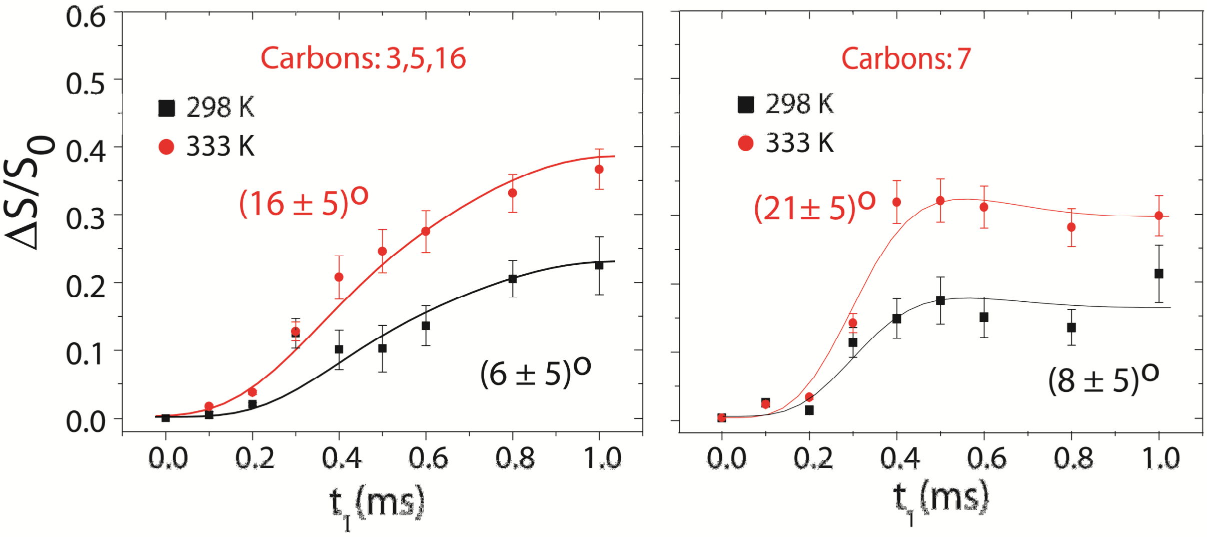

Figure 39 - CONTRA results of: a) carbons 3 and 5; b) carbon 7. It is possible to observe that the reorientation angle of the main chain increase with temperature.

The CONTRA experiments were performed at two temperatures, 298 and 333 K. Figure 39 shows the curves obtained corresponding to the carbons 3 and 5 (left) and 7 (right). The modeling of the CONTRA curves reveal average reorientation angles of (6 ± 5)° and (16 ± 5)° at 298 and 333 K respectively. Similar results were measured for other backbone carbons, suggesting a collective carbon libration throughout the fluorenyl and benzothiadiazole group.

Such increase in the reorientation angles is an indication that the glass transition temperature involves a substantial rise in the collective motion on the backbone, since this increase in the libration occurs close to the glass transition temperature.

4 Electrical Measurements

In this chapter we shall discuss the results of the electrical measurements obtained for both thick and thin film devices. Correlations with the results presented on chapter 3 will be outlined. Finally a correlation between the results obtained for thick and thin devices will be drawn.

4.1 Thick Film Devices

In this sub-chapter we present results obtained for devices built according to the procedures described in sub-chapter 2.5.5. The polymer layer was deposited by drop cast and its thickness was 4 µm, and therefore, we are sure to have used a similar morphology and structure as in the chapter 3 (structural/dynamical investigations). The idea behind this choice was to investigate thick samples, and, afterwards, we would extend the investigation to thin film devices, with characteristics similar to those used in industrial applications. All electrical measurements, for both thick and thin samples, were conducted using a close-cycled Helium cryostat with quartz optical-windows. The temperature control was made with the help of a Lakeshore 331 TC, allowing a temperature variation from 50 to 490 K.

4.1.1 Current versus Voltage (IxV)

The current-voltage characteristics of the thick F8BT devices were measured using a Keithley 6059A source-meter unit. The samples were kept under vacuum inside the closed-cycled Helium cryostat. Measurements were conducted in steps of 10 K with a 15-minutes wait for the sample to reach the thermal equilibrium. The current-voltage sweeps were performed in steps of 10 V, from 0 to 400 V.

The IxV characteristics at several temperatures are presented in figure 40a. For low temperature and low voltages, the current is rather small and constant up to a certain transition point ($V_T \approx 105$ V, for $T = 50$ K – see arrow in figure 38a), at which a strong increase in the current is observed with the applied voltage. The transition point is temperature-dependent and moves toward high voltages as the temperature increases.

These IxV characteristics are similar to that observed for the trap-filled regime, figure 25, chapter 2. The trap-filled limit, defined as the voltage, in which nearly all traps are filled, can be estimated by the following equation[86]:

$$V_{TFL} = \frac{qL^2}{2\varepsilon_0 \varepsilon_r} N_T \qquad (66)$$

where L is the film thickness and N_T is the total concentration of traps.

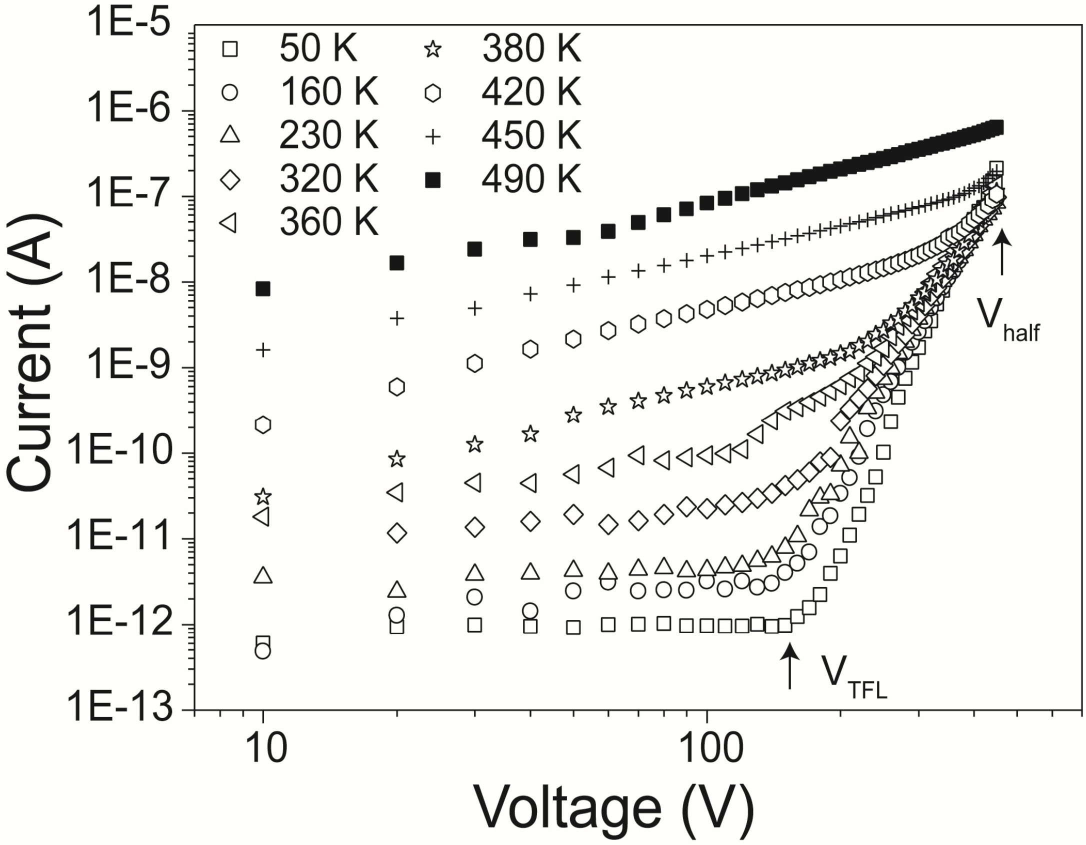

Figure 40 - IxV characteristics for selected temperatures for F8BT thick devices. Observe the presence of the trap-filled limit.

As one can see in figure 40, the V_{TFL} changes for higher voltages as the temperature increases. From the V_{TFL}, it is possible to estimate the total density of traps as a function of temperature. This is shown in figure 41. N_T is nearly constant and equal to 3.5x10^{24} m^{-3} from 50 to 350 K. Close to the glass transition (≈ 360 K), N_T starts to increase and reaches 9x10^{24} m^{-3} at 450K. Nevertheless, it should be expected that N_T did not change, unless the polymer underwent a phase transition.

From the WAXD, experiments it was possible to observe that at 398 K, the amount of β-phase in the sample starts to decrease, giving rise to the crystalline α-phase. The increase of N_T can be associated to this structural transformation, since the α-phase is less planar (probably helical[38]), and, consequently more structural traps are expected. Moreover, in figure 34, the ratio between the crystalline and the amorphous portion increases. It has already been mentioned that the interface between two different structural phases can act as a strong trap-region. Therefore both assumptions explain the origin of such increasing number of traps. Also, in the amorphous region, one expects to have an increasing charge detrapping, due to the coordinated movement on the polymer main-chain. With a larger detrapping rate, the system requires a large amount of charges in order to reach the trap-filled regime. Hence, the V_{TFL} moves toward high voltages and, as a result, N_T increase. It is worth mentioning that the values calculated for the total concentration of traps is reasonable when compared to that obtained by simulations[86] of similar polymers.

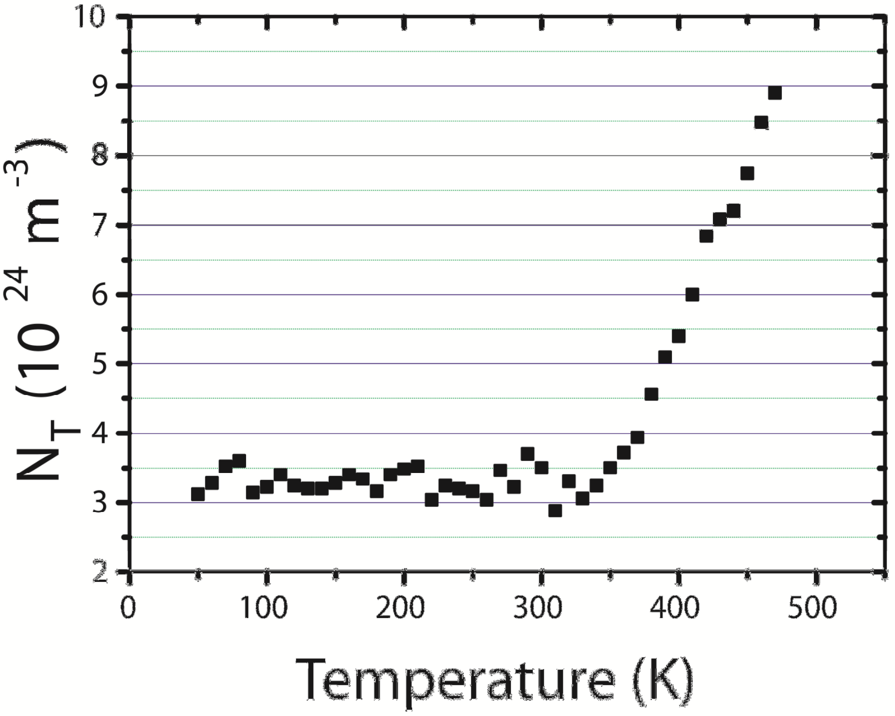

Figure 41 - Total density of traps calculated from the V_{TFL} point of experimental IxV curves of thick films devices.

Another interest feature of the IxV curves is that the current, at lower voltages, is also strongly temperature-dependent. From 50 to 490 K, the current at 10 V changed four orders of magnitude (from 10^{-12} to 10^{-8} A). However, except for the curve obtained at 490 K (above the crystalline transition), all IV curves seem to cross the same point at 400 V (E = 100 MV/m). This feature suggests that we might have a special point on IxV curves that is not temperature dependent.

An interesting paper has been recently published[86], in which a new Gaussian trap distribution model is used to describe IxV characteristics. This model assumes that the occupancy of traps is given by the product of a trap Gaussian Density of States (DOS) and a Fermi-Dirac distribution. The IxV curves simulated using this theory presented the same characteristic as crossing IxV curves at the same bias. The authors suggested that, at this bias point, the Fermi level passes through the middle of the Gaussian trap distribution, and exactly half of the traps are occupied, regardless of the width of the Gaussian distribution. This voltage can be calculated as:

$$V_{half} = \frac{qL^2}{4\varepsilon_0\varepsilon_r}(N_T - n_{t0}) \qquad (67)$$

where n_{t0} is the density of charge trapped in the absence of applied voltage. Hence, as we know N_T, calculated by V_{TFL}, and the crossing voltage, we can estimate n_{t0}.

The IxV curves for thick films were not modeled by the modified SCLC theory presented in chapter 2, since below V_{TFL} it was not possible to observe a clear transition between the Ohmic and the trap-filled SCLC regimes (as suggested in figure 25, chapter 2). The reason for this might be explained by the complexity of the structure and morphology of thick films, as revealed by WAXD. Also, the extreme low current below V_{TFL} (10^{-12} to 10^{-9} A), indicates that the injection processes are limiting the IxV characteristics, and therefore, the SCLC model is not valid.

The principles of the current-voltage characteristics are basically addressed by equation 50. We based our discussion, up to now, on the density of charges and density of trapped charge. Nonetheless, we did not measured or mentioned the charge-carrier mobility (μ), which plays an important role in the conduction of polymer systems. Hence, in order to study the mobility at several temperatures, in the following sub-chapter we present mobility measurements using the Time of Flight Technique.

4.1.2 Time of Flight Technique (TOF)

The TOF technique was set using a 9-ns pulsed and tunable ND:YAG LPS-1500 Solar Laser (excitations from 335 to 900 nm). A Keithley 6517A was used as a DC-voltage source. The photocurrents were amplified by a FEMTO DHPCA-100 and recorded using a Tektronix TDS-5052 oscilloscope. In order to increase the signal-to-noise ratio, we averaged at least 64 transients. The laser was tuned to $\lambda = 470$ nm corresponding to the F8BT absorption, as in figure 42 (top).

TOF transients of positive and negative carriers were first measured to evaluate the majority and minority carriers. In figure 42 (bottom), it is shown the transient for both types of carriers, electrons and holes, at room temperature and with an electric field of ± 0.7 MV/cm. The electron transient is considerably stronger than the holes signal. It was not possible to measure the transit time of holes for F8BT thick films, indicating they are heavily trapped near to the interface at which they are photogenerated. On the other hand, the transit time for electrons was easily obtained using a double-log curve (see inset in figure 43-top). Our results are in complete agreement with those published by Campbell and co-workers[96]. Based on these first results, the subsequent TOF measurement were set to probe electron signals.

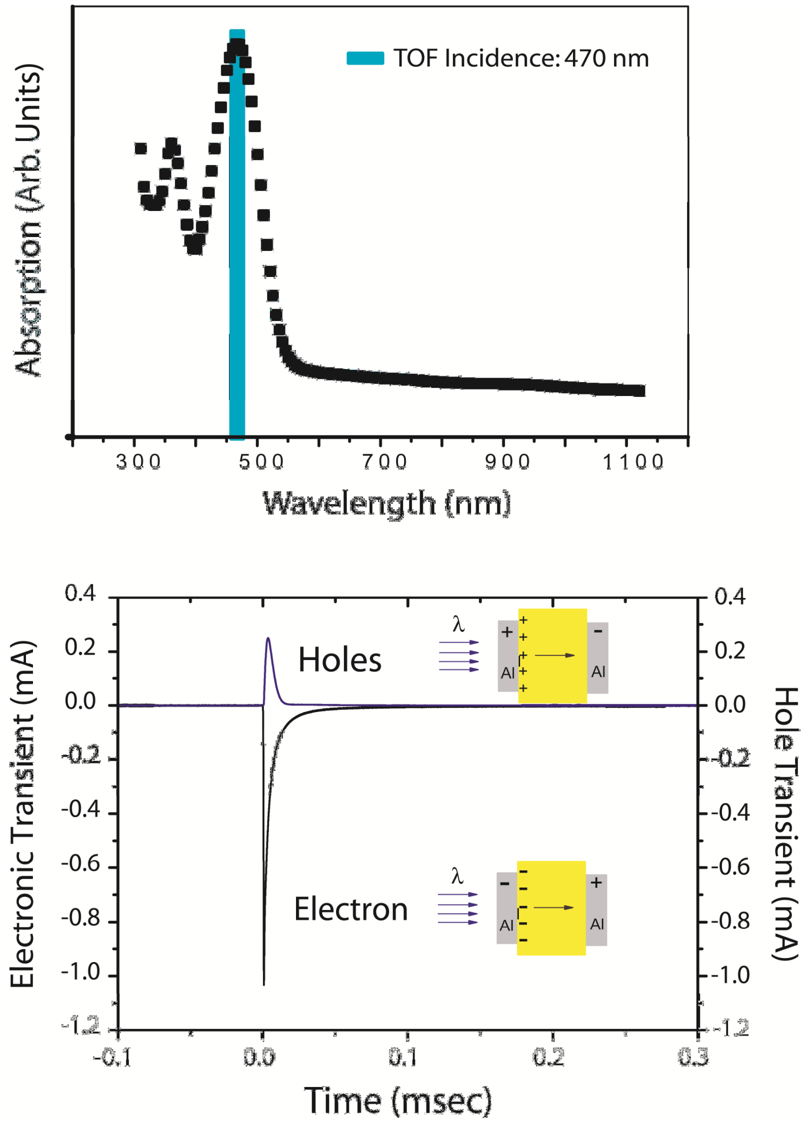

Figure 42 – **Top: Absorption Spectrum for F8BT: The laser incidence wavelength was choose at the maximum of absorption (470 nm). Botton: Comparison between electrons and holes TOF transient: Observe that electron transient is stronge than that of holes.**

Figure 43 (top) shows a typical current mode TOF transient for electrons at T = 340 K. The transient exhibits a continuously decreasing signal, without a clear plateau, indicating a rather dispersive charge transport. Hence, the transit time was extracted from the experimental curves in a double-log representation, as illustrated by the inset of figure 43 (top).

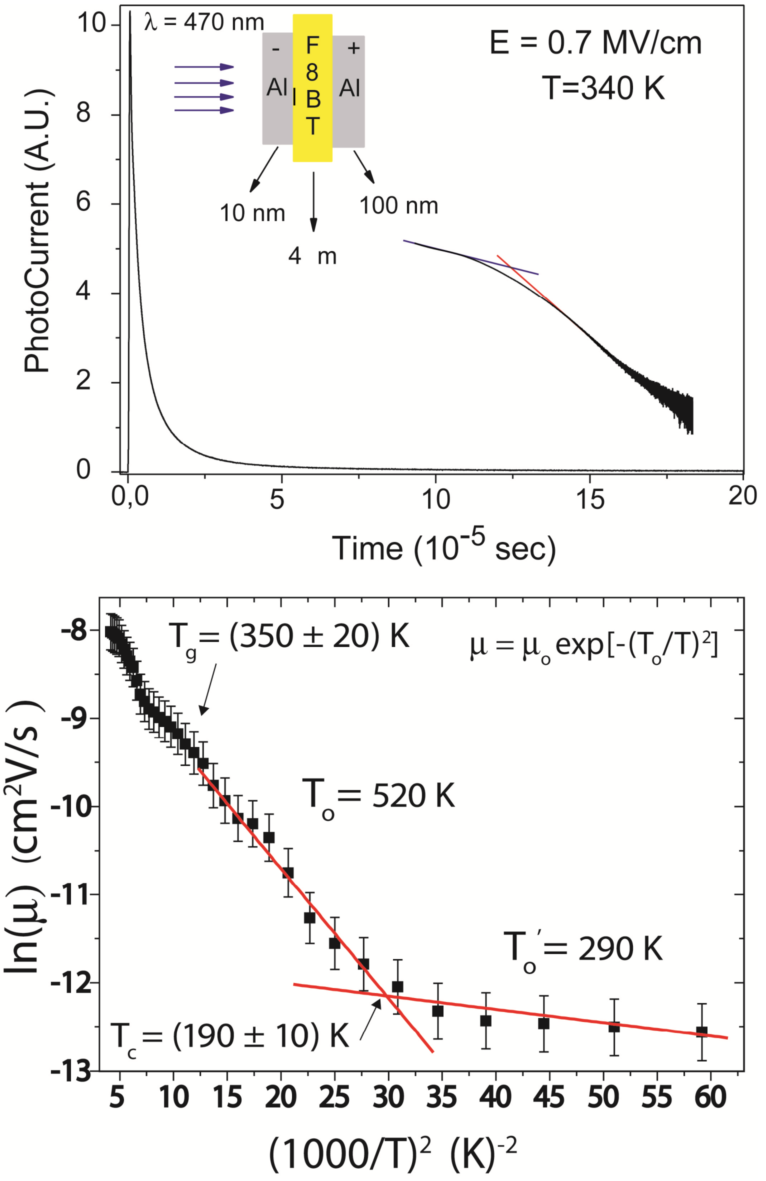

Figure 43 – Top: Typical current mode TOF transient for electrons at T = 340 K; the inset we have the same curve in a log-log representation. Bottom: the calculated mobility for each measured temperature.

The mobility was calculated for each measured temperature using equation 61. Figure 43 (bottom) shows the mobility values in the temperature range of 120 to 490 K, displayed on a $\ln(\mu)\, vs\, T^{-2}$ curve. This curve reveals two characteristic features: a clear change in the slope at 190 K and a deviation from a straight line at around 350 K. The results presented in chapter 3 revealed two molecular transitions, at approximately 210 K (β - relaxation) and 370 K (glass transition). The coincidence between the characteristic features of the $\ln(\mu)\, vs\, T^{-2}$ curve and the relaxation phenomena is remarkable.

Both linear regimes, above and below 190 K (T_c in Figure 43 bottom), were fitted by equations 62a and b, and the calculated ratio between the two slopes was (1.7 ± 0.3), which is in fair agreement with the ratio of the slopes predicted by the GDM model for a ND-D transition[21,87]. Since the GDM model correlates T_c with the ND-D transition, the charge transport across thick F8BT film of is non-dispersive above and dispersive below T_c. However, even above T_c the TOF transient signal did not present the typical plateau that characterizes the non-dispersive signals. It suggests that, in systems with high disorder structure and complex morphology, such as F8BT thick films, the transition from N-ND might not be due to geometrical or temporal reasons. It can also depend on changes in molecular reorientations and dynamics.

In this sense, the coincidence between the β-relaxation peak and the change in slope of the $\ln(\mu)\, vs\, T^{-2}$ also deserves discussion. The β relaxation is related to the onset of molecular motions on the side groups at about 210 K. Thus, the change in dispersiveness of the charge transport is also likely to correspond to a change in the structural disorder or fluctuation of the local conjugation length[97], which occurs due to the change in the local packing induced by the molecular agitation above the β-transition temperature.[38]

Another point to be discussed is the connection between the deviation from the straight line starting at 315 K and the occurrence of the glass transition. The faster increase in mobility above T_g ($T > 1.2\ T_g$) can be attributed to a motional narrowing effect that occurs as a results of the narrowing of the DOS induced by the glass transition. In this situation, the carrier experience, on average, a smoother energy landscape during their motion, and the slope of the $\ln(\mu)\ vs\ T^{-2}$ curve is increased above $1.2T_g$. At temperatures around T_g, the time scale of the collective molecular reorientations seems not to be fast enough for the carrier to experience the narrowed DOS, nor too slow so that the disorder could be considered static.

In other words, slightly above T_g, one may consider that the energy disorder becomes temperature-dependent, so a deviation from the GDM predicted behavior is observed. This is consistent with the non-linear behavior observed during the glass transition[87]. This interpretation was proposed in reference 87, in which a very similar behavior was observed for mobility measurements of vapor-deposited films of 1-phenyl-3-diethylamino-styryl-5-p-diethylphenylpyrazoline (DEASP) also carried out using the TOF technique. An equivalent view was proposed by Giro et. al.,[98] who suggested that, below T_g, there will be a strong localization of charges due to the geometrical restrictions, which does not favor hopping between neighboring sites, but rather trapping and detrapping. Following this idea, one might conclude that below the glass transition temperature, the conduction is trap-controlled and, at such temperature and above, the trapped charge carriers are liberated by the backbone molecular motion. This implies that a structural detrapping mechanism dominates the charge conduction around and above T_g.

Interestingly, the IxV results, especially in the V_{TFL} discussion, are also consistent with as increase in detrapping as the temperature reaches the glass transition.

Besides, the interesting correlation developed up to now, another interesting molecular-relaxation sensible measurement is the Impedance Spectroscopy. The next sub-chapter is dedicated to such technique.

4.1.3 Impedance Spectroscopy (AC)

AC measurements were performed on the thick samples described in sub-chapter 2.6. The curves were measured at different temperatures in the 70 – 490 K range and with frequencies varying from 10^{-1} to 10^{6} Hz. An Impedance Analyzer Solartron SI 1260 connected to a Dielectric Interface Solartron SI 1296 was used in all measurements.

In Figure 44 (top), some representative measured curves are shown in a Cole-Cole diagram (real impedance versus imaginary impedance). Characteristic semi-circles were obtained, revealing a decrease in both real and imaginary impedance as the temperature increases. It is worth mentioning that from, 450 K, a deviation from the natural semi-circle path is observed. This feature is normally attributed to a change in mechanism concerning the electrical properties of F8BT films. Curiously, at the same temperature, we measured, by DSC and WAXD, the F8BT crystallization: the dissipation of the β-phase and the formation of the crystalline α-phase.

Figure 44 (bottom) presents the real impedance versus temperature for frequencies ranging from 0.1 to 1.77 Hz (low frequencies). It is possible to observe three peaks, at 150, 350 and 450 K, on the real impedance curve. These peaks can be correlated with the molecular processes already analyzed by the techniques presented in chapter 3: the low temperature peak is due to the relaxation of the side-chain (β-relaxation), while the peaks at 350 and 450 K are associated to the glass and to the crystal-to-crystal phase transformation, respectively. By comparison, one might observe that the temperatures are similar to those obtained in chapter 3.

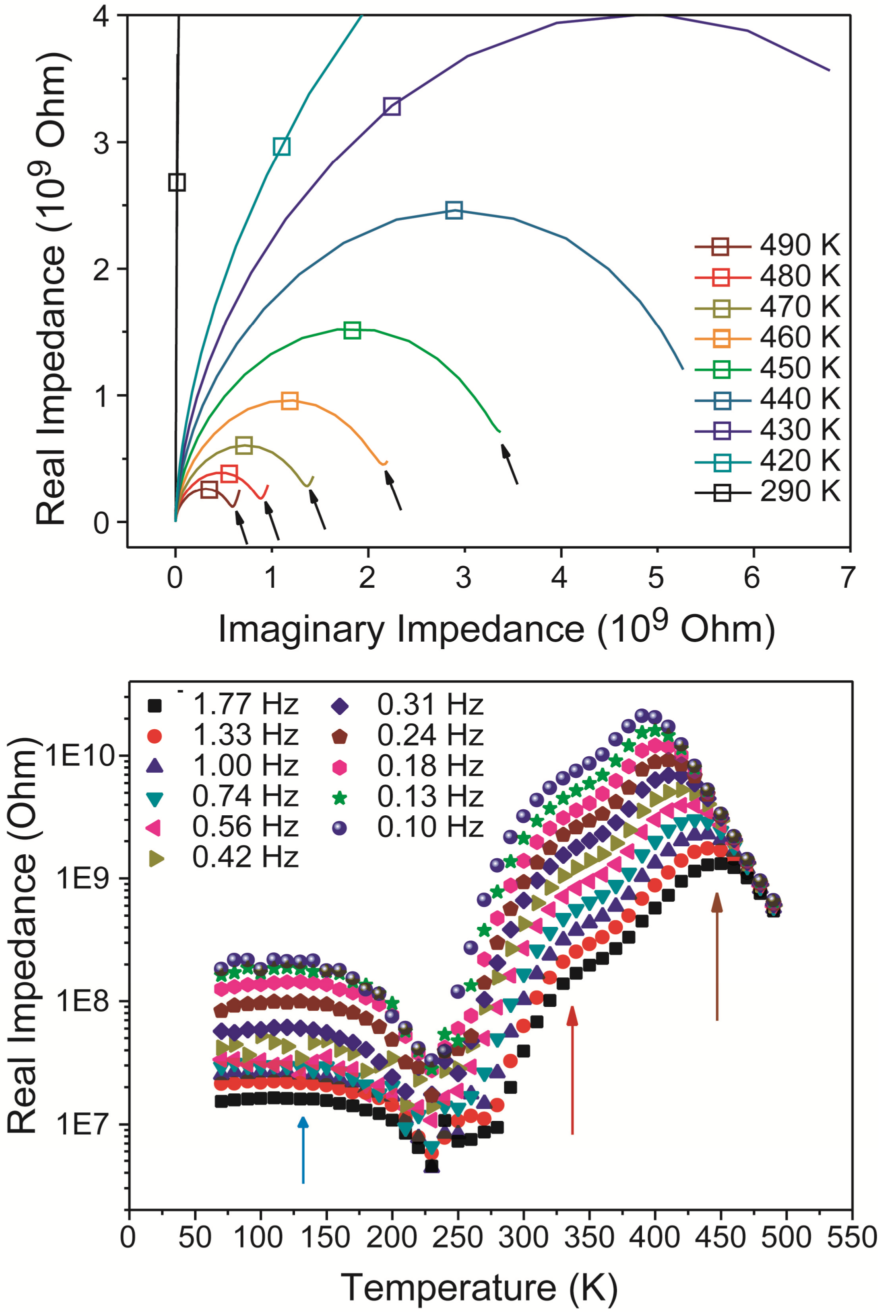

Figure 44 – Top: Cole-Cole diagram for selected temperature are presented and Botton: The Real Impedance versus temperature for selected frequencies are illustrated.

The first maxima observed at higher temperatures can be, indeed, attributed to the glass transition of the backbone, since, as measured by the CONTRA NMR method, in this range of temperatures, the main-chain is executing libration, with frequencies around unities of Hz, the same range we plotted on the real impedance versus temperature graph.

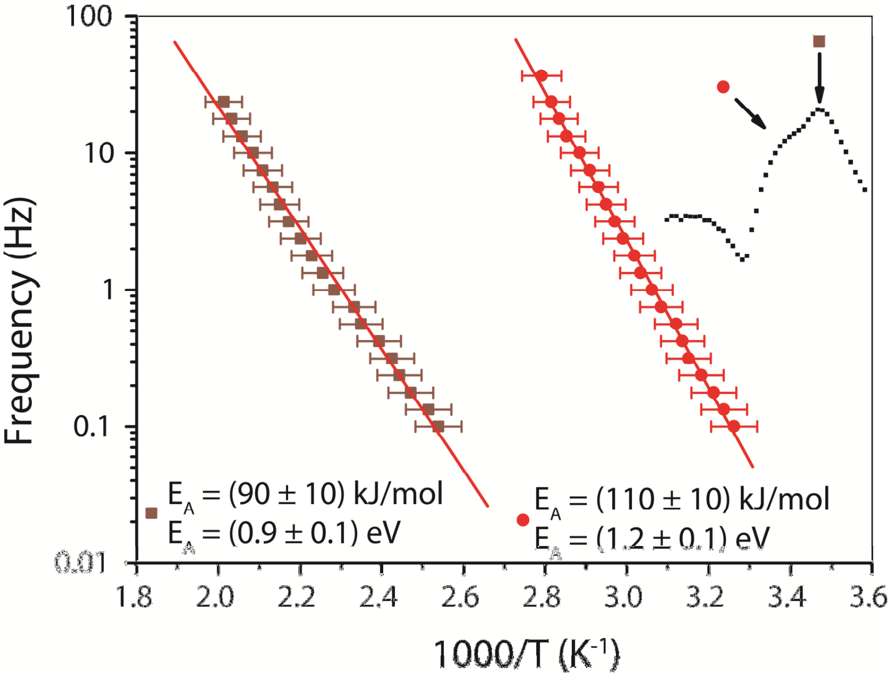

Figure 45 – Arrhenius Plot for the two high-temperature peaks observed in the real impedance versus temperature curves, as signed by the inset.

Another feature that can be analyzed is the Arrhenius plot of the two peaks at higher temperatures. It is well-known that conjugated backbone movements require an energy activation of hundreds of kJ/mol (units of electron-volts). Figure 45 shows the Arrhenius plot for both high-temperature peaks. The first (red) has an energy activation of approximately 110 kJ/mol (1.2 eV). Such high energy is expected for the glass transition, as it involves collective motions throughout the main-chain. The second, associated to crystallization, has an activation energy of 90 kJ/mol (0.9 eV), which is also plausible for this phenomenon.

4.2 Thin Films Devices

The F8BT devices thickness measured in the next sections is 250 nm. The devices were built as described in sub-chapter 2.5.5. Although the techniques used for molecular characterization presented in chapter 3 require thick films, normally obtained by casting deposition, on the following pages we will use the structural/dynamical characterization results obtained for micrometer films to explain the phenomena of electrical conduction and transport of nanometric thin films. The justification for that will be based on the Impedance measurements, which also showed the presence of the β-relaxation and the glass transition in the thin film devices. This is the reason we start with the Impedance measurement results in this section. It is worth mentioning that thin films, with thicknesses of hundreds of nanometers, are applied on realistic samples, such as, photovoltaic, light-emitting diodes and field effect transistors.

4.2.1 Impedance Spectroscopy

The DMTA, NMR, WAXD and, possibly, DSC are not methods designed to measure nanometric films, since it is essential to have free-standing films and, normally an amount of hundreds of mg of samples. These requirements are typically complicated to obtain with nanometric films. However, as showed from the Impedance Spectroscopy of thick samples (section 4.1.3), it is possible to probe the molecular relaxation in thin film devices using such measurement. Therefore, we have performed similar measurement and procedures as is section

4.1.4, using, however, a 250 nm film, in order to study the molecular relaxation in thin film devices.

Figure 46 (top) presents the real impedance versus temperature for frequencies ranging from 0.1 to 3.16 Hz (low frequencies). Differently from the results obtained for thick film, it was possible to observe only two peaks on the real impedance curve: the first at low temperature (≈ 250 K) and the second at around 425 K. Recent results[101], have shown that spin-coating films normally have less tendency to crystallization if compared to as-casting films. Therefore, our AC results indicate that, for thin films, the crystal-to-crystal transition does not occur, being the two peaks, respectively related to the side-chain relaxation (β-relaxation) and to the glass transition. By comparison, one might observe that the temperatures are shifted toward higher temperatures than those obtained in chapter 3. However, it is expected that thin films undergo molecular relaxation at higher temperatures because of the higher spatial restriction of these films[101].

In order to confirm the correspondence between peaks and molecular dynamics, Arrhenius plots were derived for both peaks. Figure 50 (bottom), shows the Arrhenius behavior for the low-temperature peak. The activation energy was found to be approximately 21 kJ/mol (0.21 eV), which is consistent with the results obtained for DMTA, DIPSHIFT and AC for thick films. Therefore, one can, undoubtedly, attribute such peak to the onset of molecular dynamics of the side-chain groups.

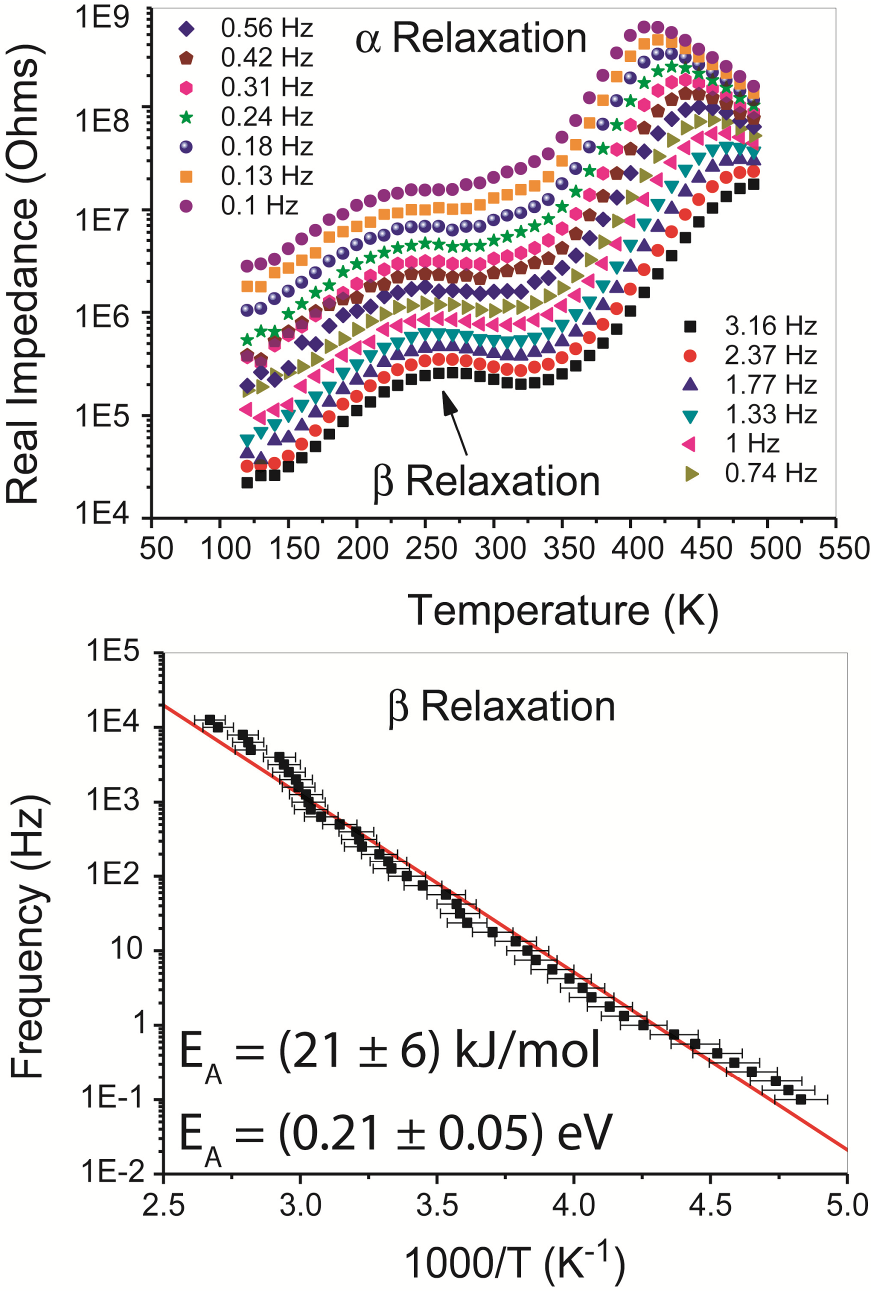

Figure 46 – Top) Real Impedance versus temperature for the frequencies range of 0.1 to 3.16 Hz and; botton) Arrhenius plot for the β-relaxation process.

Arrhenius plots were also made for the high temperature peak, as shown in figure 47. Despite the narrow frequency range appearance of such peak, it was possible to calculate, with accuracy, its apparent energy activation. The value obtained was approximately 70 kJ/mol (0.7 eV), which is lower than that calculated for the glass transition of thick films. T_g in thin films is expected to be found at higher temperatures[30,62]. It is well-known that the glass transition has a WLF behavior[30,38,62], which dictates that, at temperatures below 0.8 T_g, the Arrhenius curve is linear, and the slope of the curve can be interpreted as an apparent activation energy. Around the glass transition, the slope of the curve starts to increase achieving very high values ($\approx$ 200 kJ/mol at $1.2Tg$). If the temperature range of the measurement is restricted, a linear behavior is observed, but, in this case, the slope would depend on how far below T_g the experiment is conducted. Hence, the T_g for thin film samples occurs at a higher temperature, and the apparent activation energy measured for a similar temperature and frequency range is expected to be lower. This is schematically shown in the inset of Figure 45.

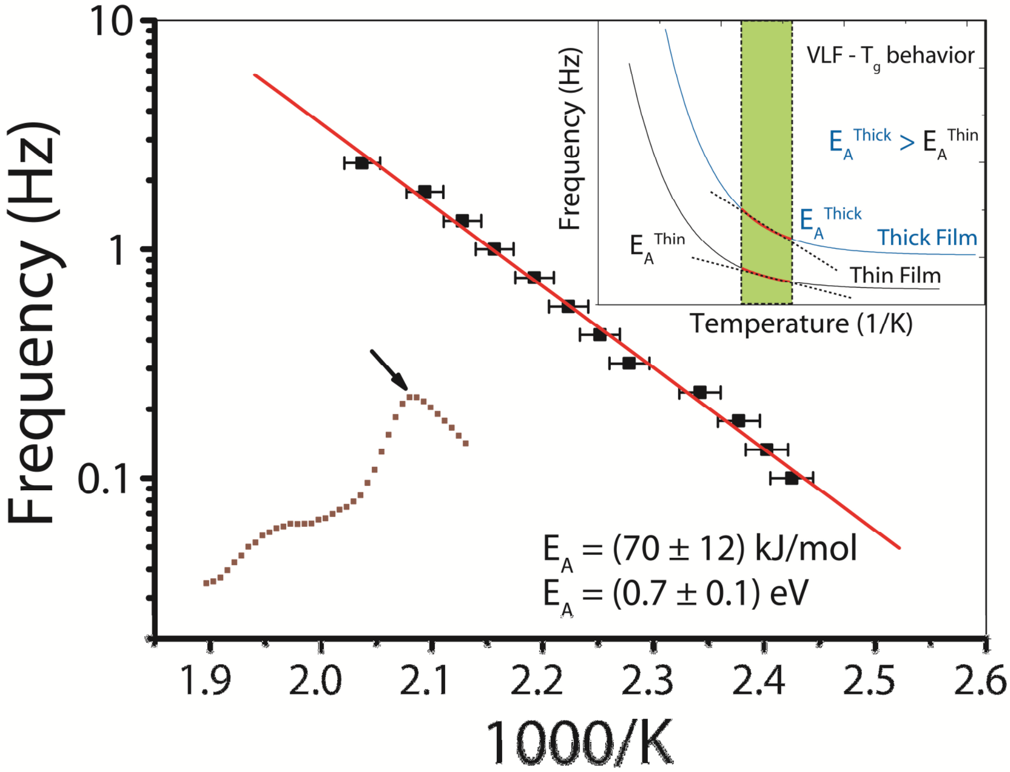

Figure 47 - Arrhenius Plot for the two high-temperature peaks observed in the real impedance versus temperature curves, as signed by the inset.

Finally, from the impedance spectroscopy measurements in thin films, we were able to confirm that both the β-relaxation and the glass transition also occur in such layers, and that the temperature of appearance is slightly increased. The AC results also revealed the absence of the crystal-to-crystal transition, suggesting that thin films are probably not as semicrystalline as the thick film is. Besides, the charge-carrier mobility results for thick samples revealed that those molecular dynamics phenomena affect the electrical properties considerably. The question which arises is: Shall the electrical properties of thin films be affected by the molecular relaxation processes measured by IS as it was for thick one? The next two sections are intended to answer this question.

4.2.2 Current versus Voltage (IxV)

The measurements were conducted with the same equipment and procedures as for thick films, although the external applied voltage range was reduced to 0 - 30 V.

In figure 48, the experimental IxV curves for the F8BT thin film devices are plotted for the whole temperature range (50 to 420 K) in a linear scale. One shall observe that the current, for higher voltages, increases from 50 up to 340 K. From this point, the IxV characteristics change their behavior and the current start decrease from 360 down to 420 K.

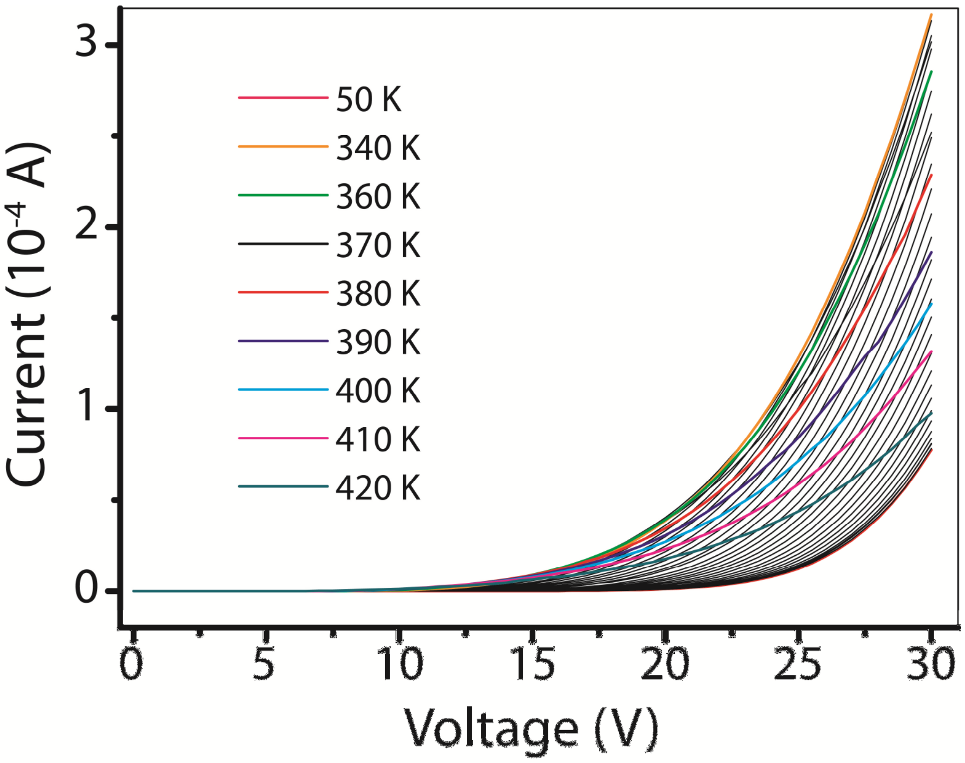

Figure 48 - Experimental Current-Voltage characteristics for F8BT thin-film device for several temperatures.

A more specific analysis can be made on a log-log plot of the IxV as shown in figure 49. In general, the curves exhibit a behavior similar to the one observed in figure 25 of chapter 2, with the presence of an ohmic region for low electric fields followed by a trap-limited Space Charge Limited (SCLC) region at higher voltages. Contrary to the case of thick films, V_{TFL} was not achieved, but changes were clearly observed in the behavior of the SCLC regions. Thus, the current-voltage data were fitted using the modified SCLC model with a stretched exponential-field dependence of the mobility, which was successfully used to describe many polymeric systems, although it fails to fit lower voltages currents[82-84]. Hence, we avoided such region, in order to minimize the fitting deviation. The calculation of such model was introduced in chapter 2.

Figure 49 shows the fittings of curves measured at different temperatures. The fitting regions were selected right above the kink observed on log-log scale in order to guarantee the validity region of equation 56. Such kink moves towards lower voltages as the temperature increases. For lower voltages and temperatures, the injection processes, due to thermal emission and the tunneling effect, are rather poor. Therefore, the bulk conduction is limited by the injection phenomena. As the temperature and the voltage increases, the injection of charges by the contacts increases, and a transition from the limited injection conduction to the space charge limited current occurs. Moreover, it is widely-known that, at low currents and low temperatures the diffusion currents are of greater significance to explain the IxV characteristics. However, the simplified model described in sub-chapter 2.5.1 ignores the diffusion. Consequently, we used equation 56 to fit the SCLC region of the experimental data in order to extract the zero field mobility (μ_0), as shown in figure 50.

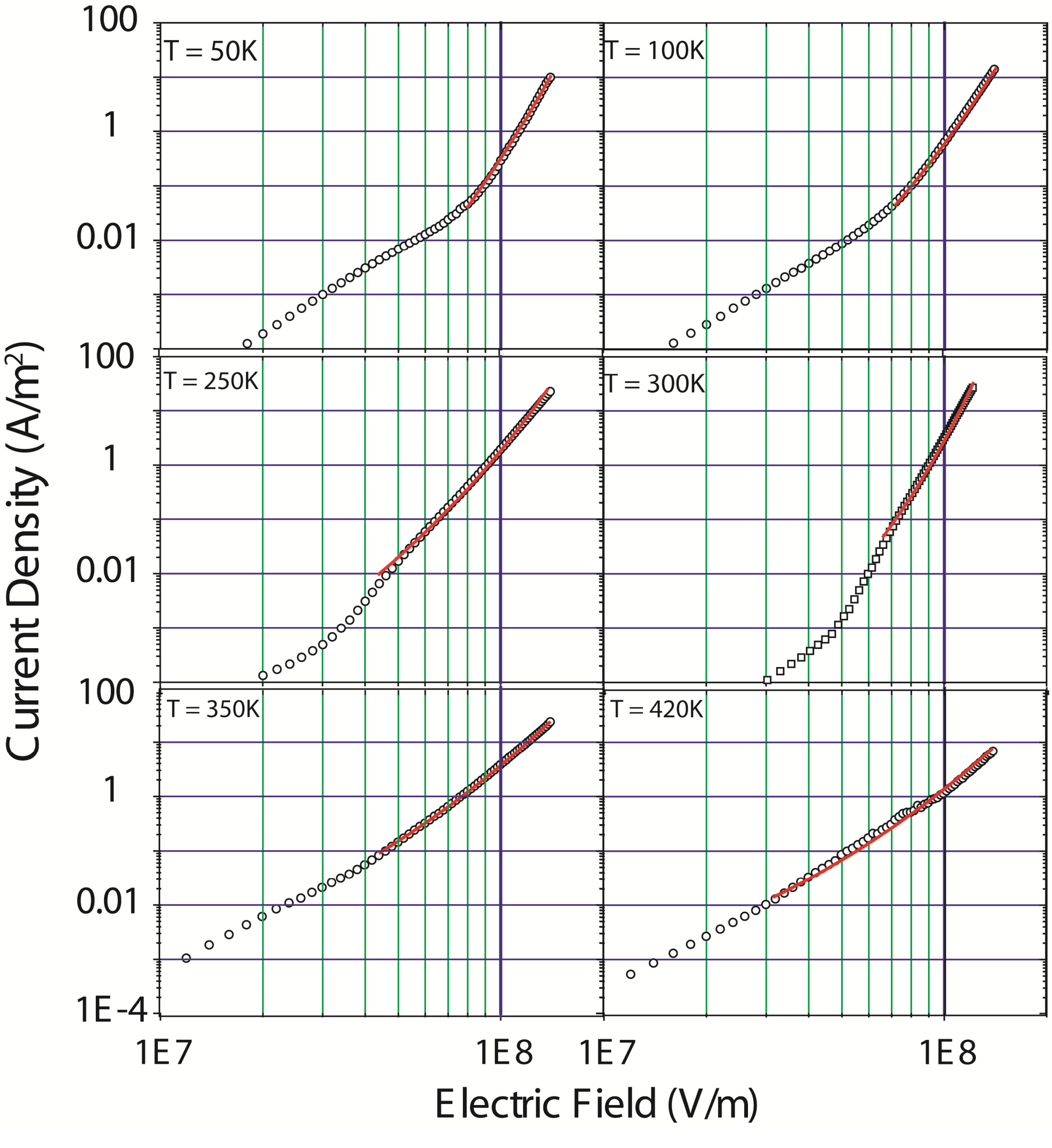

Figure 49 – Current-Voltage fitting using the model described at chapter 2. The fitting were made on the SCLC regime for different temperatures.

The variation of the extracted μ_0 values as a function of temperature is shown in figure 50. There, we plotted $\ln(\mu_0)\, vs\, T^{-2}$ in order to analyze μ_0 in the framework of the GDM model, as we did for TOF measurements of thick films.

Interestingly, the same behavior for μ_0 was observed in thick films TOF results: the shape of the $\ln(\mu_0)\, vs\, T^{-2}$ is rather similar to that of $\ln(\mu)\, vs\, T^{-2}$ measured for thick films. This curve reveals the two characteristic features: a clear change in the slope at 205 K and a deviation from a straight line at around 350 K. Such result also coincides with the molecular relaxation phenomena measured by techniques presented in chapter 3.

This suggest that the two molecular transitions, described in chapter 3, for thick films, and by Impedance Spectroscopy in the previous section, at approximately 210 K (β - relaxation) and 370 K (glass transition), seem also to be found in thin films and, moreover, interfere in the electrical properties of the nanometric polymer layer.

The linear regions above and below the break at T_c where fitted by equations 62 in order to calculate T_0. The calculated ratio between the two slopes was (1.8 ± 0.3), which can be considered to be in good agreement with the ratio of the slopes predicted by GDM (1.4) for a ND-D transition, since the present results were obtained by the simplified IxV model. Moreover, the shape of the $\ln(\mu_0)\, vs\, T^{-2}$ is fairly similar to that of TOF, which suggests that we might be dealing with similar influences on the transport phenomena.

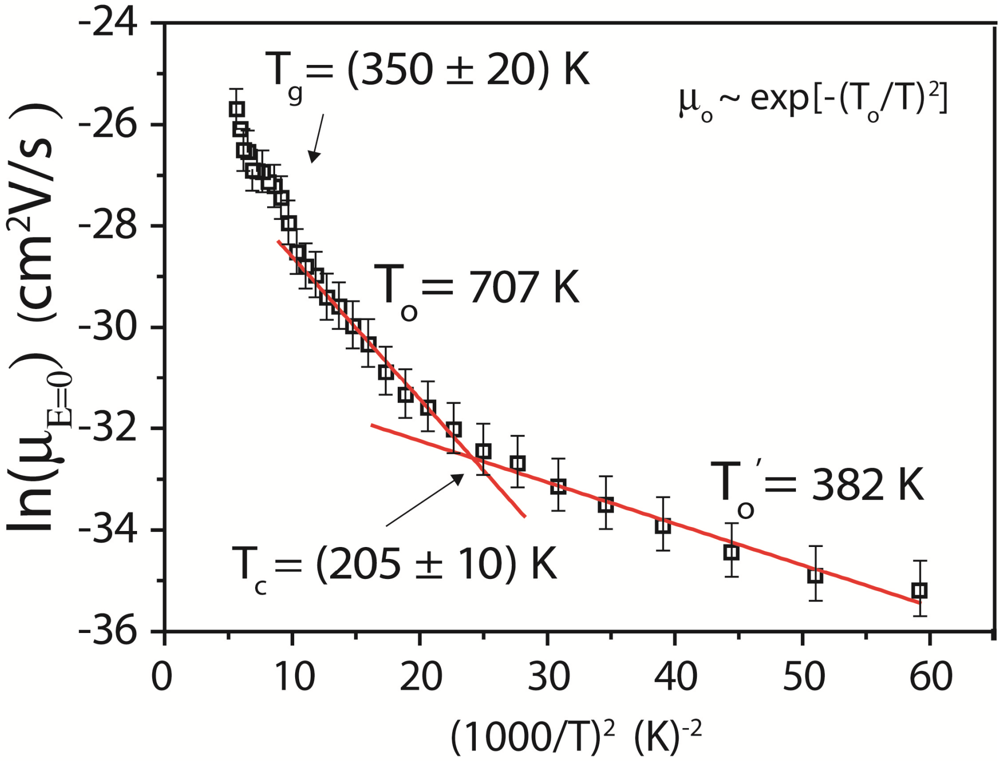

Figure 50 - Calculated mobility at zero-field for each measured temperature in a $\ln(\mu_0)\ vs\ T^{-2}$ graph, studied by the GDM model.

The mobility presented in this sub-chapter was indirectly calculated by the model derived in this thesis. What we might ask ourselves now is: can we measure the mobility of charge carriers in thin film devices directly? The next section will answer this question.

4.2.3 Current Extraction by Linear Increasing Voltage (CELIV)

The experimental parameters used for all Photo-CELIV experiments were: $\tau_{\text{delay}} = 2\mu s$, $\tau_{\text{LVR}} = 70\mu s$, $V_{\text{max}} = 8V$, and $A = 0.11\ V/\mu s$. After the first cycle, in which the transient Photo-CELIV was recorded, the LRV was applied a second time without laser excitation, and j(0) was recorded. The laser pulse excitation wavelength was chosen to be at 335 nm, to avoid high absorption by the incident interface, based on the absorption spectrum of F8BT (figure 51). Also, as previously discussed, Photo-CELIV requires the existence of photocharge uniformly distributed within the bulk.

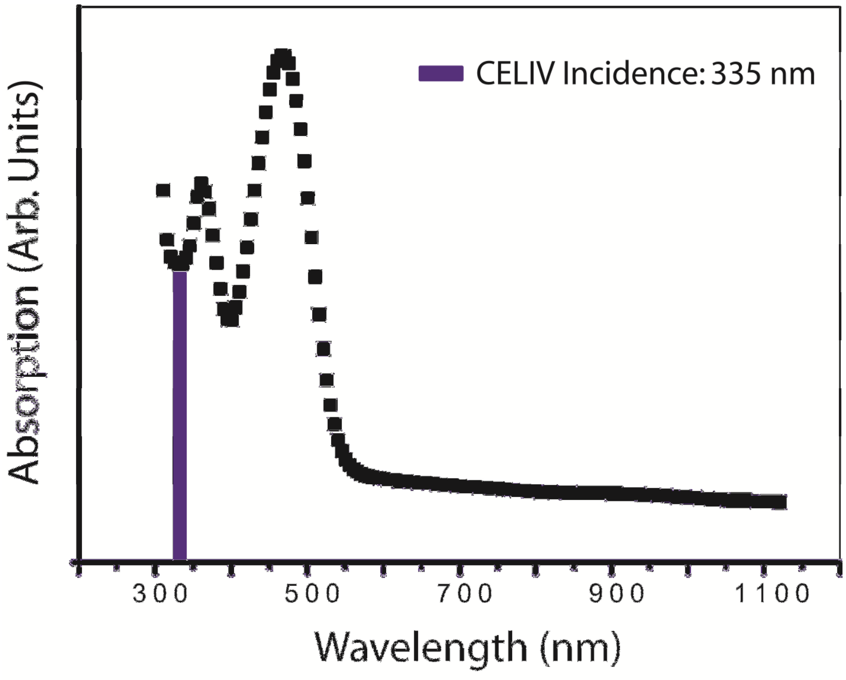

Figure 51 – Absorption spectrum of F8BT: CELIV laser excitation wavelength was choose to be at 335 nm.

Figure 52a shows the full response of a Photo-CELIV transient (Δj) superimposed to j(0), obtained at 350 K. The fact that Δj decreases to almost zero indicates that all photo-generated charge carriers are extracted by the first LVR. During the second LVR, j(0)remains almost constant, which clearly shows that the injection of charge carriers by the electrodes is negligible. Otherwise, one would be able to observe an increasing current j(0). In general, the amount of photo-generated charges is small compared to the charge transported by the displacement current Δj < j(0), which indicates that the electric field throughout the sample is not strongly disturbed by charges photo-generated in the bulk.

Photo-CELIV profiles (Δj) obtained at different temperatures are shown in Figure 52b. While the maxima of the Δj peak decreases and the respective width increases for lower temperatures, the total amount of extracted charge carriers remains almost constant.

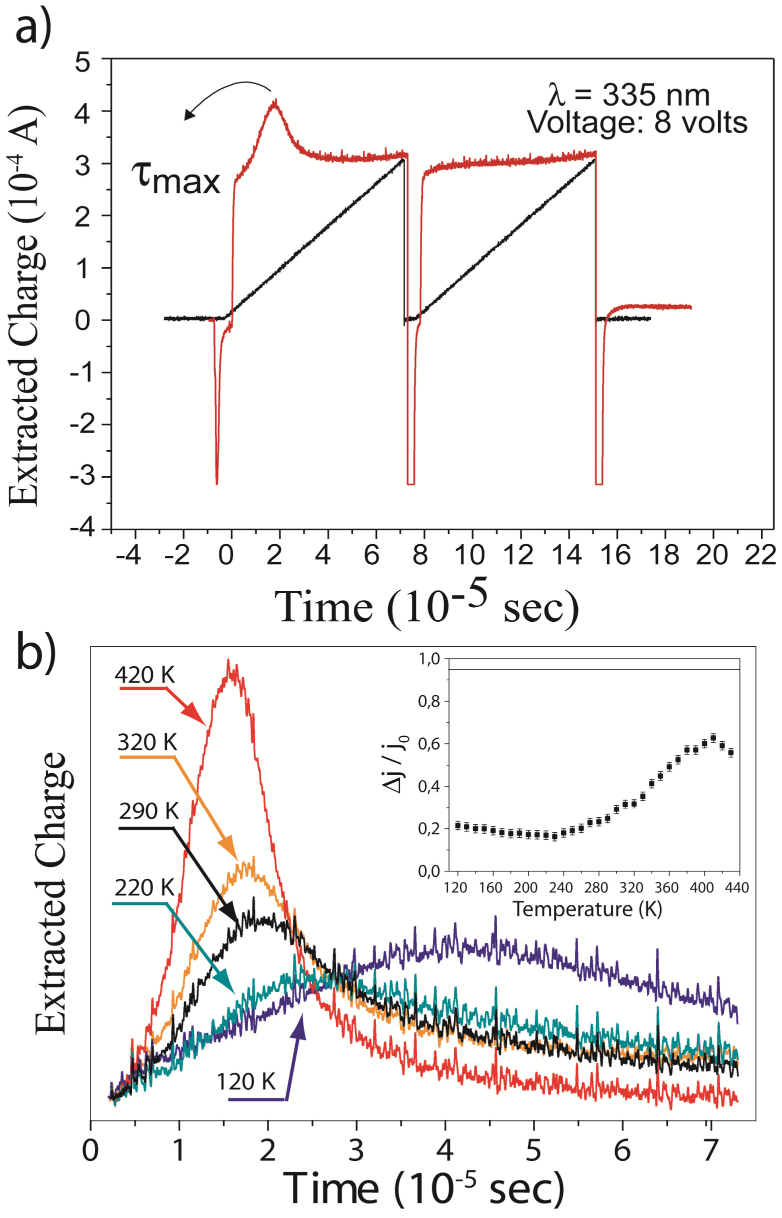

Figure 52 – a) Photo-CELIV current extraction obtained for the Al/F8BT/ITO device at 350 K. b) Photo-CELIV current profile for the Al/F8BT/ITO device at several temperatures. As an inset are the $\Delta J / J(0)$ values plotted as a function of temperature.

The mobility was calculated using equation 64 and is displayed in the whole temperature range of 120 to 420 K on a $\ln(\mu_0)\, vs\, T^{-2}$ curve, as shown in Figure 53a. This curve also reveals the same two characteristics features observed in thick-film TOF measurements and by the calculated mobility on IxV curves of thin films: a break in the slope at 205 K and a deviation from a straight line in the temperature range of 315 to 390 K.

The results exhibited in Figure 53a were also analyzed by the GDM model assuming a Gaussian DOS and hopping transport. Both linear regimes, above and below 205 K (T_c), were also fitted by the equations 62a and b, and the calculated ratio between the two slopes was ($\frac{257}{178}$=1.4 ± 0.3), which is in reasonable agreement with the ratio of the slopes predicted by the GDM model for a ND-D transition[87]. Since the GDM model correlates T_c with the ND-D transition, the charge transport across thin F8BT films is non-dispersive above T_c and dispersive below it, the same conclusion we reached for TOF in thick films and thin films IxV.

It is worth mentioning that, in TOF experiments, the critical temperature of the ND-D transition is defined as the temperature at which the charge relaxation time become longer than the charge extraction time, so thermal equilibrium is not attained during the transit time. Under these conditions, it was concluded that the mobility is no longer a well-defined material property and become thickness dependent[21].

However, in Photo-CELIV experiments it is difficult to define an extraction time as is in TOF. Hence, we analyzed the dispersiveness parameter which is usually quantified by the ratio $t_{1/2}/\tau_{max}$, where $t_{1/2}$ is the width at half maximum of the conduction current profile of Δj [20]. Thus, the higher (lower) $t_{1/2}/\tau_{max}$ is, the more (less) dispersive the charge transport. Nevertheless, it is important to emphasize that Bange et. al.[93] have drawn some important conclusion on the interpretation of $t_{1/2}/\tau_{max}$ as a dispersion parameter in the case of non-equilibrium charge carriers. According to them, $t_{1/2}/\tau_{max}$ also increases with the bimolecular recombination rate, which may lead to false interpretation.

Figure 53b shows the dependence of the $t_{1/2}/\tau_{\max}$ ratio on the square of the inverse temperature. A maximum is observed at 220 ± 20 K, which coincides with the change of slope of the $t_{1/2}$ vs T^2 curve and the low-temperature peak observed in the tanδ measurement. Above 315 K, a change in the dependence of $\tau_{\max}$ on temperature is clearly observed. Concerning the effect of bimolecular recombination on $t_{1/2}/\tau_{\max}$,[93] the temperature dependence of bimolecular recombination has been measured for different organic polymer and it has been shown that the recombination rate increases with temperature[99,100]. In our case, the opposite behavior was observed, implying that the decrease in $t_{1/2}/\tau_{\max}$ at higher temperatures is indeed due to the decrease in the degree of dispersiveness of the transport rather than to changes in the bimolecular recombination rate. Besides, the inset of figure 52b indicates that $\Delta j/j(0)$ is nearly constant and equal to 0.2 between 120 and 300 K, so a large contribution from bimolecular recombination is not expected[93].

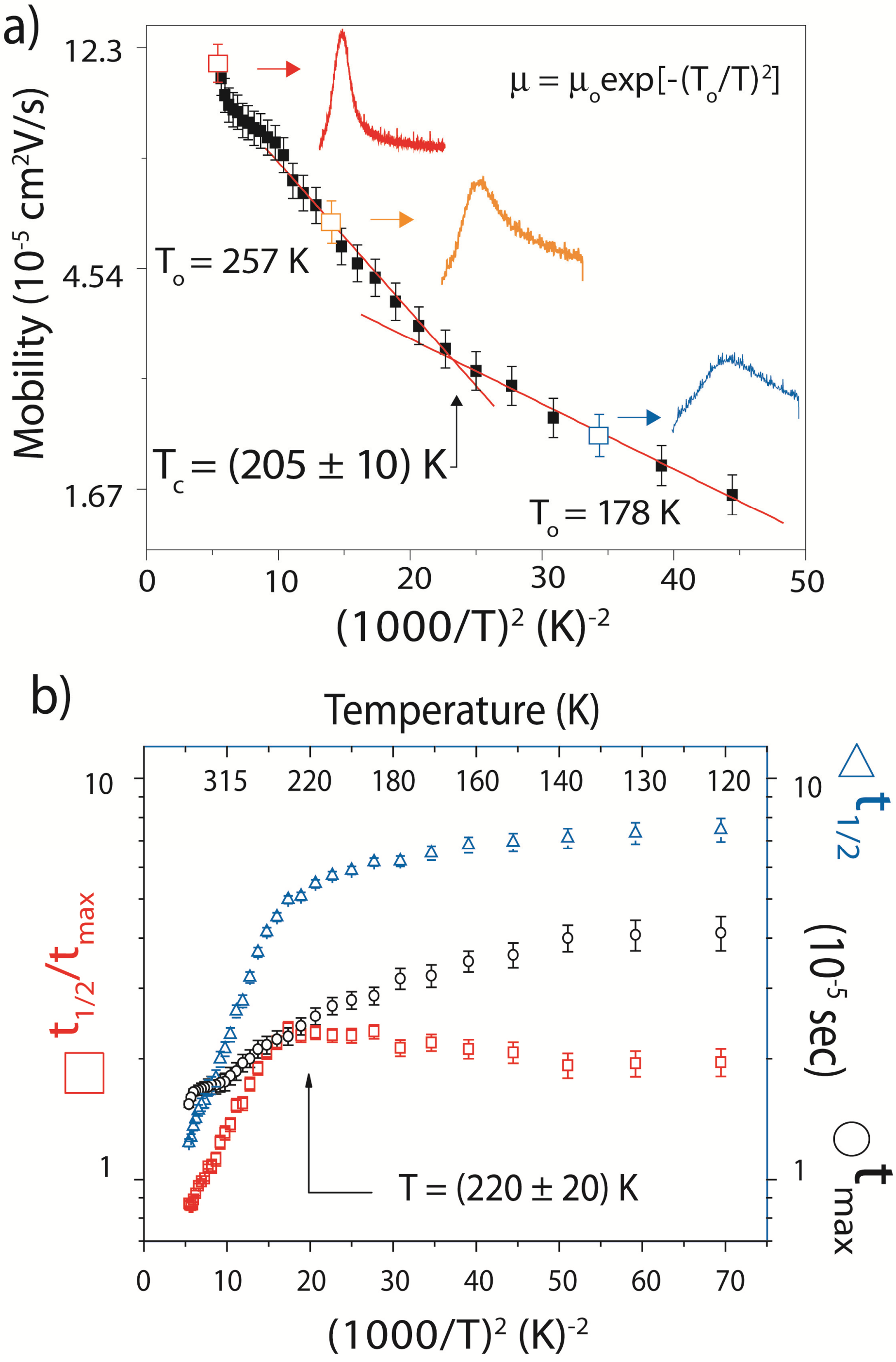

Figure 53 – a) Mobility calculated from Photo-CELIV transients as a function of temperature together with the dielectric relaxation - tanδ - in order to correlate changes in the mobility with molecular relaxations. b) Plot of $t_{1/2}$, t_{max} and $t_{1/2}/t_{max}$ obtained from the CELIV measurements as a function of $1000/T^2$ and T.

Nevertheless, the kink in the slope of the $\ln(\mu_0)\ vs\ T^{-2}$ curve and a coinciding change in the behavior of the dispersiveness parameter ($t_{1/2}/\tau_{\max}$) were observed in the Photo-CELIV data as well, which can be considered as a sign of a ND-D transition. Therefore, the change observed in the Photo-CELIV response is likely to be related to the ND-D transition at approximately 205 K.

Besides the fact that the ND-D transition may be explained within a pure geometrical approach, the coincidence of this transition with the onset of the side group motions is a strong indication that the change in the local packing plays a role in this behavior. Regarding the changes observed in the mobility behavior around the glass transition temperature, it is concluded that the motion-induced narrowing of the DOS around T_g, together with the time-dependent disorder of the DOS during the glass transition process (315 to 390 K), explains the mentioned modification. A similar conclusion was drawn for the mobility of thick films measured by TOF.

5 Summary: Correlation between Molecular Dynamics and Structure with Electronic Properties

Thermal methods, namely DTMA, DSC and ^{1}H, indicated the presence of three main molecular relaxations in thick films, which were assigned as β-relaxation, α-relaxation (or glass transition) and crystal-to-crystal transitions. Similar results concerning molecular relaxation for polyfluorene materials have been published elsewhere[38,95,102-104].

NMR methods allowed us to understand the molecular nature of the relaxations, the β process being associated to the side-chain movements and the glass transition to segmental motions on the polymer backbone. WAXD measurements revealed that the glass transition precedes the dissipation of the lamellar β-phase, which is induced by the slow solvent evaporation and is known to be meta-stable. In this sense, the onset of the molecular motions in the amorphous regions allows the reorganization of the chains, so that a crystal-to-crystal transition can occur. The new and more stable α-phase is considered ordered, being the polymer backbones organized in a helicoidal arrangement. At higher temperatures, the polymer reaches the melting point of the α-phase, as revealed by DSC and WAXD.

The conduction in disordered polymers is expected to occur via hopping between energetic-distinct sites, normally assumed to be dispersed in a Gaussian distribution, known as Gaussian Density of States (DOS). However, these sites are populated with trapping states, which immobilize the charge carriers, limiting the current throughout the polymer film. In recent works, trapping states are assumed to be distributed according to a Gaussian distribution law. Both the

DOS and the trapping states distribution can broaden with disorder. It is worth remembering that the origin of trapping states, as addressed in chapter 2, may be explained by the Polaron Model. Therefore, the morphology and/or packing structure of polymer chains play an important role in the description of the energy and distribution of traps.

As a result, the electrical properties of both thick and thin films were similar. Despite the fact that thin films did not present a crystal-to-crystal transition (comparison of real impedances versus temperature), the influence of the molecular dynamics on the temperature-dependence of the mobility was essentially identical. Hence, we will limit our discussion to the results regarding thin films, but using what was learnt from the molecular characterization of the thick films.

Figure 54 presents the mobility measured by Photo-CELIV (a) and the one extracted by IxV modeled curve (b), both together with the dielectric loss function $tan\delta = \frac{\varepsilon''}{\varepsilon'}$ at 1Hz, measured by impedance spectroscopy in thin film devices. The coincidence between the characteristic features of the mobility curves and the peaks in the tanδ vs. $1/T^2$ dependence is remarkable.

The coincidence between the β-relaxation peak in the tanδ vs. T^{-2} and the change in slope of the $\ln(\mu_0)\, vs\, T^{-2}$ deserves discussion. As already mentioned, the β-relaxation is related to the onset of molecular motions on the side groups at about 210 K. Thus, the change in dispersiveness of the charge transport, as described by the GDM and confirmed by the dispersiveness parameter ($t_{1/2}/\tau_{max}$), is also likely to be related to a change in the structural disorder or fluctuation of the local conjugation length, which occur due to the change in the local packing induced by the molecular agitation above the β-transition temperature. Essentially, it has been already shown that the onset of movement on the side-chain increases the inter-chain packing-distance[38], which, in the Polaron Model, means that the energy of trapping states might start to diminish at this point.

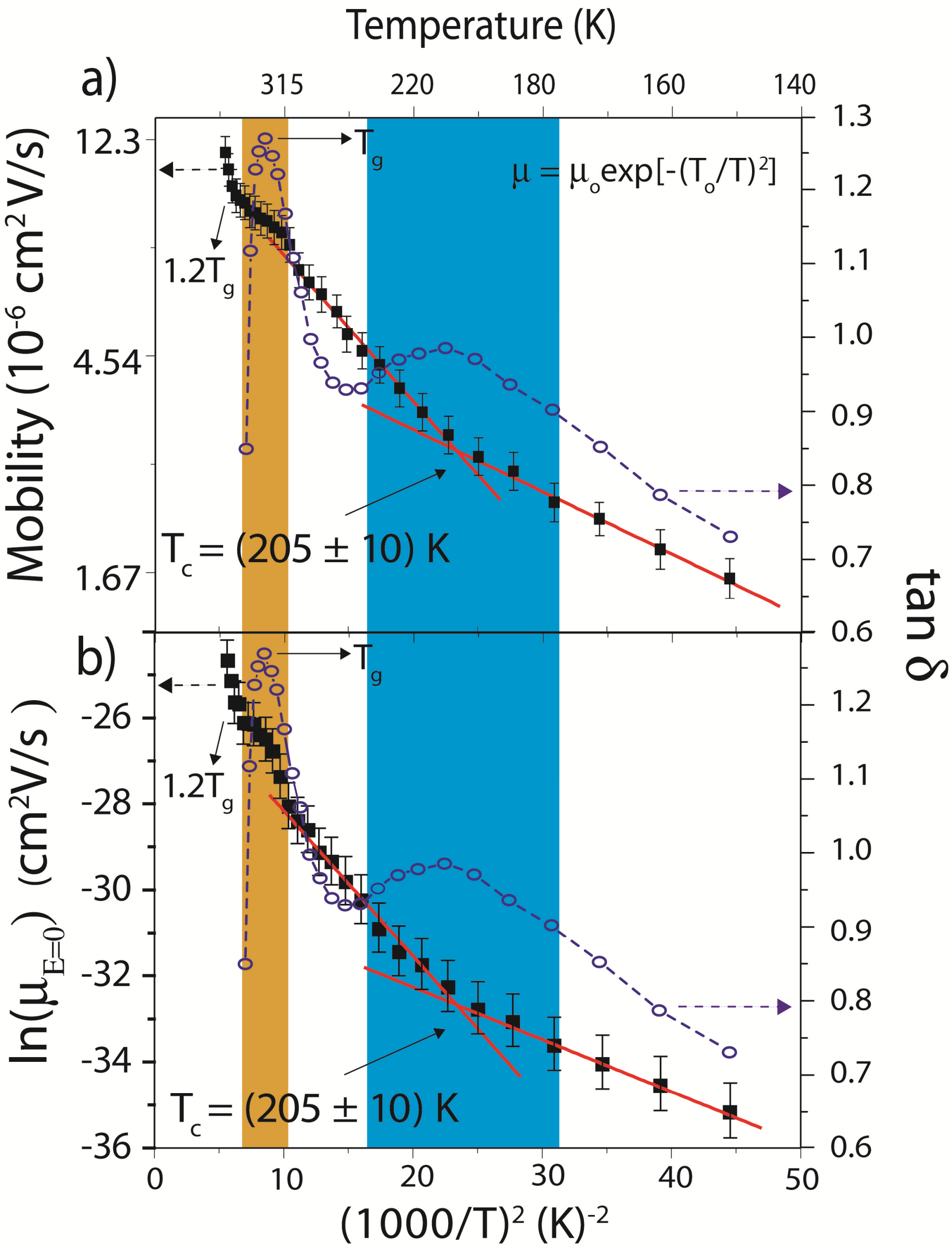

Figure 54 – **Comparison between mobility measured by CELIV and modeled by Current-Voltage characteristics of thin-film devices. The blue circle is the dielectric loss in order to illustrate the correlation between the changes observed on the mobility curves and the molecular dynamics measured and discussed in chapter 2.**

Another point for discussion is the connection of the deviation from the straight line starting at 315 K and the occurrence of the glass transition. The faster increase in mobility above Tg ($T > 1.2\ Tg$) can be attributed to a motional narrowing effect which occurs due to the narrowing of the DOS induced by the glass transition. In this situation, the carriers experience, on average, a smoother energy landscape during their motion, so the slope of the $\ln(\mu_0)\, vs\, T^{-2}$ curve is increased above $1.2\,Tg$. At temperatures around Tg, the time scale of the collective molecular reorientations seems not to be fast enough for the carrier to experience the narrowed DOS, but nor too slow so that the disorder can be considered static. In other words, around or slightly above Tg, one may consider that the energy disorder becomes temperature-dependent, so a deviation from the GDM predicted behavior is observed. This is consistent with the non-linear behavior observed during the glass transition. An equivalent view has been proposed by Giro et. al.,[98] who suggested that, below Tg, there will be a strong localization of charges due to the geometrical restrictions, which do not favor hopping between neighboring sites, but rather trapping and detrapping. Following this idea, one may conclude that, below the glass transition temperature, the conduction is trap-controlled and, above such temperature, the trapped charge carriers are liberated by the backbone molecular motion. This indicates that a structural detrapping mechanism dominates the charge conduction above 1.2 Tg.

A naive picture of this explanation is given in figure 55, in which we illustrate the hopping conduction, and the DOS at four temperatures: a) below β-relaxation; b) around β-relaxation; c) around α-relaxation (glass transition); and d) above α-relaxation. In our stretch, τ_i is referred as the hopping time and E_i to the trap energy:

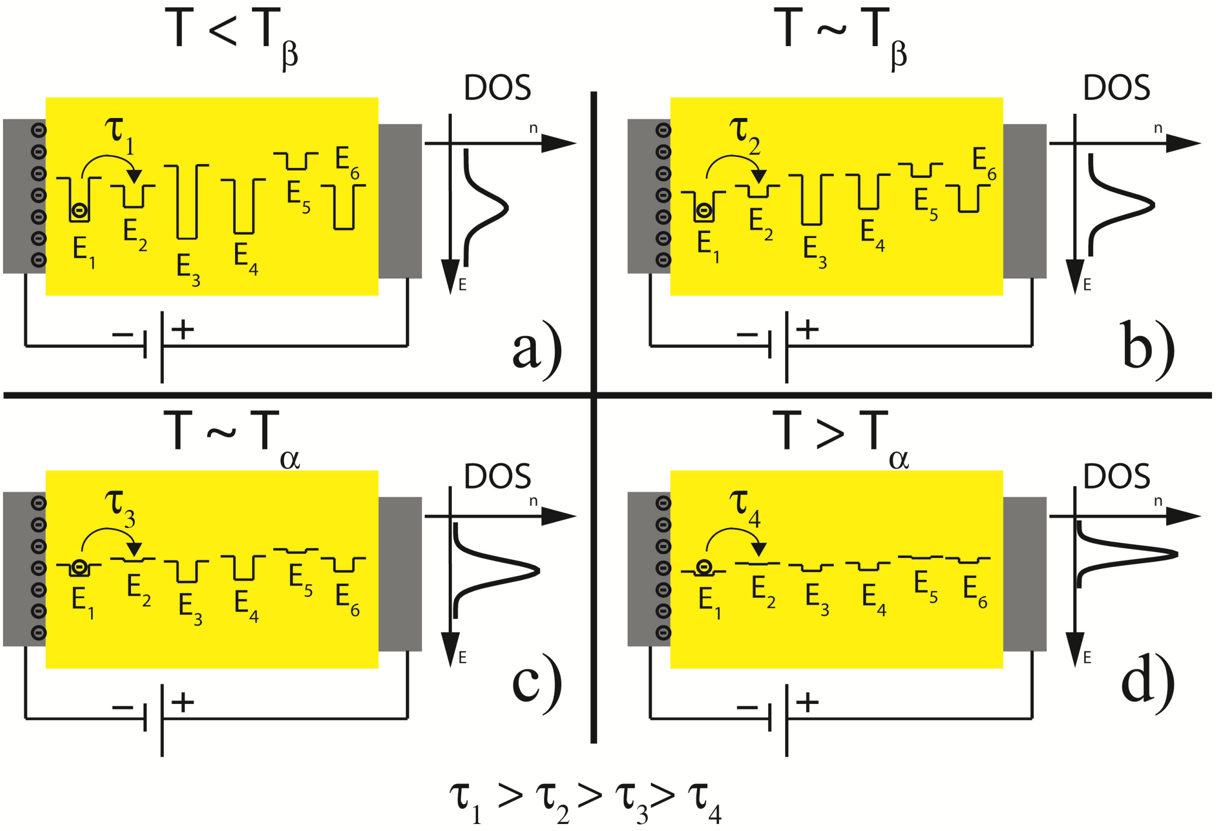

Figure 55 - A naive picture of the structural detrapping mechanism in F8BT samples (τ is the hopping time) for several temperatures.

Below β-relaxation, no significant molecular movements occur; consequently, the energy-trap distribution is located at higher energies, and the DOS is broader, due to the inhomogeneous packing structure. Around β-relaxation, the traps energies diminish because of the side-chain movement, which produces a small increase in the lateral spacing and in the stacking distance of the phenyl rings[38]. However, around and above T_g, the increase in the amplitude of the collective chain motions produces a significant increase in the stacking distance of the phenyl ring and promotes the liberation of trapped charges. Therefore, the DOS is narrowed, and the mobility increases significantly.

Another fact which deserves attention is that, in the case of thick film, the interface between amorphous and crystalline regions in the sample are critical for charge trapping formation[20,39]. In this sense, above *Tg*, and considering the WAXD results, one may expect that this interphase becomes more prevalent, due to the crystallization of the α-phase. This would lead to an increasing of number of traps, as suggested by figure 41, chapter 4. However, although the density of traps seems to increase, its energy depth diminish and the hopping time (τ) decrease. Consequently, the conduction is made easier.

6 Conclusion and Perspectives

In summary, we presented a study on the temperature-dependent electrical properties in F8BT thin films and correlations with the molecular structure and dynamics. It was observed that the temperature dependence of the mobility, for both thick and thin films, exhibit two main changes, associated to a non-dispersive to dispersive (ND-D) transition, the first predicted by the Gaussian Disorder Model and the second related to the glass transition of the material. Despite the fact that the ND-D transition may be explained within a pure geometrical approach, the coincidence of this transition with the onset of the side-group motions is a strong sign that the change in the local packing plays a role in this behavior.

Regarding the changes observed in the mobility behavior around the glass transition temperature, it is concluded that the motion-induced narrowing of the DOS above $1.2T_g$, together with the time-dependent disorder of the DOS during the glass transition process (315 to 390 K), explains the mentioned modification. As far as we know, this is the first time that such effects have been observed in a functional electroluminescent polymer, such as F8BT.

Charge transport in disordered systems, as conjugated polymer films, is a complex phenomenon that involves interdependences between mobility and the density of carriers, the effect of the external electric field, and when the temperature is changed, also the dynamic of different molecular segments and thermal structural modifications. This thesis intended to give a contribution to the understanding of this intricate area of research, trying to make a correlation between structural and morphological changes in thick and thin films of F8BT, using different techniques of structural analysis and electrical characterization.

Due to the complexity of this field of research, several future perspectives have appeared. The first challenge we decide to overcome, is the use of thin films in both NMR and WAXD. Together with co-workers, we started the development of procedures to obtain the necessary amount of spin-coating thin films to be applied in such techniques. This work is in progress and some results have led to the same conclusion we have had in chapter 4: thin film does not present crystalline portion as it does in thick film.

Photo-CELIV experiment on samples with different thickness is of a great importance on the interpretation of the ND-D transition. From the GDM model, the kink observed for such transition is thickness dependent. Therefore, in order to confirm or not the GDM model for our system we might explore the thickness of our sample.

Also, we may repeat the same experiments in polymer which do not present aliphatic chain (side-chain), e.g., the pure PPV. If the kink observed at lower temperature in the mobility curve seems to be influenced by the relaxation of the side-chain, the PPV should not reveal such characteristic.

We also want to dedicate more attention to the current-voltage model used to describe the IxV curve of thin films. The work published by Nicolai[86] has shown that interesting advances in modeling current in disordered materials have been reached. Therefore, we are now focused on the development of a similar IxV model.

Finally it would be of great interest to explorer the Thermal Stimulated Current (TSC) method in our samples. Such technique is closely connected with trapping and detrapping phenomena. Therefore new finding could come from such studies. Actually, I have made such measurements during my times in Darmstadt. However, we were not able to go above to the room temperature, and the glass transition influence over the TSC data was not registered. Nonetheless, we are implementing this technique and it will be available soon.

References

1 TANG, C.W.; VANSLYKE, S.A. Organic electroluminescent diodes. *Applied Physics Letters*, v. 51, p. 913-916, 1987.

2 POPE, M.; SWENBER, C.E. *Electronic processes in organci crystals and polymers*. London: Oxford University Press, 1999.

3 BURROUGHES, J. H. et al. Light-emitting-diodes based on conjugated polymers. *Nature*, v. 347, n.6293, p. 539-541, 1990.

4 FRIEND, R. Amorphous-semiconductors - making multilayered samples, *Nature*, v. 331, n.6152, p. 118-119, 1988.

5 FRIEND, R. H.; BURROUGHES,J. H. Charge injection in conjugated polymers in semiconductor-device structures. *Faraday Discussions*, v. 88, p. 213, 1989.

6 BURROUGHES, J. H. et al. Light-emitting-diodes based on conjugated polymers. *Nature*, v. 347, n.6293, p. 539-541, 1990.

7 FRIEND, R. Organic conductors - inclusion of chalcogens raises electron-mobility. *Nature*, v. 329, n.6134, p. 14-15, 1987.

8 FRIEND, R. Molecular electronics - bringing molecules to order. *Nature*, v. 352, n.6334, p. 377-377, 1991.

9 FRIEND, R. H. et al. Electroluminescence in conjugated polymers. *Nature*, v. 397, n.6715, p. 121-128, 1999.

10 FRIEND, R.; BRADLEY, D.; HOLMES, A. Polymer leds. *Physics World*, v. 5, n.11, p. 42-46, 1992.

11 FRIEND, R.; BURROUGHES, J.; SHIMODA, T. Polymer diodes. *Physics World*, v. 12, n.6, p. 35-40, 1999.

12 MUCCINI, A. A bright future for organic field-effect transistors. *Nature Materials*, v. 5, p.605-613, 2006.

13 MALLIARAS, G.; FRIEND, R. An organic electronic prime. *Physics Today*, v.58, n.5,p.53-58, 2005.

14 BIANCHI, R. F. et al., Photo-oxidation phenomenon of MH-PPV films studied by ellipsometry and infrared spectroscopy. *Molecular Crystals and Liquid Crystals*, v. 374, p. 457-462, 2002.

15 SCOTT, J.C. et al. Degradation and failure of MEH-PPV light-emitting diodes. *Journal of Applied Physics*, v. 79, n.5, p. 2745-2751, 1996.

16 SUTHERLAND, D.G.J. et al. Photo-oxidation of electroluminescent polymers studied by core-level photoabsorption spectroscopy. *Applied Physics Letters*, v. 68, n.15, p. 2046-2048, 1996.

17 SCOTT, J.C. et al. MEH-PPV light-emitting diodes: mechanisms of failure. *Molecular Crystals and Liquid Crystals Science and Technology Section A*, v. 283, p. 57-62, 1996.

18 ATREYA, M. et al. Stability studies of poly(2-methoxy-5-(2 '-ethyl hexyloxy)-p-(phenylene vinylene). *Polymer Degradation and Stability*, v. 65, p. 287-296, 1999.

19 KHILLAN, R. K.; SU,Y.; VARAHRAMYAN, K. The degradation of poly [2-methoxy-5-(2-ethylhexoxy)-1,4-phenylene vinylene] thin films studied by capacitance-voltage analysis and attenuated total reflection infrared spectroscopy. *Thin Solid Films*, v. 483, n.2, p. 416-419, 2005.

20 KLINE, R. J.; McGEHEE, M. D. Morphology and charge transport in conjugated. *Journal of Macromolecular Science*, v. 46, p. 27-45, 2006.

21 BORSENBERGER, P. M. et al. The role of disorder on charge transport in molecularly doped polymers and related materials. *Physics of Status Solid*, v. 149, n.9, p. 10-47, 1993.

22 KÖSE, M. E. Evaluation of Excitonic coupling and charge transport integrals in P3HT nanocrystal. *Journal of Physical Chemistry C*, v. 115, p. 13076-13082, 2011.

23 CHEN, P. et al. Side-chain effects on the morphology and properties of fluorine-based alternating copolymers. *Polymer International*, v. 56, p. 996-1005, 2007.

24 ABKOWITZ, M. et al. Behavior of the drift mobility in the glass transition region of some hole-transporting amorphous organic films. *Journal of Applied Physics,* v. 52, p. 3453-3457, 1981.

25 DONLEY, C. et al. Effect of packing structure on the optoelectronic and charge transport properties in poly(9,9-di-n-octylfluorene-alt-bezothiadiazole). *Journal of the American Chemical Society,* v. 127, p. 12890-12899, 2005.

26 TAPPI: flexible Electronics: revolutionary products and carrer opportunities for criative engineers: Available in: <http://www.tappi.org/content/events/11student/New_Technologies.pdf>. Accessed in: 08/2011

27 SONY'S 11-inch XEL-1 OLED TV: Available in: <http://www.hdtvinfo.eu/news/hdtv-articles/sony-announces-a-27-inch-oled-tv.html>. Accessed in: 08/2011

28 SONY Develops a "Rollable" OTFT^{*1}-driven OLED Display that can wrap around a pencil: Available in: <http://www.sony.net/SonyInfo/News/Press/201005/10-070E/index.html>. Accessed in: 08/2011

29 SONY to launch 17″ and 25″ OLED TVs: Available in: <http://www.geek.com/articles/chips/sony-to-launch-17-and-25-oled-tvs-20110217/ >. Accessed in: 08/2011

30 SPERLING, L.H. *Introduction to physical polymer science.* New York: Wiley Interscience Publication, 1992.

31 ENGEL, T. *Quantum chemistry and spectroscopy.* Washigton: Prentice Hall, 2006.

32 FRIEND, R. Conjugated polymer: new material for optoelectronics application. *Pure Applied Chemistry*, v. 73, n. 3, p. 425-230, 2011.

33 LONGUETHIGGINS, H. C.; SALEM, L. The alternation of bond lengths in long conjugated chain molecules. *Proceedings of the Royal Society of London Series A*, v. 251, p. 172-185, 1959.

34 SALEM, L. *The molecular orbital theory of conjugated systems.* London: Benjamin, 1966. p. 214.

35 PEIERLS, R.E. *Quantum theory of solids.* Oxford: University Press, 1955. p. 108.

36 CHIANG, C. K. et al. Electrical-conductivity in doped polyacetylene. *Physical Review Letters*, v.39, n.17, p. 1098-1101, 2977

37 DURRANI, M. Physicist shares chemistry Nobel prize. *Physics World*, v.13, n.11, p.6-7, 2000.

38 FARIA, G. C. et al. A multitechnique study of structure and dynamics of polyfluorene cast films and the influence on their photoluminescence. *Journal of Physics Chemistry B*, v.113, p. 11403-11413,2009.

39 SEANOR, D.A.; *Electrical properties of polymers*. London: Academic Press, 1982.

40 BRADLEY, D. D. C. et al. Structural studies of oriented precursor route conjugated polymers. *Synthetic Metals*, v. 17, n.3, p. 473-478, 1987.

41 BRADLEY, D. D. C.; EVANS,G. P.; FRIEND, R.H. Characterization of poly(phenylenevinylene) by infrared and optical-absorption. *Synthetic Metals*, v. 17, n.3, p. 651-656, 1987.

42 MURASE, I. et al. Highly conducting poly(phenylene vinylene) derivatives via Soluble precursor process. *Synthetic Metals*, v. 17, n.3, p. 639-644, 1987.

43 BRADLEY, D. D. C.,; FRIEND, R. H. Photoexcitation in poly(phenylenevinylene). *Journal of Molecular Electronics*, v. 5, n.1, p. 19-24, 1989.

44 Light emitting-diodes based on conjugated polymers: Available in: <http://apps.webofknowledge.com/full_record.do?product=UA&search_mode=CitationReport&qid=2&SID=N2b43D75jhG4k@gPBe4&page=1&doc=1>. Accessed in: 08/2011

45 FUKUDA, M.; SAWADA, K.; YOSHINO, K.; Fusible conducting poly(9-alkylfluorene) and poly(9-9dialkylfluorene) and their characteristics. *Japanese Journal of Applied Physics*, v.8, p.1433-1435, 1989.

46 RANGER, M.; RONDEAU,D.; LECLERC, M. New well-defined poly(2,7-fluorene) derivatives: photoluminescence and base doping. *Macromolecules*, v. 30, n.25, p. 7686-7691, 1997.

47 KREYENSCHMIDT, M. et al. Thermally stable blue-light-emitting copolymers of poly(alkylfluorene). *Macromolecules*, v. 31, n.4, p. 1099-1103, 1998.

48 MILLARD, I.S. High-efficiency polyfluorene polymers suitable for RGB applications. *Synthetic Metals*, v. 111, p. 119-123, 2000.

49 KULKARNI, A.P.; JENEKHE, S. A. Blue light-emitting diodes with good spectral stability based on blends of poly(9,9-dioctylfluorene): interplay between morphology, photophysics, and device performance. *Macromolecules*, v. 36, n.14, p. 5285-5296, 2003.

50 CHO, H.J. et al. Synthesis and characterization of thermally stable blue light-emitting polyfluorenes containing siloxane bridges. *Macromolecules*, v. 36, n.18, p. 6704-6710, 2003.

51 JACOB, J. et al. Poly(tetraarylindenofluorene)s: new stable blue-emitting polymers. *Macromolecules*, v. 36, n.22, p. 8240-8245, 2003.

52 HWANG, D.H.; PARK, M. J.; LEE, J. H. EL properties of stable blue light-emitting polyfluorene copolymers. *Materials Science & Engineering C-Biomimetic and Supramolecular Systems*, v. 24, n.2, p. 201-204, 2004.

53 LEE, J. et al. Stabilized blue luminescent polyfluorenes: introducing polyhedral oligomeric silsesquioxane. *Macromolecules*, v. 37, n.23, p. 8523-8529, 2004.

54 LEE, K.S. et al. Synthesis and characterization of stable blue light-emitting poly (spirobifluorene) derivatives containing alkoxy group. *Journal of Polymer Science Part a*, v. 43, n.11, p. 2316-2324, 2005.

55 AHARON, E. et al. Stable blue emission from a polyfluorene/layered-compound guest/host nanocomposite. *Advanced Functional Materials*, v. 16, n.7, p. 980-986, 2006.

56 CHOCHOS, C.L. et al. Thermally stable blue emitting terfluorene block copolymers. *Journal of Physical Chemistry B,* v. 110, n.10, p. 4657-4662, 2006.

57 TSENG, Y.H. et al. Stable organic blue-light-emitting devices prepared from poly[spiro(fluorene-9,9'-xanthene)]. *Macromolecules*, v. 38, n.24, p. 10055-10060, 2005.

58 SHIH, P.I. et al. Stable and efficient white electroluminescent devices based on a single emitting layer of polymer blends. *Advanced Functional Materials*, v. 16, n.12, p. 1582-1589, 2006.

59 LEHNHARDT, M.; RIEDL, T.; RABE, T.; KOWALSKY, W. *Organic electronics.* v. 12 p. 486-489, 2011.

60 SCHIDLEJA, M.; MELZER, C.; VON SEGGERN, H. The organic light-emmiting field effect transistor. *Frequenz.* v. 62 p. 100-107, 2011.

61 LEE, C. L. et at. Investigation of exciton dissociation in poly(9,9-dioctylfluorene-co-benzothiadiazole): 2,3,7,8,12,13,17,18-octaethyl-21h,23h-porphyrin platinum (II) system for photovoltaic device application. *Journal of the Nanoelectronics and Optoelectronics.* v.5, p. 170-176, 2010.

62 STROBL, G. *The physics of polymer.* Feiburg: Springer, 1997.

63 MURAYAMA, T. *Dynamic mechanical analysis of polymeric material.* New York: Elsevier, 1978.

64 deAZEVEDO, E. R. *Novas metodologias de ressonância magnética nuclear para o estudo da dinâmica lenta em materiais orgânicos no estado sólida: aplicações em polímeros e proteínas.* 2001. 194. Tese (Doutorado), Instituto de Física de São Carlos – Universidade de São Paulo, São Carlos, 2001.

65 SCHMIDT-ROHR, K.; SPIESS, H. W. *Multidimensional solid-state nmr and polymers.* New York: Academic Press, 1994.v. 1, p. 478.

66 deAZEVEDO, E. R.; BONAGAMBA, T. J. Nuclear magnetic resonance spectroscopy, In: *Handbook of Applied Solid State Spectroscopy.* New York: Springer,2006.v. 1, p. 1-63.

67 HAEBERLEN, U. *High resolution NMR in solids.* New York: Academic Press, 1976.v. 1, p. 190.

68 deAZEVEDO, E. R.; BONAGAMBA, T. J. Molecular dynamics and local molecular conformation in solid materials studied by nuclear magnetic resonance. *Brazilian Journal of Physics*, v.36, p.61-74, 2006.

69 SARLES, L. R.; COTTS R. M. Double nuclear magnetic resonance and the dipole interaction in Solids. *Physical Review*, v.111, p.853-859, 1958.

70 ANDREW, E. R.; BRADBURY A.; EADES R. G. Removal of dipolar broadening of nuclear magnetic resonance spectra of solids by specimen rotation. *Nature,* v.183, p.1802-1803, 1959.

71 LOWE I. J. Free induction decays of rotating solids. *Physical Review Letters,* v.2 p.285-287, 1959.

72 ANDREW E. R.; EADES R. G. Possibilities for high-resolution nuclear magnetic resonance spectra of crystals**.** *Discussions of the Faraday Society.* v.38-42, 1962.

73 MARIC, M.M.; WAUGH, J. S. NMR in rotating solids. *Journal of Chemical Physics*, v. 70, p. 3300-3316, 1979.

74 SCHAEFER, J.; STEJSKAL, E. O. Carbon-13 nuclear magnetic resonance of polymers spinning at the magic angle. *Journal of American Chemical Society*, v.98, p.1031-1032, 1976.

75 deAZEVEDO, E.R. et al. Intermediate motions as studied by solid-state separated local field NMR experiments. *Journal of Chemical Physics*, v.128, p.1-11, 2008.

76 VANVLECK, J. The dipolar broadening of magnetic resonance lines in crystals. *Physical Review*, v.74, p.1168-1183, 1948.

77 CLOUGH, K. W. et al. The stochastic theory of the nuclear magnetic resonance line in rotating solids**.** *Physics Society of London*, v.79, p. 457-467, 1962.

78 deAZEVEDO, E. R. et al. Principles of centerband-only detection of exchange in solid-state nuclear magnetic resonance, and extension to four-time centerband-only detection of exchange. *Journal of Chemical Physics,* v.112, p.8988-9001, 2000.

79 HIRSCHINGER, J. et al. Chemical exchange effects in the NMR spectra of rotating solids. *Journal of Chemical Physics*, v.85, p. 4248, 1986.

80 REICHERT, D.; et al. CONTRA: improving the performance of dynamic investigations in natural abundance organic solids by mirror-symmetric constant-time CODEX. *Journal of Magnetic Resonance*, v. 191, p. 141-147, 2007.

81 LAMPERT, M.; MARK, P. *Current injection in solids.* London: Academic Press, 1970.

82 LUPTON, J.J.; SAMUEL, I.D.W. Temperature-dependent device model for polymer light-emitting diodes: significance of barrier height. *Synthetic Metals*, v. 111, n.381-384, 2000.

83 LUPTON, J.J.; SAMUEL, I.D.W. Temperature-dependent single carrier device model for polymeric light-emitting diodes. *Journal of Applied Physics D*, v. 32, n.2973-2984, 1999.

84 BLOM, P.W.M. et al. Electric-field temperature dependence of the hole mobility in poly(p-phenylene vinylene). *Physical Review B*, v. 55, n. 2, p. 656-659, 1997.

85 MARTENS, H.C.F. et al. Comparative study of hole transport in poly(p-phenylene vinylene) derivatives. *Physical Review B*, v. 61, n.11, p. 7489-7493, 2001.

86 NICOLAI, H.T. et al. Electron traps in semiconducting polymers: exponential versus Gaussian trap distribution. *Physical Review B*, v. 83, p. 195204-195209, 2011.

87 BÄSSLER, H.; BORSENBERGER, P. M. The transition from nondispersive to dispersive charge transport in vapor deposited films of 1-phenyl-3-*p*-diethylamino-styryl-5-*p*-diethylphenylpyrazoline (DEASP). *Chemical Physics*, v. 177, p. 763-771, 1993.

88 LAQUAI, F. et al. What determines the mobility of charge carriers in conjugated polymers?, *Philosophical Transactions of the Royal Society A*, v. 365, p. 1437-1487, 2007.

89 PAASCH, G.; SCHEINERT, J. Charge carrier density of organics with Gaussian density of states: analytical approximation for the Gauss–Fermi integral. *Journal of Applied Physics*, v. 107, p. 104501-104505, 2010.

90 MACDONALD, J. *Impedance spectroscopy.* Chapel Hill: John Wiley & Sons, 1987.

91 HAVRILIAK, S.; HAVRILIAK, S.J. *Dielectric and mechanical relaxation in materials.* Munique: Hanser Publisher, 1997.

92 JUSKA, G. et al. Extraction current transient: new method of studying of charge transport in microcrystalline silicon. *Physical Review Letters*, v. 84, n. 21, p. 4946-4949, 2000.

93 BANGE, S. et al. Charge mobility determination by current extraction under linear increasing voltages: case of nonequilibrium charges and field-dependent mobilities. *Physical Review B*, v. 81, p. 35209-35216, 2010.

94 TAJIMA, H.; YASUI, M. Determination of trap density function based on measurements of photoinduced charge carrier extraction using linearly increasing voltage at low temperatures. *Journal of the Physical Society of Japan*, v. 80, p. 63705-63709, 2011.

95 DONLEY, C.L. et al. Effect of packing structure on the optoelectronic and charge transport properties in poly(9,9-di-n-octylfluorene-alt-benzothiadiazole). *Journal of the American Chemical Society*, v.127, p. 12890-12899, 2005.

96 CAMPBELL, A. J. et al. Dispersive electron transport in an electroluminescent polyfluorene copolymer measured by the current integration time-of-fight method. *Applied Physics Letters*, v. 79, n.14, p.2133-2135, 2001.

97 TANASE, C. et al. Charge carrier density dependence of the hole mobility in poly(p-phenylenevinylene).In: BRUTTIN, W.(Ed.) *Physics of organic semiconductor.* Weinheim, Germany: Wiley-VCH, 2005.p.

98 GIRO, G.; DiMarco, P. G. Studies on temperature-dependent charge carrier mobility in poly-N-vinylcarbazole films. role of the excimer-forming sites as traps *Chemical. Physics Letters*, v. 162 p. 221-226, 1989.

99 BLOM, P. W. M.; VISSENBERG, M. C. Advances in polymer recombination. *Material Scince Engenniring,* v.27, p.53-52, 2000.

100 BLOM, P. W. M. et al. Recombination in polymer light-emmiting diode. *Polymer Advances Technologhy.* v.57, p.113-122, 2001.

101 Cobo, M.F. et al. Studies on thick and thin morphology of P3HT films. *To be submitted,* 2011.

102 ARIF, M. et al. Chain morphologies in semicrystalline polyfluorene: evidence from Raman scattering. *Physical Review Letters*, v. 96**,** p.25503, 2006.

103 CHEN, S.H. et al. Phase behavior of poly(9,9-di-n-hexyl-2,7-fluorene). *Journal of Physical Chemistry B*, v.110, p.4007, 2006.

104 CHEN, S.H. et al. Crystalline forms and emission behavior of poly(9,9-di-n-octyl-2,7-fluorene). *Macromolecules*, v.38, p.379, 2005.

CURRICULUM VITAE – Gregório Couto Faria – September/2011

Personal Data

Name: Gregório Couto Faria – (Faria, G. C.)
Place and Date of Birth: 5th January/1984, São Carlos – Brazil

Education

Degree in Physics, 2002- 2006, Instituto de Física de São Carlos, Universidade de São Paulo (IFSC/USP), Brazil – Scientific Initiation on Organic Electronics, from 2003 to 2006.

M.Sc. Physics, 2006-2008, Instituto de Física de São Carlos, Universidade de São Paulo (IFSC/USP), Brazil, supervised by Eduardo Ribeiro de Azevêdo Dissertation title: "A Multitechnique Study of Structure and Dynamics of Polyfluorene Cast Films and the Influence on their Photoluminescence".
Award: Best Master Thesis 0f 2008 given by "Nuclear Magnetic Resonance Users Association - AUREMN"

Doctor in Physics (Brazil) and Doctor rer. nat "summa cum laude" (Germany), 2008 - 2011, Instituto de Física de São Carlos, Universidade de São Paulo and Institute of Electronic Materials, Technischen Universität Brazil, supervised by Prof. Eduardo Ribeiro de Azevêdo and Prof. Heinz von Seggern. (**Double Diploma Agreement**)
Thesis Title: "Structure and Dynamics of F8BT as revealed by Solid-State NMR, Dynamic Mechanical Thermal Analysis and Wide Angle X- Ray Diffraction – Correlations with Optoelectronic Properties".
Award: Dilip-Das Gupta Awards given by the IEEE/USA (Institute of Electrical and Electronics Engineers) to the best young scientist. (2011)

Publications in peer-reviewed journals:

1. FARIA G. C.; FARIA; R. M.; DEAZEVEDO; E. R.; von SEGGERN, H.; Temperature Dependence of the Drift Mobility of Poly(9,9'-dioctylfluorene-co-benzothiadiazole) Based-Thin-Film Devices. The Journal of Physical Chemistry C. "Just Accepted Manuscript" – DOI: 10.1021/jp204893q

2. DE DEUS J. F.; FARIA G. C.; IAMAZAKI E. T.; AKCELRUD, L.C.; Polyfluorene based blends for white light emission. Organic Electronics. v. 12 , P: 1493-1504, 2011.

3. DEAZEVEDO, E. R. ; AYROSA, A. M. I. B. ; FARIA, G. C. ; CERVANTES, H. J.; HUSTER, D. ; BONAGAMBA, T. J. ; PITOMBO, R. N. M. ; RABBANI, S. R. . The effects of anticalcification treatments and hydration on the molecular dynamics of bovine

pericardium collagen as revealed by 13C solid-state NMR. Magnetic Resonance in Chemistry, p. 704-711, 2010.

4. AZEVEDO, E. R. ; FARIA, G. C. ; BATALHAO, T. B. ; CASTRO FILHO, J. ; SANTONI, E. ; SARTORI, J. L. ; NUNES, L. A. O. . Projection Spectrograph as a Tool for Light Polarization Classrooms Demonstrations. Química Nova (Impresso), v. 33, p. 1204-1210, 2010.

5. FARIA, G. C. ; PLIVELIC, T. S. ; COSSIELLO, R. F. ; SOUZA, A. A. ; ATVARS, T. D. Z.; TORRIANI, I. L. ; DEAZEVEDO, E. R. . A Multitechnique Study of Structure and Dynamics of Polyfluorene Cast Films and the Influence on Their Photoluminescence. Journal of Physical Chemistry. B, v. 113, p. 11403-11413, 2009.

6. FARIA, G C. ; COSSIELLO, R. F. ; ATVARS, T. D.Z. ; DEAZEVEDO, E. R. . Molecular relaxations in polyfluorene based cast films. Synthetic Metals, p. 2289-2292, 2009.

7. SOUZA, A ; COSSIELLO, R ; PLIVELIC, T ; MANTOVANI, G ; FARIA, G. C. ; ATVARS, T ; TORRIANI, I ; BONAGAMBA, T ; DEAZEVEDO, E . Temperature dependence of molecular dynamics and supramolecular aggregation in MEH-PPV films: A solid-state NMR, X-ray and fluorescence spectroscopy study. European Polymer Journal, v. 44, p. 4063-4073, 2008.

8. SANTOS, L ; FARIA, R ; DEANDRADE, A ; FARIA, G.C. ; AMORIN, C ; MERGULHAO, S . Transition from dispersive to non-dispersive transport of holes in poly(2-methoxy-5-(2-ethyl-hexyloxy)- 1,4-phenylene vinylene) light-emitting diodes investigated by time of flight measurements. Thin Solid Films, New York, v. 515, p. 8034-8039, 2007.